Athermal Phase Transformations of Germanate Pyroxenes under High-Pressure Condition

HATTORI Takanori

Thesis Submitted to
Graduate School of Science
Osaka University
for the Degree of
Doctor of Science (Physics)
2000

Abstract

In order to elucidate the transformation processes and mechanism of minerals at high-pressure and low-temperature where the atoms are not thermally activated, the pressure-induced change of crystal structure of $FeGeO_3$ clinopyroxene (*C2/c*) were investigated by X-ray diffraction techniques in conjunction with diamond anvil cell (DAC) and synchrotron radiation (SR).

$FeGeO_3$ clinopyroxene (*C2/c*) is reported to transform into the mixture of Fe_2GeO_4 spinel and GeO_2 rutile at high pressure and high temperature. In the present study, it transforms reversibly into a new high-pressure phase, $FeGeO_3$ (II), at 13 GPa and at room temperature. This process indicates that the initial phase tends to transform into the denser phase without atomic diffusion at low temperature. Analysis of the powder X-ray diffraction pattern showed that $FeGeO_3$(II) is based on the deformed the hexagonal closed packing (*HCP*) of oxygen and has the same cationic arrangements as that of clinopyroxene. TEM observation of the recovered sample shows that the phase transformation is accompanied by diffusionless mechanism. These results suggest that the clinopyroxene transforms into $FeGeO_3$(II) by martensite mechanism. The transformation process of $FeGeO_3$ implies that the high-pressure transformation of minerals at low temperature is generally accompanied by the shear mechanism rather than by the atomic diffusion process.

To reveal the onset of the shear-induced transformation at 13 GPa, the compression behavior of $FeGeO_3$ clinopyroxene have been investigated by single-crystal X-ray diffraction with diamond anvil cell up to 8.2 GPa. A series of the structure refinements shows the change of the compression mechanism at 4.5 GPa. Below 4.5 GPa, the GeO_4 tetrahedra are essentially incompressible with the significant decrease in Ge-O-Ge bond angle, whereas at higher pressures the GeO_4 tetrahedra are significantly compressed with keeping the Ge-O-Ge angle. The result of molecular orbital (MO) calculation shows that the above geometrical change of tetrahedral linkage contributes to

the increase in local energy of tetrahedral linkage, and the transformation into $FeGeO_3$ (II) is induced by the local instability of the tetrahedral linkage. It is inferred from the results on $FeGeO_3$ that the transformation of mineral compounds at low temperature, where the atoms are not thermally activated, is induced by the instability of the local unit.

Preface

Present thesis concerns with high-pressure transformations of minerals under temperature condition where atoms are not thermally activated. High-pressure transformations and the precursory phenomena of $FeGeO_3$ clinopyroxene (*C2/c*) were investigated from viewpoints of their crystal structures by in-situ powder X-ray diffraction and high-pressure single crystal X-ray diffraction methods for the purpose of elucidating the following points: (i) the transformation mechanism: (ii) the onset of high-pressure transformation: (iii) the effects of the crystal structure on transformation processes.

In Chapter 1, the background and the purposes of this study are introduced. Chapter 2 reviews previous studies on compression processes and transformation processes of pyroxenes. The experimental procedures of in-situ powder X-ray diffraction and high-pressure single crystal X-ray diffraction are described in Chapter 3. Experimental results are given in Chapter 4 in the order of the powder X-ray diffraction at high-pressure and room temperature, the transmission electron microscopy (TEM) and analytical-TEM (ATEM) examination of the recovered sample, and the single crystal X-ray diffraction and the molecular orbital (MO) calculation. The discussion on the transformation mechanism, the onset of the transformation and the effect of the crystal structures on the transformation processes are given in Chapter 5. Conclusions of the present thesis are given in Chapter 6.

Acknowledgments

I am greatly indebted to Prof. T. Yamanaka for helpful advice and discussion in the course of the investigations and careful reading this manuscript. I also thank to Prof. S. Kawarazaki, Prof. H. Takei, Assistant Prof. Y. Kudo and Assistant Prof. A. Onodera for the careful reading this manuscript.

I wish to express the special thanks to Dr. T. Nagai for many advice and technical supports on this study, to Prof. Schulz and Dr. S. Werner of Munchen University for the kindly help of the single crystal diffraction works and the instruction on structure analysis using DAC, to Prof. M. Kitamura, Dr. N. Shimobayashi and the students in Kitamura laboratory of Kyoto University for helpful assistance of TEM observation and useful discussion.

I thank Assistant Prof. A. Yoshiasa and Assistant Prof. O. Ohtaka for helpful discuss and constructive comments on my studies. I am very grateful to Y. Noda and T. Shobu of Tohoku University and N. Ikeda of SPring8 for the instructions on X-ray structure analysis and technical supports of the intensity data collection at SPring8. I thank Miss J. Mimaki for instruction on the MO calculation, many colleagues for lending me their personal computers, Dr. Nakatsuka for the helpful advice of studies, Dr. Chihara for the discussion on the error estimation, many colleagues and secretaries in Yamanaka, Takei, Masuda and Sunamura laboratory for enjoying our college life together. I thank many friends in Ohshima, Nasu laboratory and the colleagues at swimming pool for their encouragements. Finally, I thank my parents and the sister for their encouragements and economic assistance.

Contents

Chapter 1. Introduction

1.1 High-pressure phase transformation

All materials change crystal structures with temperature, pressure, electric and magnetic fields and the different chemical circumstances. In these processes, the structures may distort and change their local and bulk symmetries; they may rearrange the atomic positions; the occupancies of the cation sites may become ordered or less ordered. These processes are called phase transformation. Especially, the pressure-induced changes are called high-pressure transformations.

High-pressure phase transformations are very important in the Earth Science. Many minerals tend to take the denser structures under high-pressure and high-temperature conditions in deep Earth's interior. Phase relations of the mantle constituent minerals under high-pressure and high-temperature conditions have been investigated to reveal the Earth's interior.

The previously reported high-pressure transformation sequences of AO_2 and ABO_3 minerals are shown in Fig. 1.1. These phase transformations are divided into some categories on the basis of the Buerger's structural classification (1951, 1961) (Table 1.1, 1.2). Each category is subdivided into reconstructive and displacive transformations. The former is accompanied by breaking the chemical bonds and the latter is accompanied by the small shifts of the atomic positions. Most of transformations of AO_2 and ABO_3 minerals are reconstructive and involve the coordination increase.

1.2 Metastable state

Generally reconstructive phase transformations of silicate minerals are accompanied by the large activation energy because the large energy is needed for disconnecting the strong Si-O bonds. Therefore, the transformations are very sluggish and the system cannot often move into an equilibrium state under low-temperature condition where the atoms are not thermally activated.

If the phase is present in a local minimum of free energy instead of in a unique minimum and is separated still from lower minimum by energy barriers, the system is said to be in a "metastable state". Under such condition, the parent phase is often metastably compressed and, in some case, transforms into another metastable state through a lower activation energy path (Ostwald step rule). These transformations are often observed in the compression of mineral compounds at room temperature. For example, the SiO_2 quartz transforms into the amorphous state at about 15~20 GPa, not into its high-pressure polymorphs of coesite and stishovite (Hemley et al. 1988). Similar transformations have been reported in many compounds (c.f. review: Richet and Gillet 1997, Yamanaka et al. 1997). In spite of many experimental and theoretical approach, no studies have successfully accounted for the mechanism of the amorphization. These transformations cannot be understood by thermodynamics. The understanding of the process and the mechanism of these transformations is indispensable for understanding the structural change of minerals under the condition where the atomic diffusion is restricted.

1.3 Transformation processes under room temperature

Previously reported transformation process of AO_2 and ABO_3 minerals under high-pressure and room temperature conditions are shown in Fig 1.2. Transformation processes of some compounds under room-temperature condition are remarkably different from those at high-temperature (Fig 1.1). This results suggest that the transformation mechanism is different between these transformation. The first aim of this study is to reveal the transformation mechanism at low temperature where atoms are not thermally activated.

1.4 Effects of crystal structure on the transformation process

Nagai (1995) have investigated the relation between the oxygen packing and high-pressure transformations of several germanates at room temperature by powder X-ray diffraction. $MgGeO_3$

and $CaGeO_3$ germanates based on cubic closest packing (*CCP*) of oxygen reversibly transforms into the crystalline states, whereas Mg_2GeO_4 olivine with the hexagonal closest packing (*HCP*) of oxygen transforms irreversibly into the amorphous state. This study shows the effects of crystal structure on the transformation process, however the detailed relation is still unclear because of the lack of the detailed atomic movements on transformation. The second aim is to reveal the relation between the crystal structure and transformation process through the investigation of atomic movements during the transformation.

1.5 Onset of pressure-induced transformation

The onset of the transformations of the metastably compressed phases cannot be predicted from the viewpoint of thermodynamics. In such case, the structural stability of a parent phase may explain the onset of phase transformation. One of the most intensively studied examples is the pressure-induced transformation of α-quartz.

α-quartz consists of vertex-shared tetrahedra. Hemley et al. (1988) have discovered a pressure-induced amorphization of α-quartz at room-temperature. Many theoretical and experimental studies have been performed to reveal the mechanism (c.f. Kim-Zajous et al. (1999) and the references therein). Hazen et al. (1989) revealed that the Si-O-Si bond angle and inter-tetrahedral distance of O-O dramatically decreases with increasing pressure and concluded that the excessive decrease of the inter-tetrahedral angle of Si-O-Si below 120° induces the amorphization. The computer simulation results show the similar results (Chelikowsky et al. 1990). The molecular orbital (MO) calculation also supports the instability of the tetrahedral linkage due to the excessive kinking of tetrahedral chain (Geisinger et al. 1985). These results suggest that the pressure-induced amorphization of α-quartz is induced by the local instabilities of the tetrahedral linkage. However, it is still unclear whether this concept is generally applicable

to the transformations of other compounds. In the present study, the onset of transformation of chain germanates with vertex-shared tetrahedra are investigated from the structural aspects.

1.6 Present approach

In this study, the author focused on a chain germanate of $FeGeO_3$ clinopyroxene (*C2/c*) in terms of the following points:

(i) The detailed atomic movements on transformation is necessary for the above purpose. The chain germanates have been known to transform into crystalline state, not into amorphous state (Nagai 1995). Therefore, the chain germanate is considered to be preferable for an investigation of atomic movements using the X-ray diffraction method. (ii) Only the chain germanates transforms into crystalline state, not into amorphous state, among various germanates under high-pressure and room-temperature conditions. An investigation of the transformation mechanism of chain germanates will help understand the effects of the crystal structure on the transformation process. (iii) The results of α-quartz suggest the close relationship between the highly-kink of tetrahedral chain and the structural stability. The tetrahedral chains of germanate clinopyroxenes are most highly-kinked among all the pyroxenes. Therefore, the germanate clinopyroxene is appropriate for an investigation of the onset of the phase transformation.

In order to reveal the transformation process, $FeGeO_3$ clinopyroxene (*C2/c*) has been investigated up to 20 GPa by in-situ powder X-ray diffraction using an imaging plate (IP) in conjunction with synchrotron radiation (Chapter 4.1). The results showed that $FeGeO_3$ clinopyroxene transformed reversibly into a denser high-pressure phase of $FeGeO_3$ (II). The structure of the high-pressure phase was successfully refined on basis of the powder X-ray diffraction pattern at 20.1 GPa. To know the transformation mechanism, the sample recovered from about 20 GPa were also examined by transmission electron microscope (TEM) and analytical-

TEM (ATEM) (Chapter 4.2).

In order to reveal the onset of the transformation, the detailed crystal structure before the transformation was investigated up to 8.2 GPa by single crystal X-ray diffraction (Chapter 4.3). The Ge-O bond length and Ge-O-Ge angle of $FeGeO_3$ clinopyroxene significantly changed with increasing pressure. To comprehend this compressional behavior, the strain energy of the tetrahedral chain was estimated by the molecular orbital (MO) calculation (Chapter 4.4).

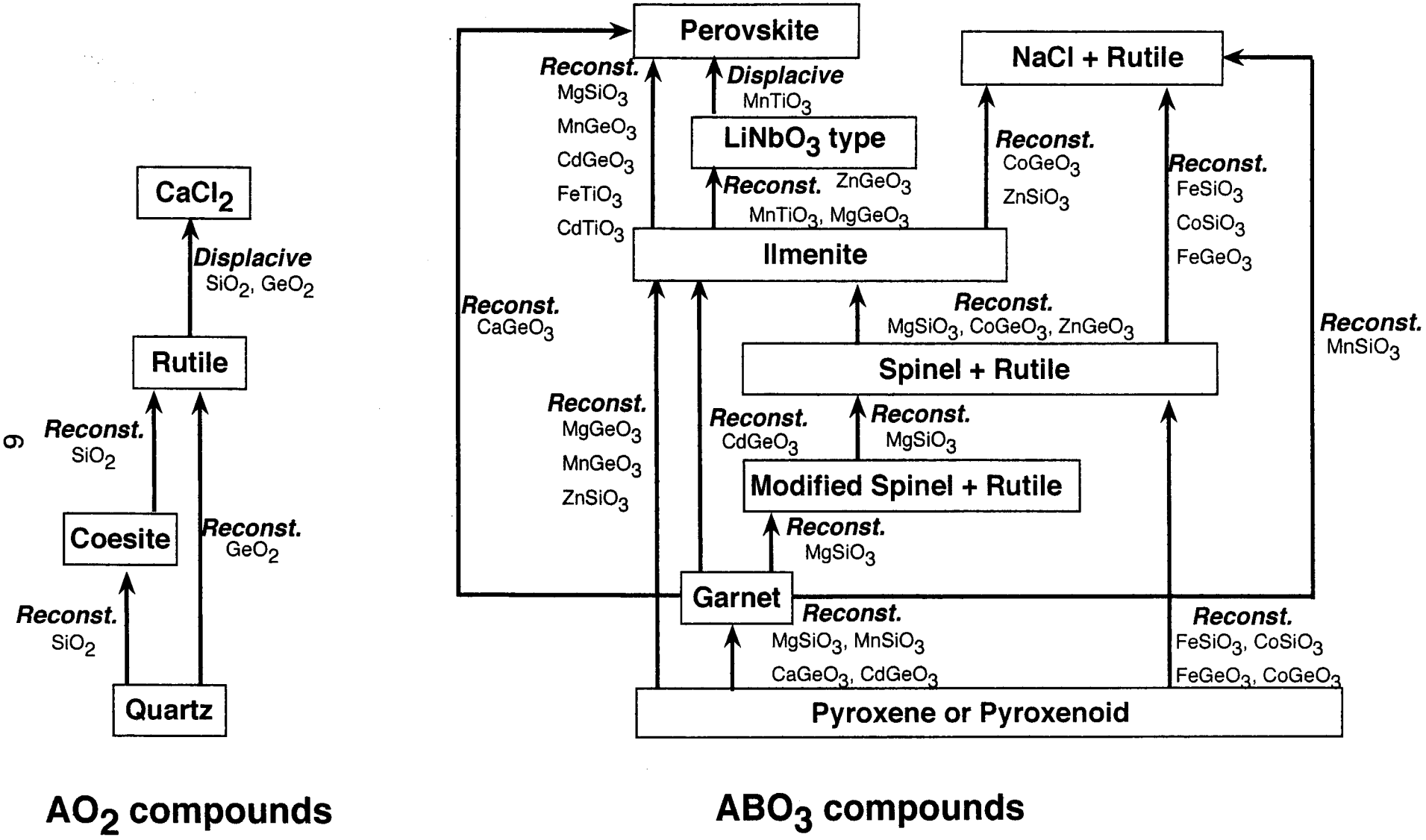

Fig 1.1 Transformation sequences of AO_2 and ABO_3 minerals under high-pressure and high-temperature conditions

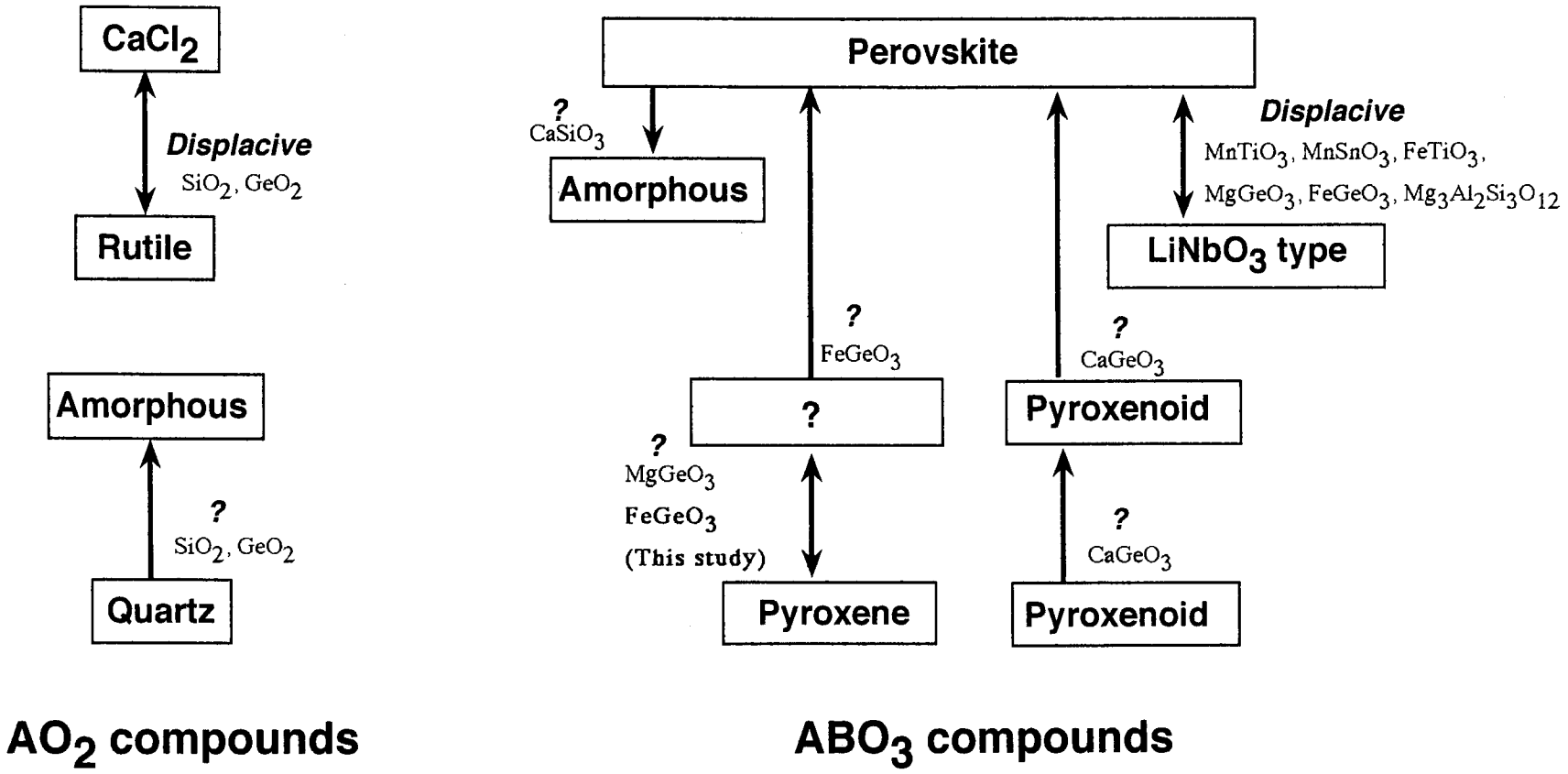

Fig. 1.2 Transformation sequences of AO_2 and ABO_3 minerals under high-pressure and room-temperature conditions

Table 1.1 Buerger's structural classification

(i) Transformations involving first coordination
    (a) reconstructive (sluggish)
    (b) dilatational (rapid)
(ii) Transformations involving second coordination
    (a) reconstructive (sluggish)
    (b) displasive (rapid)
(iii) Transformations involving disorder
    (a) substitutional (sluggish)
    (b) rotational (rapid)
(iv) Transformation of bond type (sluggish)

Table 1.2 Structural classification of the high-pressure transformations of AO_2 and ABO_3 compounds.

(i)	(a)	Coesite→Rutile, Quartz→Rutile Pyroxene→Ilmenite, Pyroxene→Garnet, Pyroxene→Spinel + Rutile, Garnet→Perovskite, Garnet→Ilmenite, Garnet→Spinel + Rutile, Garnet →NaCl + Rutile Spinel + Rutile→Ilmenite Ilmenite→NaCl+Rutile
	(b)	---
(ii)	(a)	Quartz→Coesite Ilmenite→Perovskite
	(b)	$LiNbO_3$-type→Perovskite
(iii)	(a)	Ilmenite→$LiNbO_3$-type
	(b)	Rutile→$CaCl_2$
(iv)		---

Chapter 2. Previous studies of pyroxene

2.1 Crystal structures of pyroxenes

A typical crystal structure of pyroxenes is shown in Fig. 2.1a (Zhang et al. 1997). Pyroxene consist of vertex-shared tetrahedral chains and edge-shared octahedral bands. The tetrahedral chains bridge the octahedral bands laterally along *b*-axis. The chain has the flexibility of kink and tilt. This variations in the geometry generate the various crystal structures with different crystal systems and symmetries (Cameron and Papike 1980). A typical change of crystal structure of $MgSiO_3$ pyroxene is shown in Fig. 2.2 (Angel et al. 1992; Gasparik 1990; Kanzaki 1991; Pacalo and Gasparik 1990; Shimobayashi and Kitamura 1991).

The tetrahedral chain geometry is described in terms of kink of tetrahedral chain and tilt of the tetrahedral basal plane. The kink is represented by O3-O3-O3 angle defined by the bridging oxygen (O3) of tetrahedra. The tilt is represented by an inclination angle of the normal of tetrahedral basal plane (Fig. 2.1). From the geometrical relationship between the polyhedral size and tetrahedral chain, the kink angle (*<O3-O3-O3*) has the following relation to edge distance ratio of octahedra to tetrahedra (d_{oct}/d_{tet},)

$$< O3 - O3 - O3 = 2\sin^{-1}\left(\frac{\sqrt{3}}{2}\left(\frac{d_{oct}}{d_{tet}}\right)^{-1}\right)$$

where d_{oct} and d_{tet} indicate the mean edge distances of octahedra and tetrahedra, respectively. Two extreme ends of chain geometry help understand many chain geometries in pyroxenes. One is the most-extended chain with O3-O3-O3 angle of 180 ° at the edge ratio of $2/\sqrt{3}$. The other end is the most-kinked chain with O3-O3-O3 angle of 120 ° at the edge ratio of 1/1. In the latter case, the oxygen arrangement becomes ideal *CCP* and, therefore, the structure is called "ideal pyroxene" (Cameron and Papike 1980). Tetrahedral chains in many pyroxenes have intermediate

geometry between these ends. This geometry changes with chemical compositions of the polyhedra or the change of temperature and pressure condition.

$FeGeO_3$ clinopyroxene (*C2/c*) has the most highly-kinked tetrahedral chain among various pyroxenes (O3-O3-O3 = 131.1°). The structure is very close to the ideal clinopyroxene (Fig. 2.1b) (Yamanaka, personal communication). The oxygen arrangement can be approximated by cubic closed packing (*CCP*) (Peacor 1968). Fe^{2+} and Ge^{4+} cations locate at interstices between oxygen stacking layers, alternately along the stacking direction.

2.2 Pressure-induced change of crystal structure

Pressure-induced structural changes of pyroxenes have been investigated to speculate the crystal structure under the upper mantle condition (Levien and Prewitt 1981; Zhang et al. 1997; Hugh-Jones and Angel 1994; Hugh-Jones et al. 1997). The high-pressure structure analyses showed that octahedra are more compressible than tetrahedra. Consequently, the edge distance ratio d_{oct}/d_{tet} increases and the tetrahedral chains become more kinked with pressure. The examples are shown in Fig. 2.3 (Levien and Prewitt 1981; Zhang et al. 1997; Hugh-Jones et al. 1997).

2.3 Transformation processes under high-pressure condition

2.3.1 High-pressure transformations at high temperature

P-T phase diagram is shown in Fig. 2.4. $FeGeO_3$ clinopyroxene (*C2/c*) is stable at ambient condition. It decomposes into the mixture of Fe_2GeO_4 (spinel) and GeO_2 (rutile) phases at about 1 GPa and 1000 °C (Ringwood and Seabrook, 1963). One of the decomposed phases, Fe_2GeO_4 (spinel) transforms into $Fe_{1-x}O$ (wustite) and GeO_2 (rutile) at about 25 GPa and 1400-1800 °C (Liu et al. 1977). In summary, $FeGeO_3$ clinopyroxene (*C2/c*) transforms into high-pressure phases in the following sequences:

$$FeGeO_3 \rightarrow \frac{1}{2} Fe_2GeO_4 + \frac{1}{2} GeO_2 \rightarrow Fe_{1-x}O + GeO_2$$

2.3.2 High-pressure transformations at room-temperature

High-pressure transformation of $FeGeO_3$ clinopyroxene (*C2/c*) at room temperature has not been investigated. High-pressure study of $MgGeO_3$ clinopyroxene (*C2/c*) at room temperature help predict the transformation of $FeGeO_3$ clinopyroxene.

The transformation of $MgGeO_3$ clinopyroxene (*C2/c*) has been investigated at room temperature up to 35 GPa by in-situ powder X-ray diffraction method (Nagai 1995). $MgGeO_3$ clinopyroxene transforms reversibly into a high-pressure phase at about 10 GPa. The crystal structure of high-pressure phase is not those of the previously reported high-pressure phases (ilmenite, $LiNbO_3$-type, perovskite) (Fig. 2.5a). It is still uncleared because of the low quality of the diffraction patterns taken by a conventional X-ray source and position sensitive detector (PSD). EXAFS study on $MgGeO_3$ clinopyroxene revealed that the coordination number of Ge^{4+} cation increases from fourfold to sixfold between 7.5 GPa and 31 GPa (Fig. 2.5b) (Andrault et al. 1992). These experimental results suggests that $MgGeO_3$ clinopyroxene transforms reversibly into a high-pressure phase with the coordination increase of Ge^{4+} cation at about 10 GPa.

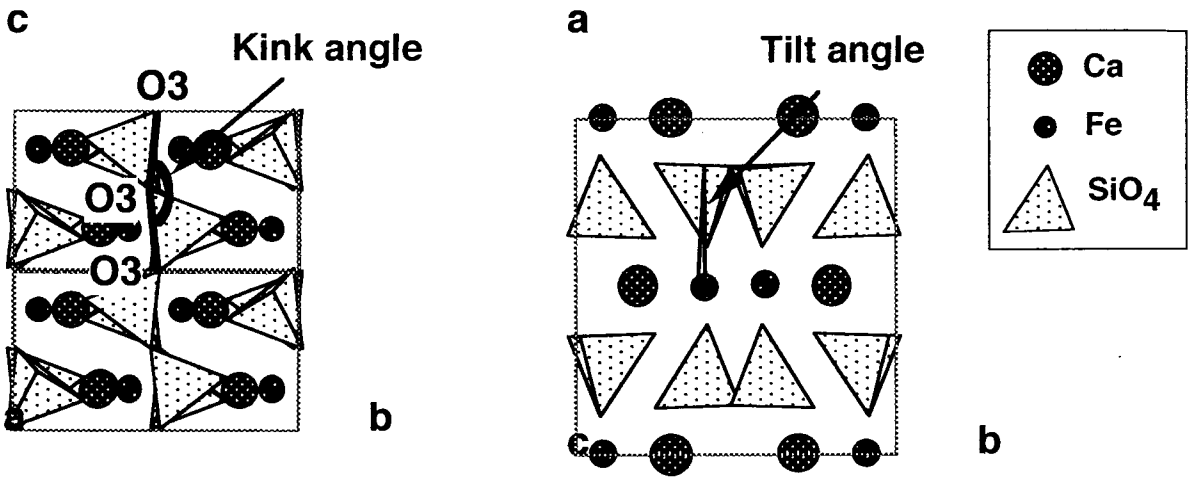

Fig. 2.1a Crystal structure of $CaMgSiO_3$ (Levien and Prewitt 1981)

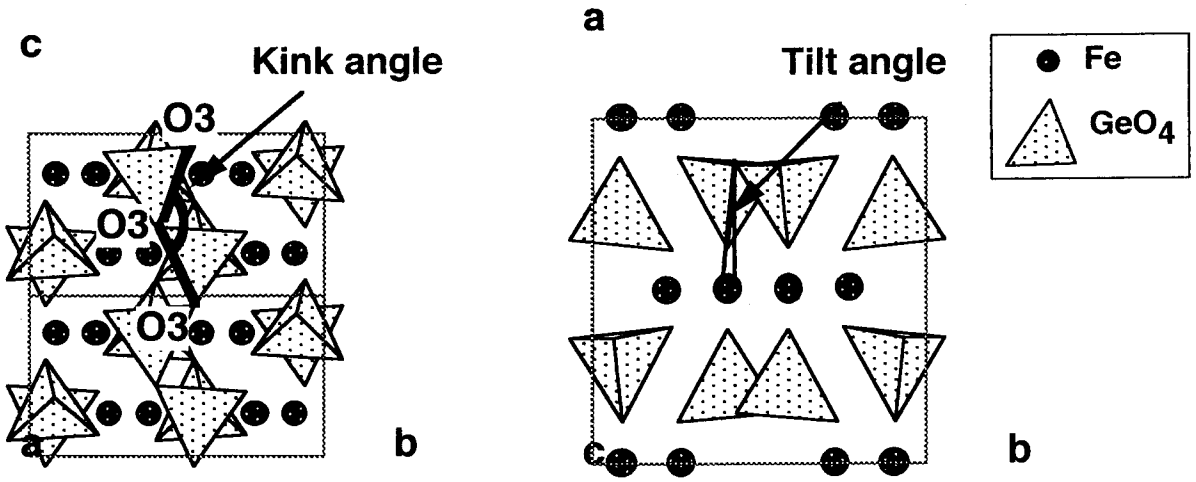

Fig. 2.1b Crystal structure of $FeGeO_3$ (Yamanaka et al. 1985)

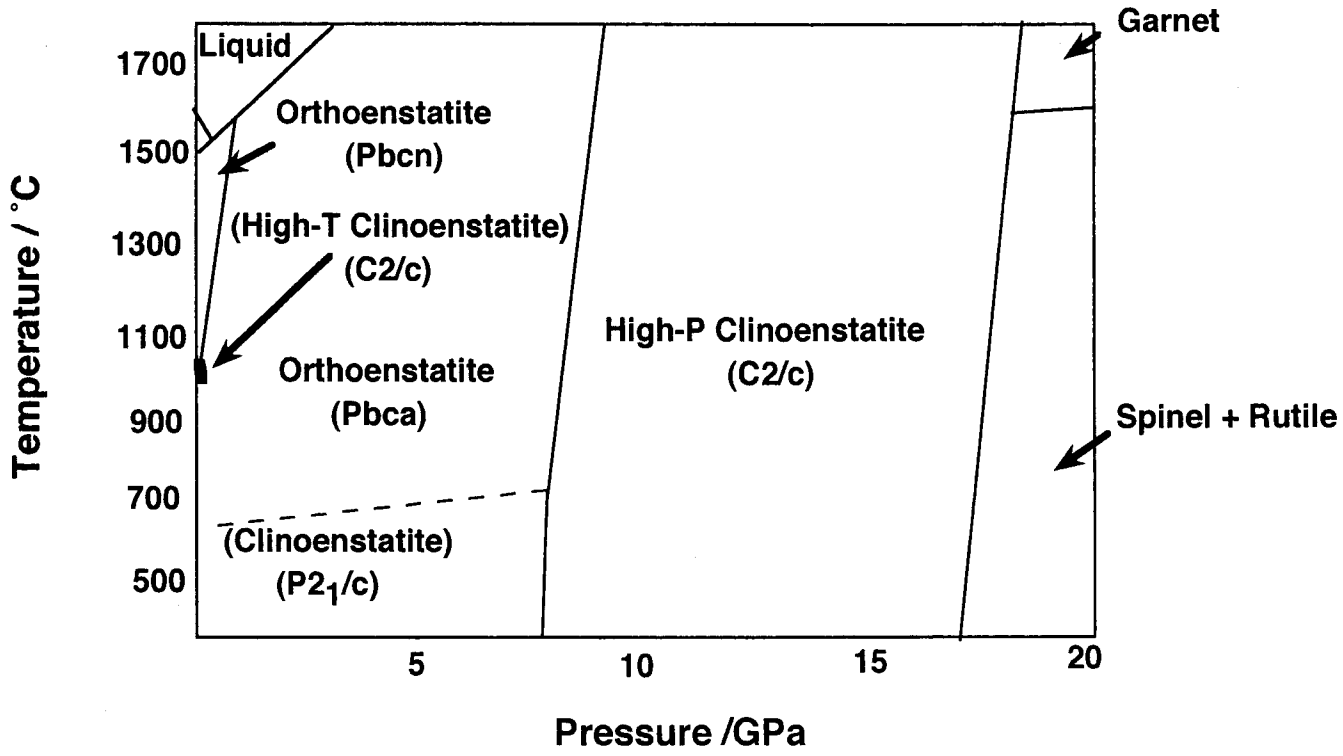

Fig. 2.2 *P-T* phase diagram of $MgSiO_3$ pyroxene (Angel et al. 1992, Gasparik 1990, Kanzaki 1991, Pacalo and Gasparik 1990, Shimobayashi and Kitamura 1991).

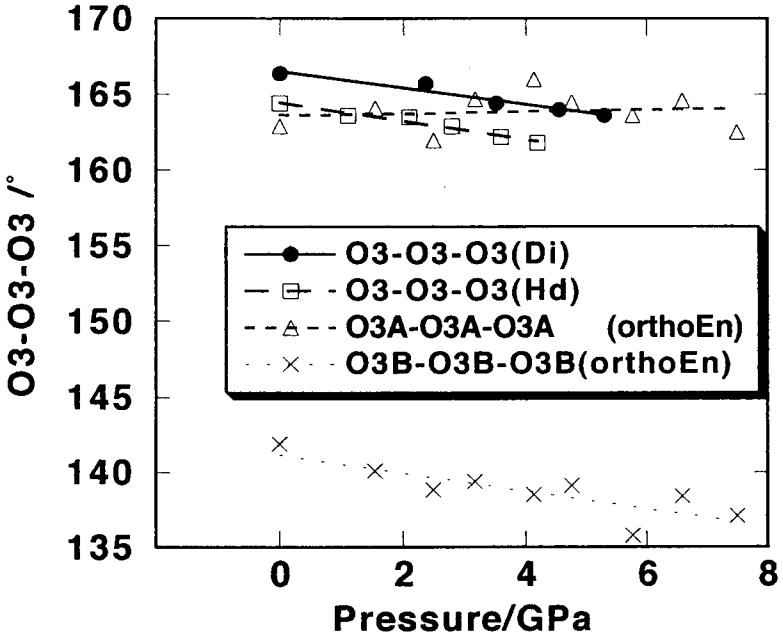

Fig. 2.3 Variation of O3-O3-O3 angles in tetrahedral chains of $CaMgSiO_3$, $CaFeSiO_3$ clinopyroxenes and $MgSiO_3$ orthopyroxene with pressure (Levien and Prewitt 1981, Zhang et al. 1997, Hugh-Jones et al. 1997)

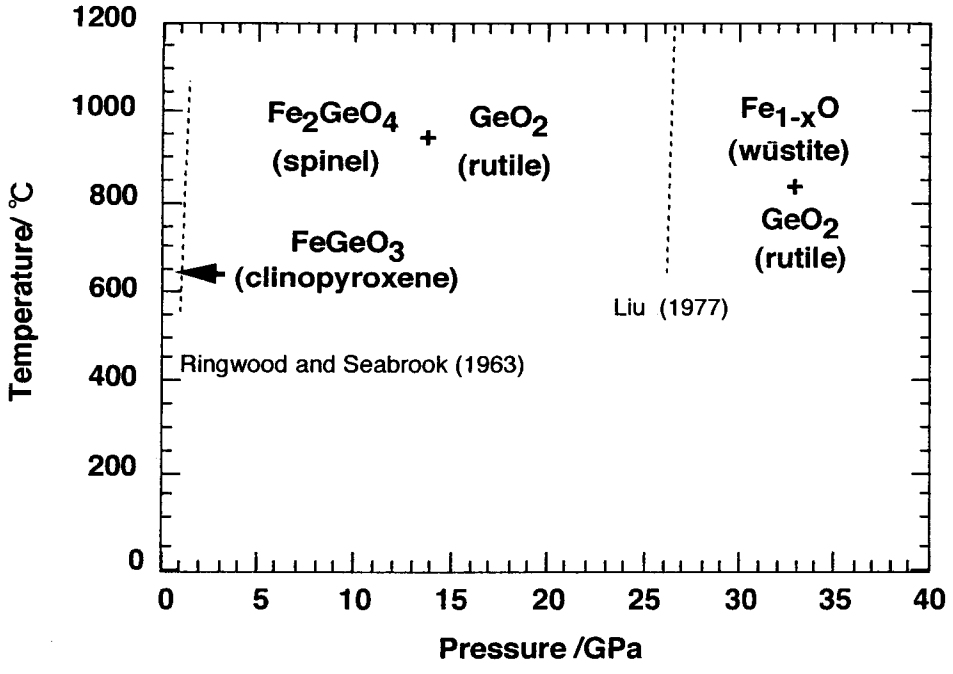

Fig. 2.4 *P-T* phase diagram of $FeGeO_3$ (Ringwood and Seabrook 1963, Liu 1977)

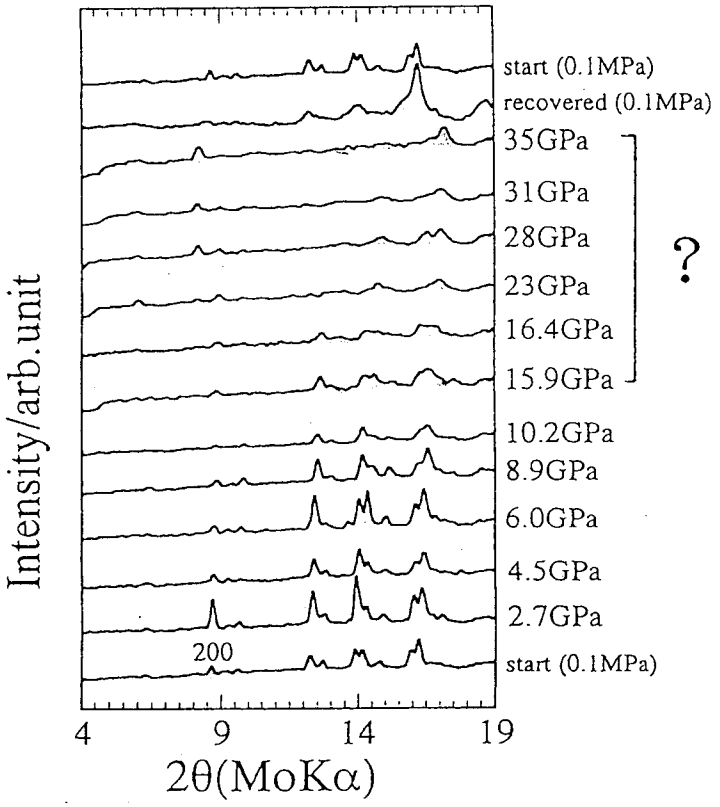

Fig. 2.5a X-ray diffraction patterns of $MgGeO_3$ clinopyroxene at pressures up to 35 GPa (Nagai 1995)

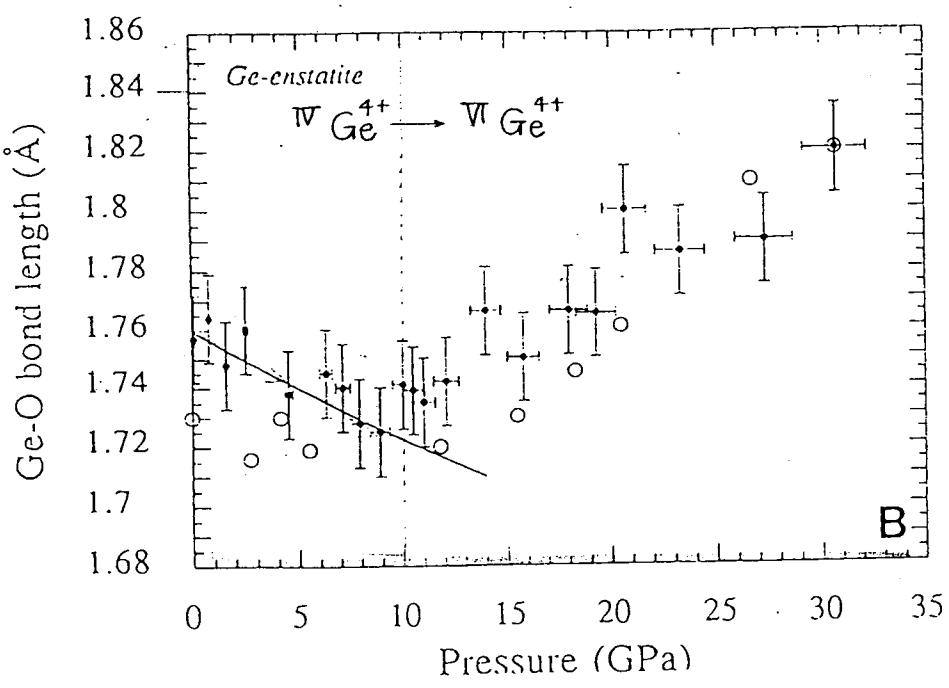

Fig. 2.5b Variation of the Ge-O bond length in $MgGeO_3$ as a function of pressure. *Full circles*, at increasing pressure from 0 to 30.7 GPa; *open circles*, at decreasing pressure from 30.7 to zero pressure. The *full line* expresses the compressibility of the GeO_4 tetrahedron before the change of coordination of germanium atoms (Andrault et al. 1992).

Chapter 3. Experimental

3.1 Sample preparation of $FeGeO_3$

3.1.1 Synthesis of $FeGeO_3$ clinopyroxene (*C2/c*)

The condition and procedures for the synthesis of $FeGeO_3$ clinopyroxene (*C2/c*) were based on Takayama et al. (1981). The phase diagram of FeO-Fe_2O_3-GeO_2 system is shown in Fig. 3.1. The sample was synthesized on the basis of the following reaction equation:

$$Fe + Fe_2O_3 + 3GeO_2 = 3FeGeO_3$$

Iron metal, Fe_2O_3 (E. Merk: 99%) and GeO_2 (Nacalai tesque Co. Ltd: 99.999%) were used as the starting materials. The mixture of these powder samples was compressed up to the pressure of 100 kg/cm^2 by a hand pump and formed into a pellet in order to proceed the solid-solid reaction more effectively. The pellet was sealed in the evacuated silica tube (10^{-3} Torr) to avoid the oxidation of Fe^{2+} ion and was kept at 1000(5) °C in a SiC heater-rounded box furnace. After the duration of 14 days, the sample was quenched in the furnace. Opaque black crystals with the linear size of 10 ~ 300 μm were obtained (Fig. 3.2).

3.1.2 Characterization of the synthesized sample

Electron Probe Micro Analysis

The chemical composition of the synthesized sample was examined by JEOL JXA-733 Electron Probe Micro Analyzer. A sample surface was polished by SiC powders of #1000, #320, #180 and diamond pastes with the grain size of 3, 1, 1/4 μm. Carbon was deposited on the surface to avoid the electron charge up during EPMA analyses.

The examination was performed through the operation of the acceleration voltage of 15 kV and the filament current of 1.2 x 10^{-8} A. The quantitative analysis was undertaken by angler dispersive method with three analyzer crystals on a high speed qualitative analysis program

(QLAN). The quantitative analysis was carried out by intensity measurement of the characteristic X-ray from the electron radiated area with the correction by atomic-number, absorption and fluorescence (ZAF) method.

The electron back scattering image does not show any remarkable contrast due to spatial inhomogeneity of chemical elements. The chemical compositions in any measured points are $FeGeO_3$ within experimental uncertainty and no metal elements except Fe and Ge were detected.

Powder X-ray diffraction

The powder X-ray diffraction pattern of the synthesized sample was taken by the Rigaku RAD-B diffractometer using CuK_α radiation. A sealed tube X-ray generator was operated at 35 kV and 15 mA. The powder pattern was taken by θ–2θ step scanning mode with fixed time of 8 seconds.

The X-ray diffraction pattern is shown in Fig. 3.3. All the diffraction peaks could be indexed as clinopyroxene. No diffraction peaks except those of clinopyroxene were observed in the pattern. The comparison between the observed *d*-values and those of JCPDS card (JCPDS #35-1265) are shown in Table 3.1. The *d*-values of the synthesized sample were coincident with those of JCPDS within the experimental uncertainty. The refined lattice parameters of $FeGeO_3$ were $a = 9.801(27)$ Å, $b = 9.145(19)$ Å, $c = 5.097(20)$ Å and $\beta = 101.95(39)°$. All the above data indicate that the $FeGeO_3$ clinopyroxene (*C2/c*) was prepared successfully.

3.2 Principle of high-pressure generation and structure analysis

3.2.1 High-pressure generation

The high-pressure generation technique is essential for the investigations of crystal structure at high pressures. The pressure is generated by the concentration of the force. The principle is explained by the following equation:

$$F = PA = p' a' = p'' a''$$

where F is the equilibrium force: P is the pressure applied on the anvil surface with area of A. The pressure is amplified when we use the anvil with two different areas of a' and a''' . The amplification factor is written by the following relation;

$$p'' = \frac{a'}{a''} p'$$

The amplified pressure of p' is a' / a'' times as much as that of p''. The above amplification factor becomes about 40 when we use the anvils with surface areas of 0.4 mmϕ and 2.5 mmϕ.

Two types of the high-pressure cell have been generally used in high-pressure experiments. One is diamond anvil cell (DAC) and the other is multi anvil cell made of the tungsten carbide (WC) or sintered diamond. Especially, the diamond anvil cell (DAC) has the great advantage in the crystal structure analysis, because the diffraction intensity from sample can be measured precisely due to the small X-ray absorption factor of diamonds. Thus, the DAC was used in the present studies.

3.2.2 Pressure measurements

Pressure was measured by the ruby fluorescence method. It is empirically known that the wavelength of ruby R_1 fluorescence line shifts with increasing pressure on the following relation (Mao et al. 1978);

$$P(GPa) = 380.8\left[\left(\frac{\lambda}{\lambda_0}\right)^5 - 1\right]$$

where P is the pressure: λ and λ_0 are the wavelength at high-pressure and ambient pressure, respectively. The generated pressure is determined from the wavelength of the ruby chips in the DAC. The accuracy of the determination on the above scale is within 6 % error in the pressure range between 6 and 100 GPa (Mao et al 1978).

In the powder X-ray diffraction study, the pressure measurements were carried out on the Ruby fluorescence system installed at BL-18C in Photon factory (PF). The pressures were measured before and after each X-ray exposure. These pressure difference was within 5% and the averaged pressure was adopted. In the single crystal study, the pressure measurements were carried out on the Ruby fluorescence system at Munchen University. The pressures were measured before and after the diffraction intensity measurements. The pressure measured after the measurement was adopted in single crystal study.

3.2.3 Structure analysis by X-ray diffraction

The electrons in crystals scatter the incident X-ray coherently. The scattered X-rays interfere mutually and form a X-ray diffraction pattern characteristic of the atomic arrangements of crystal. Therefore, the atomic arrangements can be revealed from this pattern.

The diffraction intensity from crystals is generally expressed by

$$I = I_0 A |F(hkl)|^2 \left(\frac{e^2}{mc^2}\right)^2 \left(\frac{1}{r^2}\right) LP$$

$$F(hkl) = \sum_j f_j T_j \exp\left[i\left(hx_j + ky_j + lz_j\right)\right]$$

where I_0 is the intensity of the incident beam; A is absorption factor; $F(hkl)$ is the structure factor for a hkl reciprocal point:$(e^2/mc^2)^2$ is the classical Thomson scattering amplitude for a free electron: L and P are the Lorentz and polarization factor, respectively: f_j is the atomic scattering factor for i element: T_j is the temperature factor. $|F(hkl)|$ is measured from the diffraction intensity of hkl reflection.

The electron density at position, (x, y, z) in the unit cell can be expressed by:

$$\rho(x,y,z) = \frac{1}{V} \sum_h \sum_k \sum_l F(hkl) \exp\left[-i(hx + ky + lz)\right]$$

Thus, the atomic positions in the unit cell can be revealed by the Fourier Transformation of *F(hkl)'* by measuring the diffraction intensity of many *hkl* reflections.

3.3 In-situ powder X-ray diffraction at high pressure

3.3.1 Importance of the in-situ observation

We can reveal the crystal structure of the high-pressure phase through the structure analysis of the recovered sample when the phase is quenchable at ambient pressure. On the other hand, we can not reveal the structure through the analysis of the recovered phase when the high-pressure phase are unquenchable. In such case, in-situ observations of high-pressure phase is of great advantage for the structure determination.

In-situ powder X-ray diffraction technique under extreme conditions has been developed. Recent developments in the pressure generation technique using DAC, the intensive synchrotron radiation source and the sensitive two-dimensional detector of imaging plate (IP) have enabled us to obtain the high quality X-ray diffraction pattern of the sample under high-pressure condition.

3.3.2 Advantage of the synchrotron radiation source

The synchrotron radiation facilities, such as the Photon Factory (PF) in Institute of High Energy Physics (KEK) and the Super Photon ring -8 GeV (Spring 8), have been constructed. The synchrotron radiation source has the great advantage in the crystal structure analysis in terms of the following points:

(i) High brilliance of the X-ray beam

The synchrotron radiation source is generated by bremsstrahlung of the accelerated photon nearly up to light speed. The brilliance of the synchrotron radiation which are generated by the bending magnet is about 10^{12} [photons /s /mm^2 /mrad^2 0.1 % band width], which is about 10^4 times as much as that of conventional rotating anode X-ray generator (10^8 [photons /s /mm^2

/mrad^2 /0.1 % band width]). The large diffraction intensity of synchrotron radiation source enables the high S/N ratio, the detection of the weak diffraction peaks, the more precise determination of diffraction intensity and the short measuring period. These characters are preferable for knowing the subtle change of the diffraction patterns, the precise structure determination of the high-pressure phase and the time-resolved X-ray diffraction study.

(ii) Short wavelength and small energy-dispersion

The synchrotron radiation source is basically white X-ray source. The desired X-ray wavelength can be obtained by monochromation of the white X-ray source using crystal monochromator. Especially, the shorter wavelength is of great advantage to the angler-dispersive X-ray diffraction of the sample in DAC. When the shorter wavelength is selected, the diffraction intensities of the reflection with the higher Q-values can be obtained under the restriction of the aperture angle of DAC. It enables the precise structure determination of the high-pressure phase through Rietveld analysis.

The energy-dispersion of monochromatized X-ray is $\Delta E/E = 5 \times 10^{-4}$. The small dispersion decreases the full width at the half maximum (FWHM) of diffraction peaks. The sharp diffraction profile increases the resolution of the peak position.

(iii) Highly collimated and parallel beam

The divergence of synchrotron radiation source is about 0.38 mrad and 0.037 mrad respectively along the vertical and horizontal directions in PF. The small divergence makes the diffraction peak more sharp and will increase the resolution of the peak position.

The above mentioned advantages contribute to the identification of the high-pressure phase and the structure determination of high-pressure phase.

3.3.3 High-pressure cell for powder X-ray diffraction

The lever-spring type DAC (Toshiba Tungaloy Co., Ltd.) was used in powder X-ray diffraction study at high pressures (Fig. 3.4). This cell have been originally designed by Mao and Bell (1978) and have been modified by Yagi and Akimoto (1982). The parallelism of the culet surfaces of diamond is important for the high pressure generation. The long stroke of the piston and cylinder in this cell is of great advantage for this purpose. The sample pressure is raised by rotating the screw at the end of the lever part. The force applied by the screw is amplified by the lever arm and is transferred to the diamond culet surface. It was reported that the static pressure above ~350 GPa is generated by this cell. The anvil supporting plates have the narrow slits for the path of the incident and diffraction X-ray beams. The diffraction intensity from the sample is measured through diamond anvils and these slits. The aperture angle of the slit is about 80° along 2θ direction, which enables the intensity data up to 2θ angle of 40 °.

The diamonds with the culet sizes of 350 μmϕ were used. The single crystal of $FeGeO_3$ was ground into powder by a mortar. This sample was sealed in the gasket hole together with pressure medium and small ruby tips. The stainless steel gasket was preindented beforehand and the hole of 200 μmϕ is made in the center of gasket by a drilling machine. The pressure transmitting medium of mixture of methanol, ethanol and water in the volume ratio of 16: 3: 1 was used to keep the hydrostaticity in the sample room. It was reported that the medium keeps the hydrostaticity at least up to 14.5 GPa (Fujishiro et al. 1982). In the present study, the quasi-hydrostatic condition appeared to be kept up to 20.1 GPa, judging from the constant FWHM of ruby R_2 line up to 20.1 GPa (Fig. 3.5.)

3.3.4 Diffraction intensity measurement

In-situ high-pressure X-ray diffraction was performed at the powder X-ray diffraction line of BL-18C in Photon Factory. The optics is shown in Fig. 3.6. The diffraction profiles was taken by

the angular dispersive method. The synchrotron source was monochromatized to the wavelength of 0.6199 Å and was converged by the Pt-coated mirror. The incident beam, which was collimated to the size of 80 μmϕ, radiated the sample through the diamond anvil. The diffracted beam was detected by an imaging plate (IP) (250 mm x 200 mm) which has the high dynamic range over ~10^5 and high sensitivity of X-ray photons. The distance between the IP and sample was about 200 mm, which covered 2θ range of 32°. The sample was exposed during 30 min. ~ 1 hour for each measurement. The high pressure data was taken at the pressures from 8.6 to 20.1 GPa with an interval of about 1.5 GPa.

The two-dimensional intensity data were transformed into digital counts by IP reader (Fuji, BAS2000). The intensities were integrated along Debye-Scherrer rings and converted to one-dimensional diffraction pattern with Powder pattern analyzer for imaging plate, PIP (Fujihisa and Aoki 1998). Peak positions were determined on PIP. Lattice parameters of $FeGeO_3$ between 8.6 GPa and 15.4 GPa were determined by the least squares method using at least 16 reflections in each X-ray diffraction pattern.

3.3.5 Simulation of the diffraction pattern of the high-pressure phase

The simulation of the X-ray diffraction pattern of the high-pressure phase and the refinement of the lattice parameters were carried out on a program of RIETAN (Izumi 1993). The X-ray pattern simulation was based on the atomic parameters of the high-pressure phase of $MgGeO_3$, which was determined by MD simulation (Tsuchiya, personal communication). The lattice parameters of high-pressure phase of $FeGeO_3$ were refined with the atomic parameters fixed. In the refinement, 1301 intensity data of 2θ = 6° - 32° except 2θ range of the gasket peaks were used. The intensity correction due to the X-ray absorption by diamond anvils and sample was performed in consideration of the X-ray beam path. After the correction, the parameters were

refined in the following order: (1) Scale factor and background parameters, (2) Profile parameters, (3) lattice parameters. Some profile parameters, which originates in the instrumental broadening, were determined on the basis of the refinement results of X-ray pattern of clinopyroxene at 8.6 GPa. The isotropic thermal parameters for Fe, Ge and O of the high-pressure phase were fixed at the refined values of clinopyroxene by the single crystal diffraction, to avoid the divergence of these parameters.

3.4 High-pressure single crystal X-ray diffraction study

Single crystal X-ray diffraction have been powerful method for elucidating the detailed crystal structure. The data collection is usually performed on the 4-circle goniometer. The development of the pressure-generation technique enables the setting the miniature high-pressure cell on the goniometer, which enabled the measurement of the diffraction intensity of the sample at high pressure. In this study, the compression process of the clinopyroxene (*C2/c*) was revealed by single crystal X-ray diffraction method.

3.4.1 High-pressure cell for single crystal study

Various types of the miniature high-pressure cells for the single crystal study have been developed (Merrill and Bassett 1974, Yamaoka et al. 1979, Keller and Holzapfel 1977, Schiferl 1977, Ahsbah 1984, Koepke et al. 1985, Kudoh and Takeda 1986, Werner et al. *in press*). In the present study, the four-post type DAC, which have been developed at the Schluz laboratory in Munchen University, was used. The principle of this cell design is shown in Fig. 3.7 (Werner 1996). It had two opposed diamond anvils with the culet size of 400 μmϕ and of 600 μmϕ. Each anvil was supported by the beryllium backing plate which was transparent for the X-rays. The cell opened conically at both sides by 100 °. The wide opening angle enabled the intensity measurements of many *hkl* reflections over wide reciprocal space. The diamonds were fixed on

the backing plates by a spring and a bayonet catch. The diamonds and backing plates were mounted in the central metal hole of DAC. This hole was larger than the beryllium plate disk by 0.2 mm. The mechanical stability of the beryllium plates were increased by the avoidance of any sideward stress on the plates. The parallelism of the culets of diamond anvils were kept by the four guide pins.

The gasket of spring steel No. 4310 was preindented up to 80 μm in thickness beforehand. After the preindentation, the gasket was removed from DAC and was fixed on the guide of a spark erosion system. A sample hole of 250 μmϕ was made in the center of the gasket. The gasket was set again in the center of DAC with the aid of a brass ring. The single crystal with the size of 80 × 80 × 40 μm was sealed in the gasket hole together with pressure maker (ruby crystal) and the pressure transmitting medium (the mixture of methanol and ethanol in the volume ratio of 4 : 1).

3.4.2 Diffraction intensity measurement

In the diffraction intensity measurements using DAC, the restriction of the aperture angle of DAC reduces the number of the accessible reflections compared to an usual intensity measurement without DAC. The volume ratio of the accessible reciprocal space between the high-pressure experiment and the usual experiment, V_d/V_θ are calculated by the following relation (Merrill and Bassett 1974).

$$\frac{V_c}{V_\theta} = \frac{3}{4}\left[\sin(\alpha-\theta) + \frac{\sin\alpha}{2\sin^2\theta}(\theta - \sin\theta\cos\theta)\right]$$

where V_θ is the measurable reciprocal space within the reciprocal sphere defined by the maximum diffraction angle of 2θ in an usual experiment (without the high-pressure cell). V_c is the corresponding measurable reciprocal space defined by the aperture angle (α°) of the DAC in

high-pressure experiment. The ratio becomes 52 % when we measure the reflections up to 2θ = 100 ° with the MoK_α line ($\lambda = 0.71069$ Å).

The data collection of the sample at ambient condition was carried on Rigaku-AFC5 four-circle diffractometer at our laboratory in Osaka University. Those of the sample at high pressures were carried on Nonius CAD4 κ -type diffractometer at Munchen University in Germany. The X-ray source of MoK_α was used in both experiments. The source was generated by the sealed X-ray tube and was monochromatized by a pyrolytic graphite.

It is difficult to set the sample in DAC at the cross center of the goniometer by the optical microscope, because the difference of the refractive index between the diamond and air apparently shifts the image of the sample crystal from the real position. Therefore, the sample in the high-pressure cell was set on the diffractometer center with reference to the profiles of the direct beam through the gasket hole (Fig. 3.8) (Primary beam profile method, Werner et al. 1996). It enables the setting of the sample at the center of goniometer within an accuracy of alignment < 30 μm. Lattice parameters at high pressures were determined by the least mean squares refinements using more than 20 reflections with $2\theta > 20$ °. Each of them was centered at the four equivalent positions to reduce systematic errors introduced by the misalignment of the sample crystal on the center of the diffractometer.

The conditions of the data collections are listed in Table 3.2. The intensity data were collected at five pressure points of 0, 1.5, 4.5 7.4 and 8.2 GPa. The X-ray diffraction intensities were measured by employing the ω-scanning mode to reduce the effects of the Debye-Scherrer rings of beryllium or gasket on the integrated intensity of the diffraction peaks. The diffraction intensities were measured at the "phi-fixed" positions ($\phi = 0°$) in the high-pressure experiments instead of the "bisecting" position to increase the number of the measurable reflections. In an

structure analysis under ambient condition, the diffraction intensities are usually measured at the "bisecting" position. In the high-pressure experiments using DAC, the "bisecting" position is not preferable because the X-ray diffraction beam is often stopped by the high-pressure cell. On the other hand, the diffraction beam is less stopped at the "phi-fixed" position because the normal of the cell is always oriented to the 2 θ counter at this position (Finger and King 1978). In the data collection at 7.4 GPa, the diffraction intensity data were collected at two different ψ positions (ψ = ±0.2 °) besides at the ψ=0 ° to reduce errors caused by the decrease of the incident beam due to the Bragg reflection of the diamond anvils (Loveday et al. 1990). The X-ray diffraction intensities were measured up to 2θ = 117.6° in the ambient-pressure experiment and up to 2θ = 63 ~ 67 ° in the high-pressure experiments. All the diffraction peak profiles were checked in high pressure experiments in terms of the background height and the equivalency of the diffraction intensities of the equivalent reflections. The data reduction were carried out on REDA, a program developed by Schulz laboratory for the special purpose of high-pressure single-crystal study. The decrease of the diffraction intensities due to the X-ray absorption by the diamonds and beryllium backing plates were corrected practically with reference to the transparency of direct beam through the DAC as a function of the inclination angle of DAC. Raw intensity data were corrected for these X-ray absorptions and Lorentz-polarization factor. The absorption correction for the sample itself was negligibly small.

3.4.3 Structure refinement

All structure refinements were carried out with Fortran program for the least-squares refinement, RADY on a personal computer (Sasaki 1987). In the process, the scale factor, fractional coordinates and isotropic temperature factors of the atoms were refined. These parameters were varied in a non-linear least-squares procedures by minimizing the sum of the squares of a differences

between the observed and calculated structure factors:

$$D = \sum_i^m w_i \left(|F_o| - |kF_c| \right)_i^2$$

where w_i is the weight of the observation, k is a scale factor. Summation was taken over all the observed reflections with $|F_o| > 6\,\sigma(|F_o|)$. Each observed structure factor was weighted by the factor of $1/\sigma_i(|F_o|)^2$. The structural parameters of $FeGeO_3$ clinopyroxene (Yamanaka, personal communication) were used as the initial structural parameters. The reliability of a refinement is generally measured by the no-weighted R-factor , $R(F)$ and the weighted R-factor, $R_w(F)$:

$$R = \frac{\sum_i^m \left(|F_o| - |kF_c| \right)_i}{\sum_i^m |F_o|_i}$$

$$R_w = \sqrt{\frac{\sum_i^m w_i \left(|F_o| - |kF_c| \right)_i^2}{\sum_i^m w_i |F_o|_i^2}}$$

Atomic scattering factors and anomalous dispersion parameters were taken from the *International table for X-ray Crystallography, Vol.III* (1974). The lattice parameters, number of the reflections used for refinements and the final residuals, R and wR are listed in Table 3.2. The atomic coordinates are listed in Table 3.3. All data of the interatomic distances, polyhedral volumes and distortion parameters for polyhedra, edge distance ratios of polyhedra and tetrahedral chain angles are listed in Table 3.4.

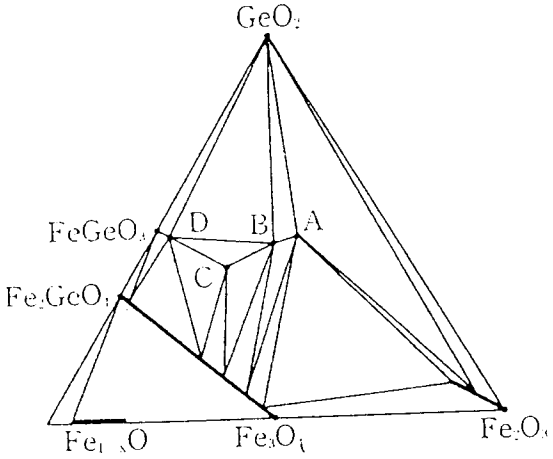

Fig. 3.1 Phase diagram of the FeO-Fe_2O_3-GeO_2 system (Takayama et al. 1981)

A : $Fe_{3.2}Ge_{1.8}O_8$, B : $Fe_{15}Ge_8O_{36}$

C : $Fe_{5.33}Ge_{2.67}O_{12}$, D : $Fe_{1.07}Ge_{0.93}O_3$

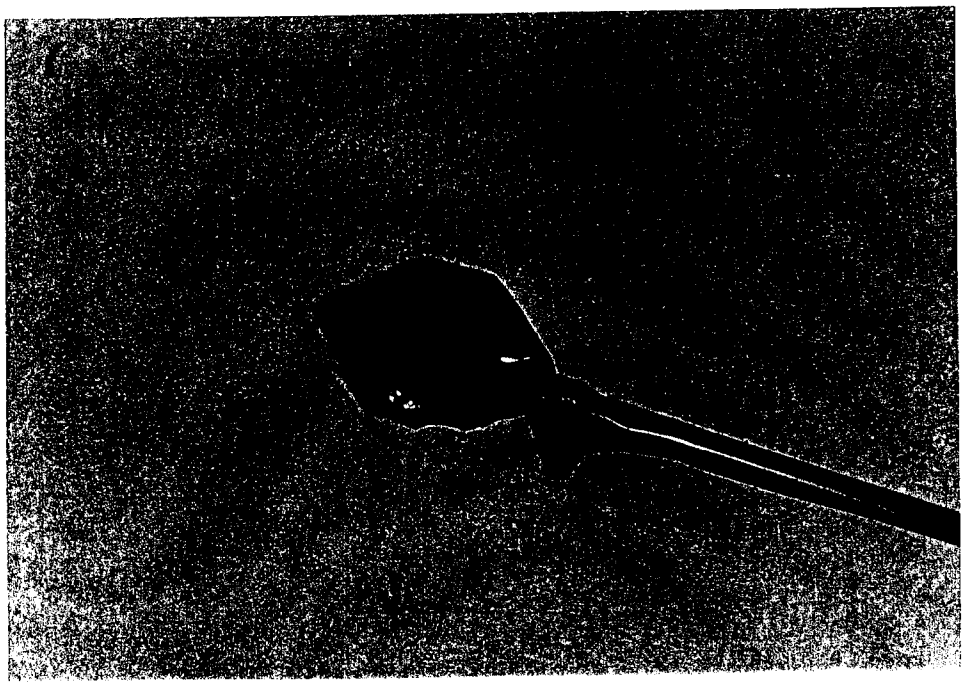

Fig. 3.2 Synthesized sample of $FeGeO_3$.

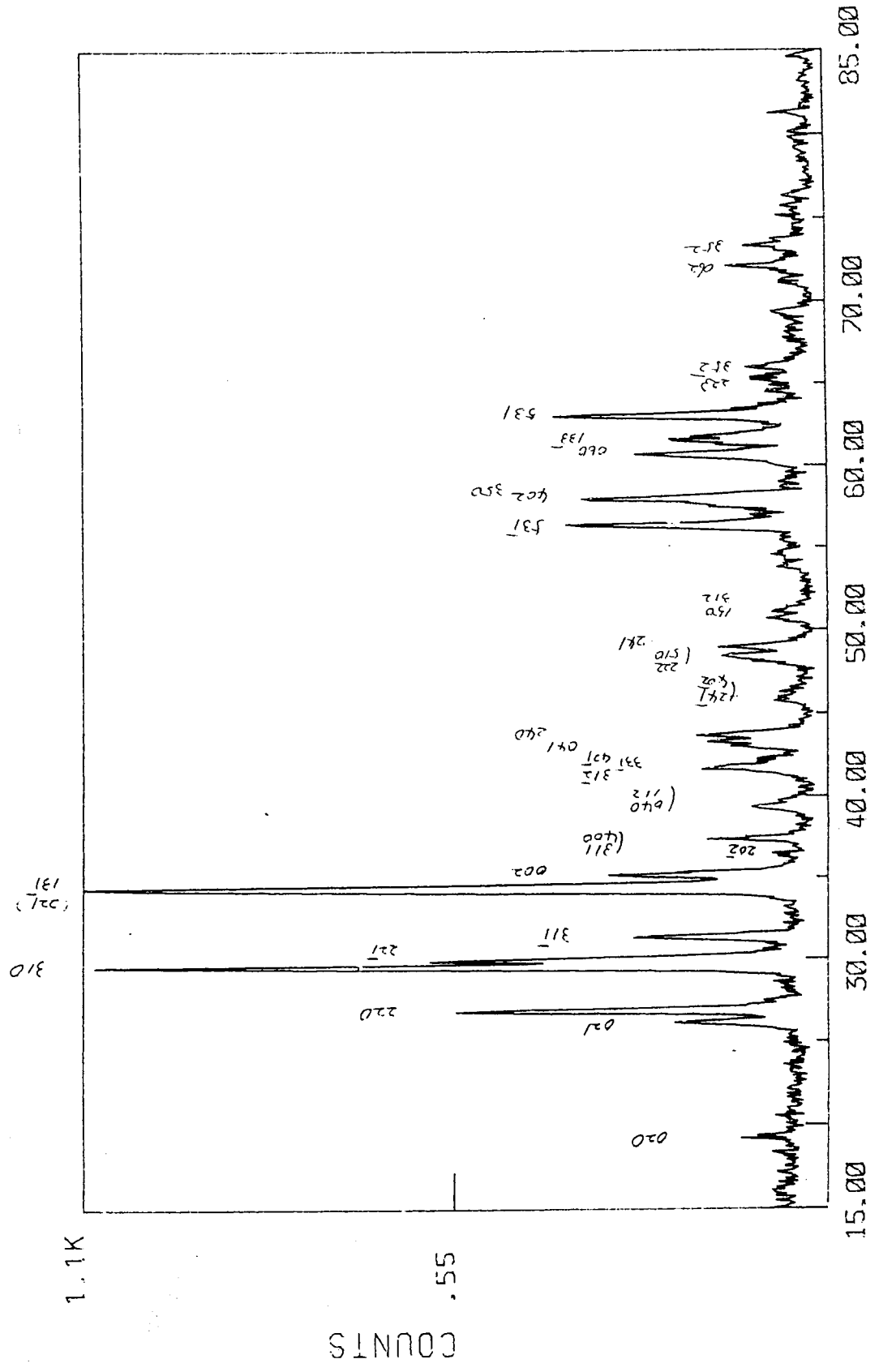

Fig. 3.3 X-ray powder pattern of synthesized sample of $FeGeO_3$.

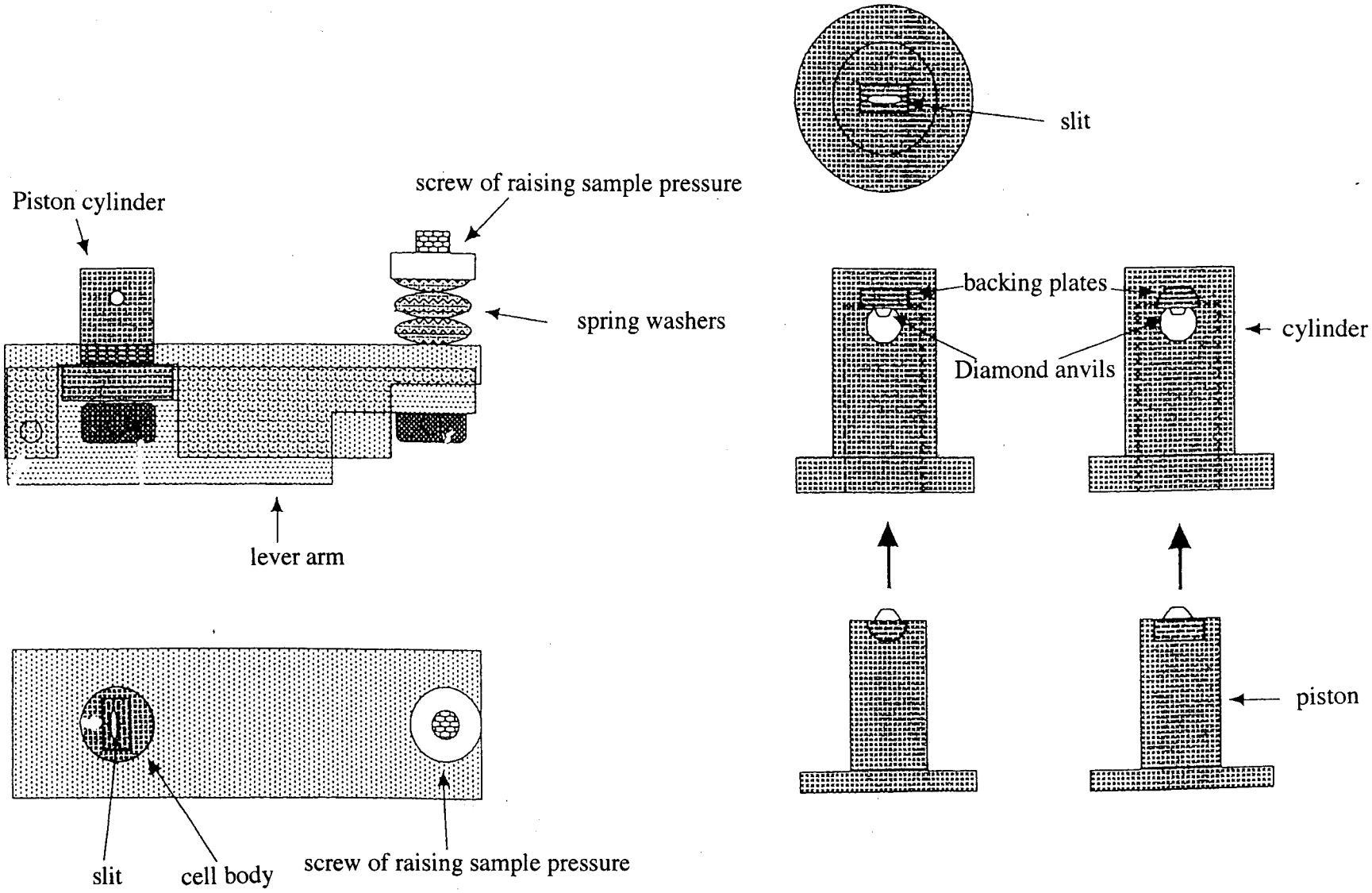

Fig. 3.4 Schematic view of the lever-spring type DAC.

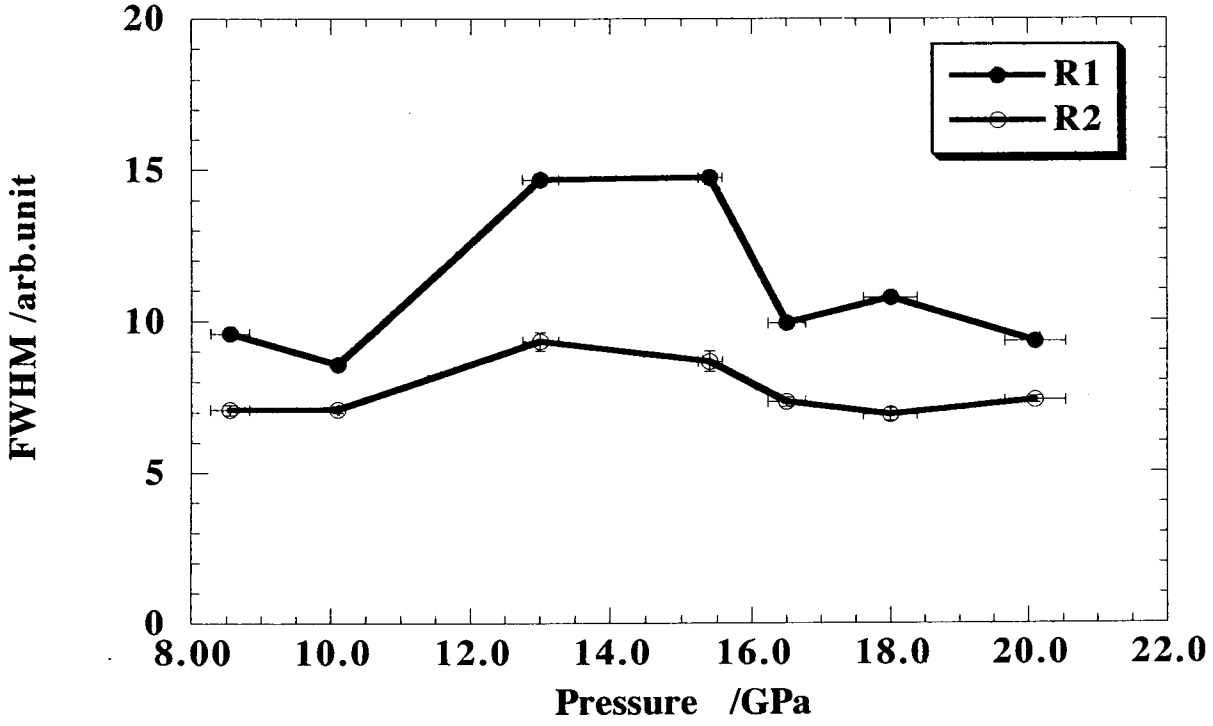

Fig. 3.5 FWHM of the ruby fluorescent peaks of R_1 and R_2 lines.

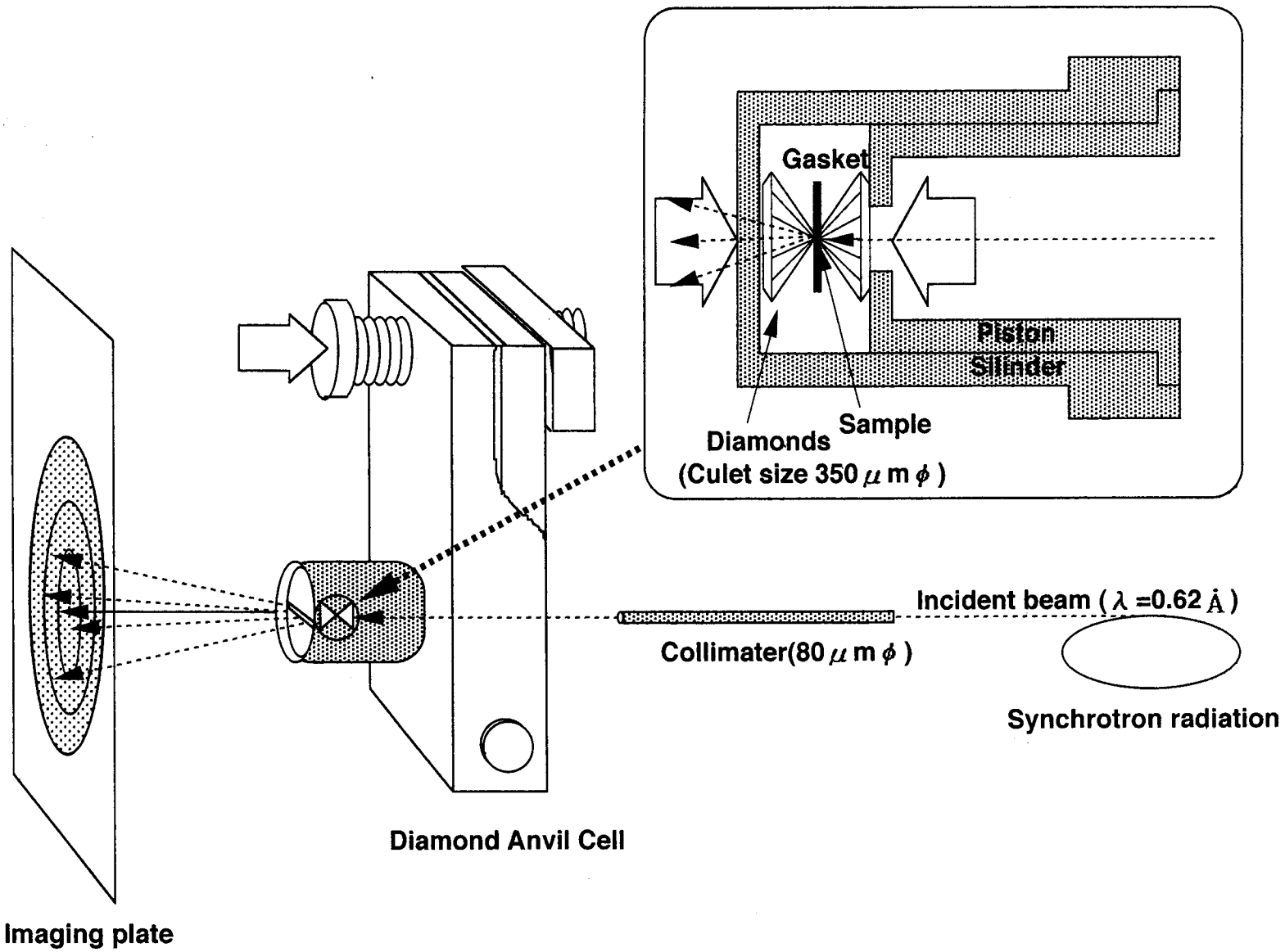

Fig. 3.6 Optics of the high-pressure angle-dispersive X-ray diffraction system installed at BL-18C.

(a)

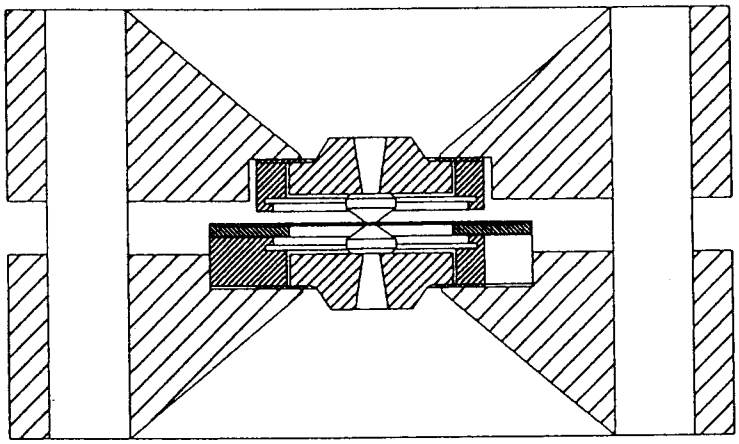

(b)

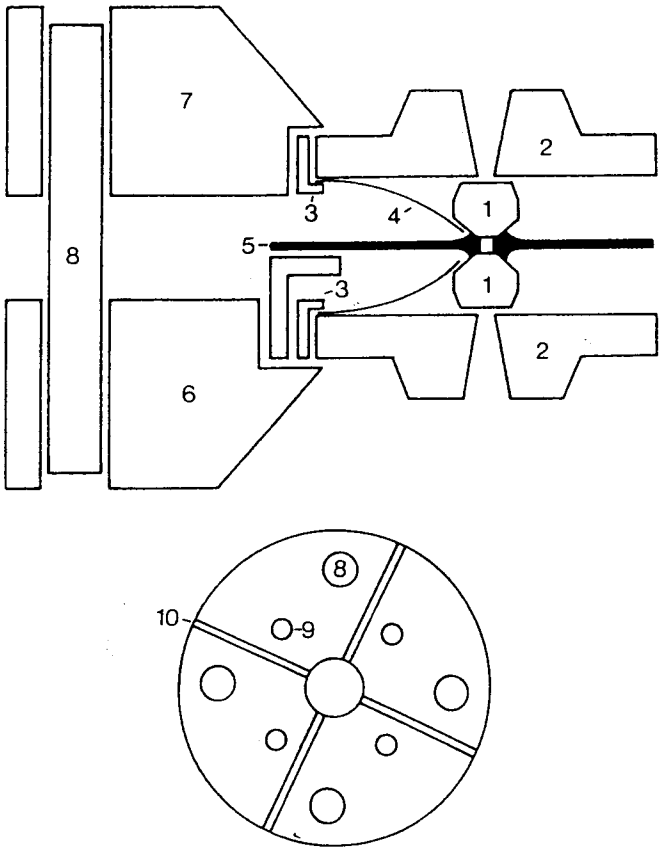

Fig. 3.7 Schematic view of the four-post type diamond anvil cell (Werner 1997).
(a) During the compression.
(b) Constituents of the cell. (1) diamond anvils, (2) beryllium backing plate, (3) bayonet catch (4) springs for fixing the diamond anvils, (5) gasket, (6) top half of cell body, (7) bottom half of cell body, (8) rotating screws for raising sample pressure.

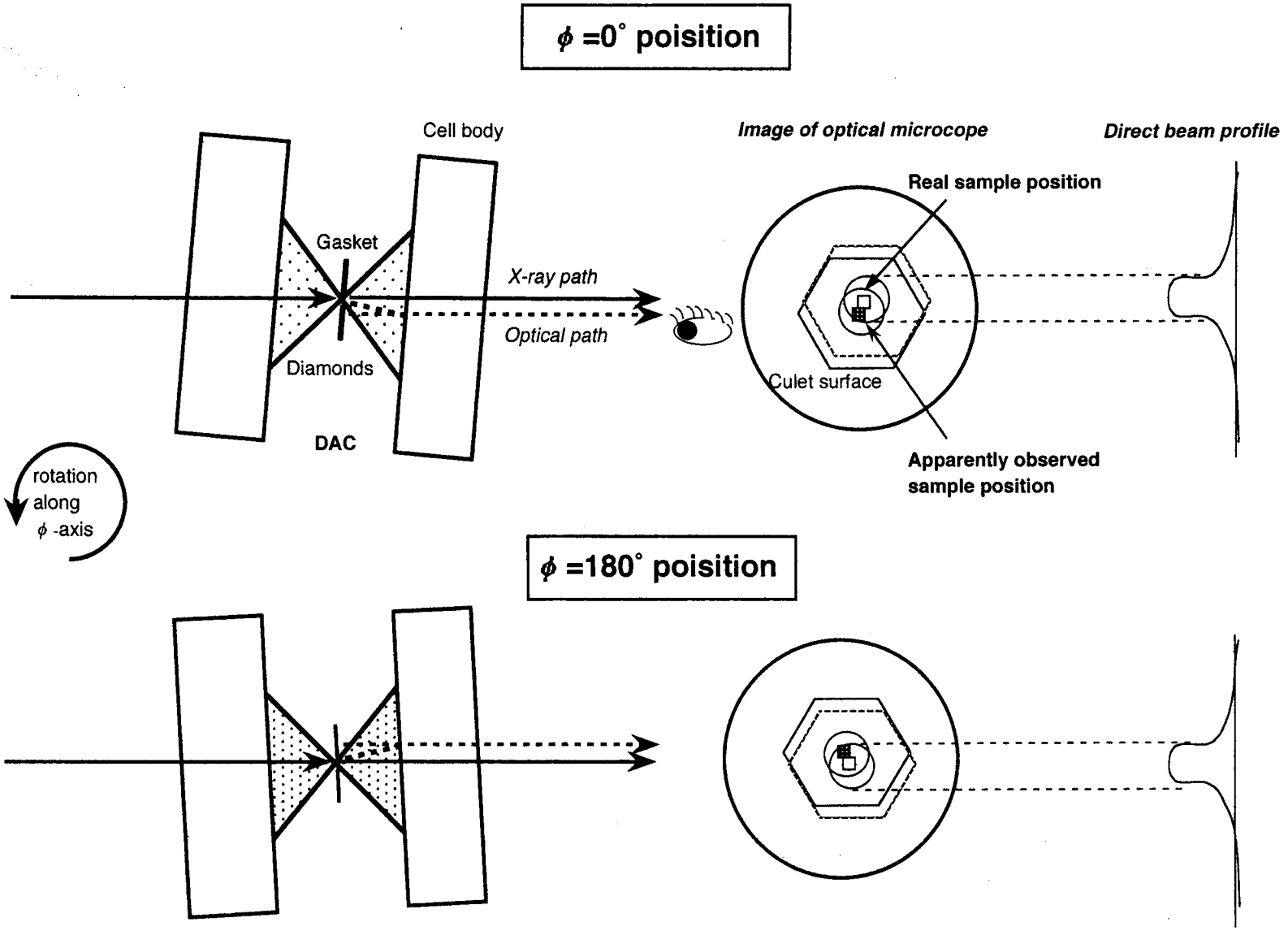

Fig. 3.8 Schematic view of primary beam method

Table 3.1 d-values of synthesized sample of $FeGeO_3$

$h\,k\,l$	d_{obs}(Å)	d_{std}(Å)	$\Delta d/d_{std}$
0 2 0	4.590	4.580	0.0022
0 2 1	3.408	3.400	0.0024
2 2 0	3.319	3.310	0.0027
3 1 0	3.019	2.973	0.0155
2 2 $\bar{1}$	2.983	2.973	0.0034
3 1 $\bar{1}$	2.853	2.849	0.0014
1 3 $\bar{1}$	2.602	2.593	0.0035
0 0 2	2.544	2.541	0.0012
4 0 0	2.402	2.397	0.0021
0 4 0	2.285	2.287	-0.0009
3 1 $\bar{2}$	2.165	2.161	0.0019
3 3 $\bar{1}$	2.135	2.138	-0.0014
4 2 $\bar{1}$	2.109	2.099	0.0048
0 4 1	2.086	2.086	0.0000
2 4 0	2.068	2.064	0.0019
5 1 0	1.876	1.876	0.0000
2 4 1	1.857	1.856	0.0005
5 3 $\bar{1}$	1.629	1.630	-0.0006
3 5 0	1.587	1.587	0.0000
0 6 0	1.524	1.524	0.0000
1 3 $\bar{3}$	1.505	1.505	0.0000
6 0 $\bar{2}$	1.500	1.498	0.0013
3 5 1	1.472	1.473	-0.0007
3 5 $\bar{2}$	1.413	1.413	0.0000

Observed lattice parameters:
$a = 9.801(27)$ Å, $b = 9.145(19)$ Å, $c = 5.097(20)$ Å, $\beta = 101.95(39)^\circ$
Lattice parameters of JCPDS(#35-1265) card:
$a = 9.793(2)$ Å, $b = 9.145(1)$ Å, $c = 5.195(1)$ Å, $\beta = 101.85(2)^\circ$

Table 3.2 Lattice parameters (Å), condition of data collection and factors of refinements

Pressure(GPa)	10^{-4}	1.5	2.9	4.1	4.5	5.4	6.0	7.4	8.2	ideal [r (O) = 140 Å]*
a (Å)	9.798(2)	9.746(1)	9.714(7)	9.682(6)	9.651(5)	9.649(10)	9.636(4)	9.600(5)	9.583(3)	$2\sqrt{11}r$ =9.287
b (Å)	9.140(1)	9.084(1)	9.043(3)	9.014(1)	8.988(1)	8.962(4)	8.946(1)	8.912(1)	8.883(3)	6r =8.400
c (Å)	5.205(1)	5.177(1)	5.156(6)	5.141(2)	5.136(1)	5.110(3)	5.119(1)	5.108(1)	5.093(2)	$2\sqrt{3}r$ =4.850
ß (°)	101.80(1)	101.52(2)	101.27(1)	101.11(5)	100.97(2)	100.85(10)	100.82(2)	100.67(2)	100.56(4)	$\tan^{-1}(-4\sqrt{2})$=100.025
a/b	1.072	1.073	1.074	1.074	1.074	1.077	1.077	1.077	1.079	$\sqrt{11}/3$ =1.1055
c/b	0.569	0.570	0.570	0.570	0.571	0.570	0.572	0.573	0.573	$1/\sqrt{3}$ =0.5774
V(Å^3)	456.3(1)	449.1(1)	444.2(6)	440.3(3)	437.3(3)	434.0(6)	433.4(2)	429.5(2)	426.2(2)	$96\sqrt{2}r^3$ =372.54
Space group					*C2/c*					
Dx (g/cm^3)	5.14	5.22	5.28	5.33	5.36	5.40	5.41	5.46	5.50	6.29
Radiation used					MoK_α					-
Monochrometer					graphite					-
Crystal size (μm^3)	140x110x105	←			80 x 80 x 40				→	-
High-pressure cell	No cell	←			Modified Merrill-Basset DAC				→	-
Diffractometer	Rigaku AFC-5R	←			Nonius CAD4				→	-
Scan type	ω	ω	-	-	ω	-	-	ω		-
Scan width, $\Delta\omega(°) = A + B\tan\theta$										
(A, B)	(1.30, 0.35)	(0.61, 0.47)	-	-	(0.61, 0.47)	-	-	(0.61, 0.47)	(0.61, 0.47)	-
Scan position	bisecting	←			phi fixed				→	-
(ψ position)	-	(0 °)	-	-	(0 °)	-	-	(0 °, ±0.2 °)	(0 °)	-
2θ range (°)	117.6	67.6	-	-	63.3	-	-	67.9	63.4	-
No. of reflections	2763	1083	-	-	978	-	-	2821	957	-
No. of reflections after averaging with $\lvert F_o\rvert > 6\sigma(\lvert F_o\rvert)$	1145	274	-	-	253	-	-	232	303	-
R (%)	5.77	6.67	-	-	5.57	-	-	5.11	6.93	-
wR (%)	5.97	8.02	-	-	7.06	-	-	5.16	6.19	-
Weighting scheme					$1/\sigma^2(\lvert F_o\rvert)$					

* Ionic radius of oxygen is based on Shannon (1976).

Table 3.3 Atomic coordinates of the observed and ideal pyroxenes

		0 GPa	1.5 GPa	4.5 GPa	7.4 GPa	8.2 GPa	ideal
Fe1	x	0.0	0.0	0.0	0.0	0.0	0.0
	y	0.9076(1)	0.9084(3)	0.9101(3)	0.9111(3)	0.9115(2)	11/12
	z	0.25	0.25	0.25	0.25	0.25	1/4
	B_{eq}	0.56(1)	1.48(5)	1.43(5)	1.49(4)	1.32(4)	
Fe2	x	0.0	0.0	0.0	0.0	0.0	0.0
	y	0.2709(1)	0.2715(3)	0.2723(3)	0.2727(3)	0.2728(2)	1/4
	z	0.25	0.25	0.25	0.25	0.25	1/4
	B_{eq}	0.54(1)	1.45(6)	1.38(6)	1.48(5)	1.26(4)	
Ge	x	0.3006(1)	0.3011(4)	0.3015(3)	0.3023(3)	0.3022(3)	5/16
	y	0.0925(1)	0.0927(2)	0.0936(2)	0.0941(2)	0.0943(1)	1/12
	z	0.2161(1)	0.2155(3)	0.2145(3)	0.2138(2)	0.2136(2)	3/16
	B_{eq}	0.362(6)	1.38(4)	1.27(4)	1.41(3)	1.27(3)	
O1	x	0.1186(3)	0.1193(22)	0.1181(23)	0.1193(20)	0.1197(17)	1/8
	y	0.0899(4)	0.0891(9)	0.0910(10)	0.0910(9)	0.0898(7)	1/12
	z	0.1388(6)	0.1366(18)	0.1350(18)	0.1360(15)	0.1340(15)	1/8
	B_{eq}	0.54(4)	1.52(18)	1.37(17)	1.39(14)	1.49(14)	
O2	x	0.3840(4)	0.3875(21)	0.3860(23)	0.3806(21)	0.3820(16)	3/8
	y	0.2402(4)	0.2418(11)	0.2440(10)	0.2465(10)	0.2463(8)	1/4
	z	0.3833(7)	0.3845(18)	0.3879(18)	0.3867(17)	0.3848(14)	3/8
	B_{eq}	0.58(5)	1.87(20)	1.47(17)	1.67(16)	1.63(14)	
O3	x	0.3583(4)	0.3601(24)	0.3645(22)	0.3654(21)	0.3629(15)	3/8
	y	0.0647(4)	0.0661(10)	0.0657(10)	0.0656(9)	0.0680(7)	1/12
	z	0.9161(7)	0.9127(20)	0.9134(19)	0.9098(17)	0.9081(14)	7/8
	B_{eq}	0.58(5)	1.57(19)	1.44(18)	1.63(17)	1.37(14)	

Table 3.4 Interatomic distances (Å), polyhedral volmes (Å^3) and distortion parameters for polyhedra, edge distance ratios of polyhedra and tetrahedral chain angles (°).

Pressure (GPa)	10^{-4}	1.5	4.5	7.4	8.2
Fe1-O1(1, 2)	2.176(4)	2.159(16)	2.133(17)	2.114(15)	2.103(17)
-O1(3, 4)	2.117(3)	2.104(22)	2.086(25)	2.089(26)	2.078(44)
-O2(5, 6)	2.107(4)	2.070(16)	2.058(17)	2.062(17)	2.047(19)
Mean Fe1-O	2.133(3)	2.111(18)	2.092(20)	2.088(19)	2.076(27)
Mean O-O	3.014(4)	2.977(25)	2.956(28)	2.937(27)	2.934(38)
Volume	12.79(3)	12.39(18)	12.06(19)	12.04(17)	11.84(14)
Q.E	1.0086(2)	1.0084(15)	1.0085(16)	1.0057(14)	1.0050(12)
A.V	28.5(8)	27.8(51)	28.4(54)	19.3(48)	17.0(40)
Fe2-O1(1, 2)	2.168(4)	2.171(16)	2.135(17)	2.126(15)	2.134(17)
-O2(7, 8)	2.014(3)	1.993(21)	1.978(25)	2.000(27)	1.999(43)
-O3(7, 8)	2.329(4)	2.281(19)	2.225(19)	2.192(19)	2.183(22)
Mean Fe2-O	2.170(4)	2.148(19)	2.113(20)	2.106(20)	2.105(27)
Mean O-O	3.069(6)	3.036(27)	2.985(28)	2.981(28)	2.972(38)
Volume	13.41(4)	12.99(16)	12.37(16)	12.28(14)	12.27(11)
Q.E	1.0145(3)	1.0149(12)	1.0135(13)	1.0105(12)	1.0109(9)
A.V	29.7(7)	32.8(29)	32.6(31)	28.1(27)	29.7(22)
Ge-O1(1)	1.746(3)	1.738(23)	1.739(23)	1.728(21)	1.722(23)
-O2(1)	1.720(3)	1.736(14)	1.735(15)	1.715(14)	1.710(18)
-O3(1)	1.784(4)	1.790(18)	1.784(18)	1.787(17)	1.774(23)
-O3(4)	1.797(3)	1.794(12)	1.796(12)	1.780(12)	1.784(15)
Mean Ge-O	1.762(3)	1.765(16)	1.764(17)	1.753(16)	1.748(20)
Mean O-O	2.872(5)	2.876(26)	2.874(28)	2.863(26)	2.848(33)
Volume	2.782(7)	2.792(35)	2.785(35)	2.742(32)	2.716(26)
Q.E	1.0058(2)	1.0069(6)	1.0069(7)	1.0056(6)	1.0059(5)
A.V	25.4(7)	30.9(28)	30.5(30)	24.2(27)	26.2(21)
Void space (Å^3)	329.2	325.2	317.3	310.3	308.1
Edge distance ratio of polyhedra					
d_{tet}/d_{oct} *	0.944(2)	0.957(12)	0.967(13)	0.967(13)	0.965(17)
Tetrahedral chain angles					
O3-O3-O3	131.10(27)	130.24(67)	130.58(67)	130.81(60)	129.28(47)
Ge-O3-Ge	120.14(22)	119.0(10)	117.90(93)	117.88(88)	117.86(65)
Tilting angle†	5.8	6.1	4.8	3.3	4.2

Note: Standard deviations are given in parentheses.
* $d_{tet}/d_{oct} = \overline{O\text{-}O}_{tet}/[(\overline{O\text{-}O}_{M1oct} + \overline{O\text{-}O}_{M2oct})/2]$.
† Angle between the normals of basal plane of a tetrahedron and of the *bc*-plane

4. Results

4.1 Transformation process of $FeGeO_3$ under high pressure

4.1.1 Transition process under hydrostatic pressure condition at room temperature

X-ray diffraction patterns at the pressures up to 20.1 GPa under room temperature and hydrostatic condition are shown in Fig. 4.1.1. No remarkable change is observed up to 10.1 GPa. All diffraction peaks is indexed as a clinopyroxene structure (*C2/c*). The refined lattice parameters and the estimated standard deviations at high pressures are shown in Table 4.1.1. The bulk modulus and the derivative are respectively determined as K_0 = 89.4 (94) GPa, K_0' = 9.1(19) by fitting of the Birch-Murnaghan equation of state. In this fitting, the cell volumes determined by the high pressure single crystal study in chapter 4.3 are also used.

The new peaks, which are shown by the symbol of "*" in Fig. 4.1.1, appeared at 13.0 GPa. Here, the newly observed phase is named $FeGeO_3$ (II). The diffraction intensity of $FeGeO_3$ (II) increases gradually with pressure, together with the decrease of that of the clinopyroxene phase. The diffraction patterns of these phases are observed in the wide pressure range of from 13.0 GPa to 20.1 GPa. Almost all the diffraction peaks of the $FeGeO_3$ clinopyroxene (*C2/c*) disappears at 20.1 GPa. The pattern at 20.1 GPa appears to be only from the single phase of $FeGeO_3$ (II). The lattice parameters of $FeGeO_3$ (II) are refined on the basis of this patterns, which is mentioned in the next section. After the release of pressure, the diffraction peak of the initial clinopyroxene phase retains their intensity (Fig. 4.1.2). The peak profile of the recovered phase is slightly broader than those before the compression. It suggests that the phase transition between clinopyroxene and high-pressure phase is reversible.

The pressure distribution of the X-ray radiated area ($80\,\mu m\,\phi$) is at most 15 % of the maximum pressure and, therefore, it is about 3.0 GPa at 20.1 GPa. The above mentioned wider

pressure range of the transformation than the pressure distribution suggests that the presently observed gradual transformation is not due to the pressure distribution of the radiated area, but is the substantial nature of the presently observed phase transformation.

The above mentioned transformation processes of $FeGeO_3$ clinopyroxene ($C2/c$) are well consistent with those of $MgGeO_3$ clinopyroxene ($C2/c$) in terms of the diffraction profile of the high-pressure phase and the pressure range of the transformation (Nagai 1995, Andrault et al. 1992). The previously reported unidentified phase of $MgGeO_3$ is considered to have the same structure as the presently observed high-pressure phase of $FeGeO_3$ (II) from the above similarity.

4.1.2 Structure refinement of the newly observed high-pressure phase

Based on the diffraction pattern obtained at 20.1 GPa, the identification of the high-pressure phase and the refinement of the lattice parameters was carried out. The space group of the high-pressure phase is not determined because of the experimental difficulty of the single crystal diffraction study above 20 GPa. First, the space group of $P\bar{1}$ is assumed in consideration of the results of the MD simulation. The cell axes of a', b', c' are taken as is shown in Fig. 4.1.3. The refinement are converged successfully. The structure of high-pressure phase does not show the possibility to have any symmetry element except $\bar{1}$. The symmetry elements of the clinopyroxene, such as C-lattice, two-fold rotation axis and c-glide along b-axis, are lost during the transformation. The above cell with the axes of a', b', c' can be reduced into another smaller cell by the following axes transformation (Fig. 4.1.3):

$$a_{hp} = \frac{a' - b'}{2}$$

$$b_{hp} = b'$$

$$c_{hp} = c'$$

where a', b', c' are the axes before the reduction and a_{hp}, b_{hp}, c_{hp} are the axes of the reduced cell.

Finally, the lattice parameters are refined based on this reduced cell (*PT*). The refinement is successfully converged and the refinement factor,R_F becomes 2.6 %. The lattice parameters of the high-pressure phase are determined as a_{hp}=6.843(28)Å, b_{hp}=8.473(35)Å, c_{hp}=4.880(5)Å, α_{hp}=89.70(19)°, β_{hp}=89.24(18)° and γ_{hp}=137.86(18)° (a'=9.334(55)Å, b',=8.473(35)Å, c'=4.880(5)Å, α'=89.70(19)°, β'=89.24(18)° and γ'=100.34(13)°). The refined parameters are listed in Table 4.1.2. The observed and simulated X-ray patterns of the $FeGeO_3$ (II) are shown in Fig. 4.1.4. The simulated pattern of high-pressure phase is coincident with the observed pattern at 20.1 GPa, though small discrepancies are observed in the diffraction intensities of some reflections of *0k0* (*k: odd*) of $FeGeO_3$ (II).

4.1.3 Volume change during the phase transformation

To check the validity of the presently determined structure as the high-pressure phase, the volume change during the transformation is investigated. The transformation pressure can not be determined definitely because the transformation occurrs continuously in the pressure range between 8.6 and 20.1 GPa. Therefore, the difference of cell volumes between the clinopyroxene and $FeGeO_3$ (II) phases at 20.1 GPa is adopted as the volume change during the transformation. The cell volume of the clinopyroxene at 20.1 GPa is estimated from the extrapolation of the compression curve of $FeGeO_3$ clinopyroxene toward 20.1 GPa using the presently determined *Ko* and *Ko'* values.

The cell volumes per one chemical formula (Z = 1) of the clinopyroxene and $FeGeO_3$ (II) phases are shown in Fig. 4.1.5. The volumes of the clinopyroxene and the $FeGeO_3$ (II) phases at about 20.1 GPa are calculated as 50.5 (7) $Å^3$/Z and 47.5 (3) $Å^3$/Z, respectively. The ratio of the volume reduction during the phase transition is 6.0 (14) %, which suggests that the presently determined structure of the high pressure phase is reasonable as a high-pressure phase. The

volume discontinuity between the clinopyroxene and $FeGeO_3$ (II) suggests that the transition is first-order type.

4.1.4 Crystal structure of the $FeGeO_3$ (II)

The projection views of the oxygen arrangement of clinopyroxene and $FeGeO_3$ (II) are shown in Fig. 4.1.6, where the structure of $FeGeO_3$ (II) is drawn on the basis of the above mentioned cell axes of a', b' , c' for the ease of the comparison of both structures. The oxygen arrangement of the $FeGeO_3$ (II) are composed of the stacking of the two-dimensionally closed packed oxygen layers. The stacking sequence of $FeGeO_3$ (II) is nearly same as the hexagonal closed packing (*HCP*), though the stacking direction is slightly inclined as shown in Fig. 4.1.6. The packing of the $FeGeO_3$ (II) is neither CCP, nor *HCP* in the strict sense. The difference of the stacking sequences is represented by the displacement vector of the stacking. The displacement vector of *CCP* is $\boldsymbol{d}_{ccp} = (+\sqrt{8/3}r, 0, -2/\sqrt{3}r)$, where r indicates the radius of the rigid sphere and the x, y, z directions are taken as shown in Fig. 4.1.6. The stacking sequence of the $FeGeO_3$ (II) phase can be approximately expressed by the alternate vectors of $\boldsymbol{d}_{hcp1} = (+\sqrt{8/3}r, +\Delta, +2/\sqrt{3}r)$, $\boldsymbol{d}_{hcp2} = (+\sqrt{8/3}r, +\Delta, -2/\sqrt{3}r)$. The y-coordinate of Δ results in the inclination of the stacking direction along y-direction in $FeGeO_3$ (II).

In the structure of $FeGeO_3$ (II), Fe^{2+} and Ge^{4+} cations occupy the highly deformed octahedral sites of the deformed *HCP*. The Fe^{2+} and Ge^{4+} cations distribute alternately along the stacking direction. Within each interstice layer between oxygen stacking layers, the Fe^{2+} and Ge^{4+} cation are aligned one-dimensionally along the c-direction of $FeGeO_3$(II) similarly to those in the clinopyroxene. The structure of $FeGeO_3$(II) are more similar to that of the ilmenite structure in terms of the oxygen packing (*HCP*) and the coordination number ($^{VI}A^{VI}BO_3$). The structure is different from ilmenite only in terms of the cation arrangements within the interstices between

oxygen layers, i.e. the structure of $FeGeO_3$ (II) is a modified structure of ilmenite with the different cation occupancies.

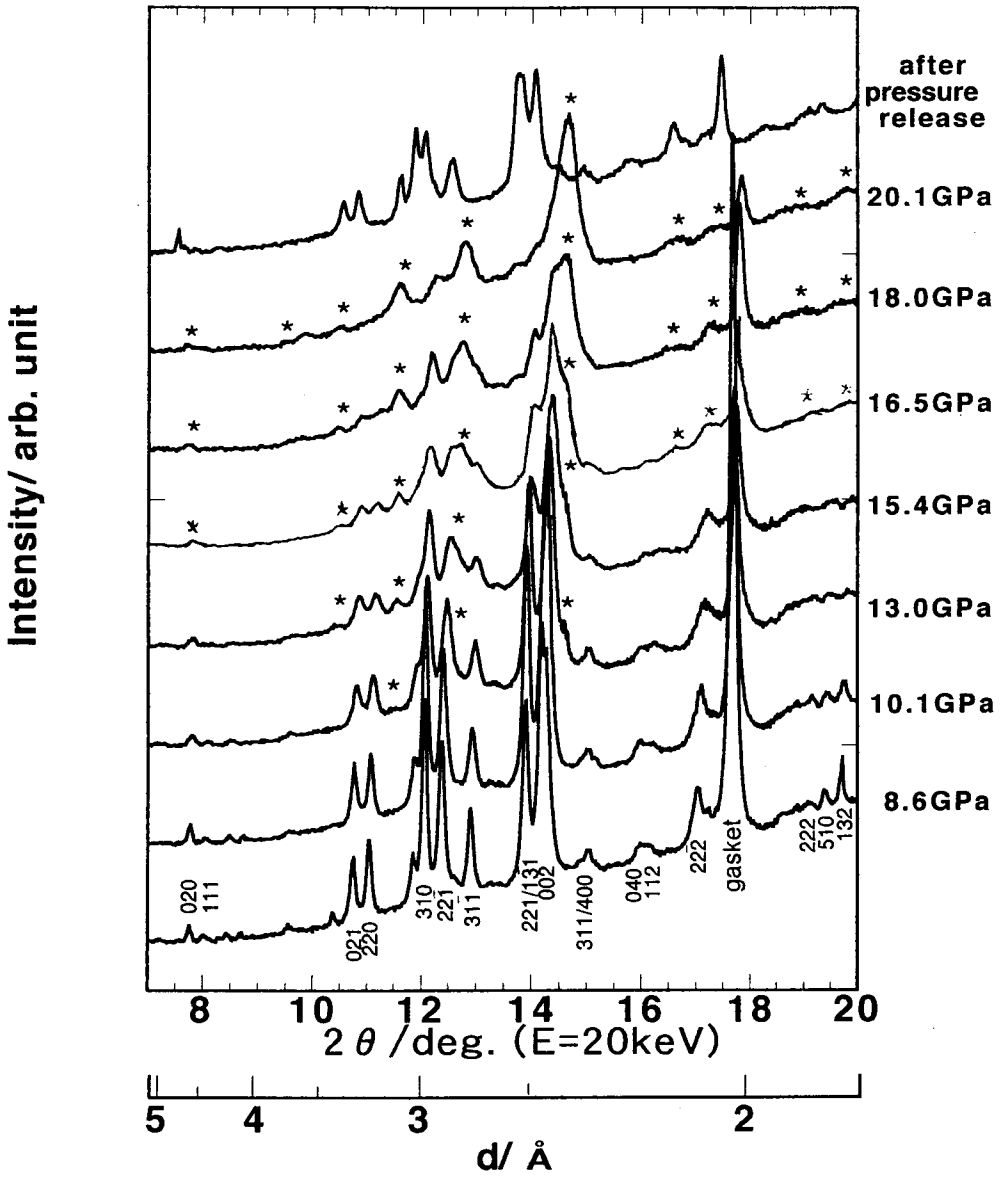

Fig. 4.1.1 X-ray diffraction patterns of $FeGeO_3$ at pressures up to 20.1 GPa and after the release of pressure.

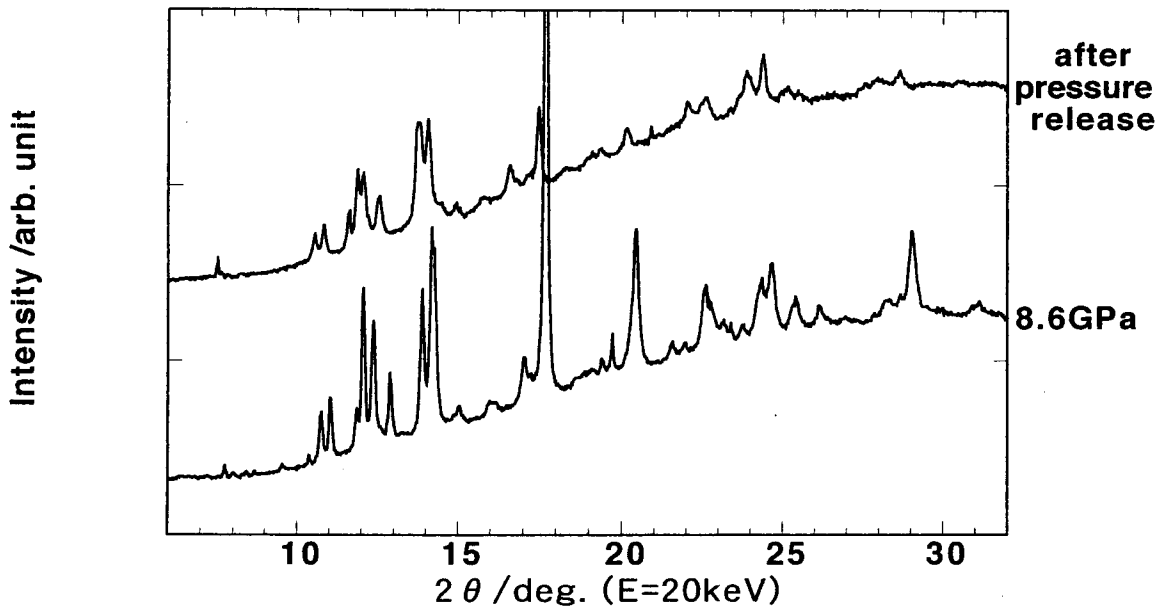

Fig. 4.1.2 X-ray pattern before the transformation and that of recovered sample from 20.1 GPa.

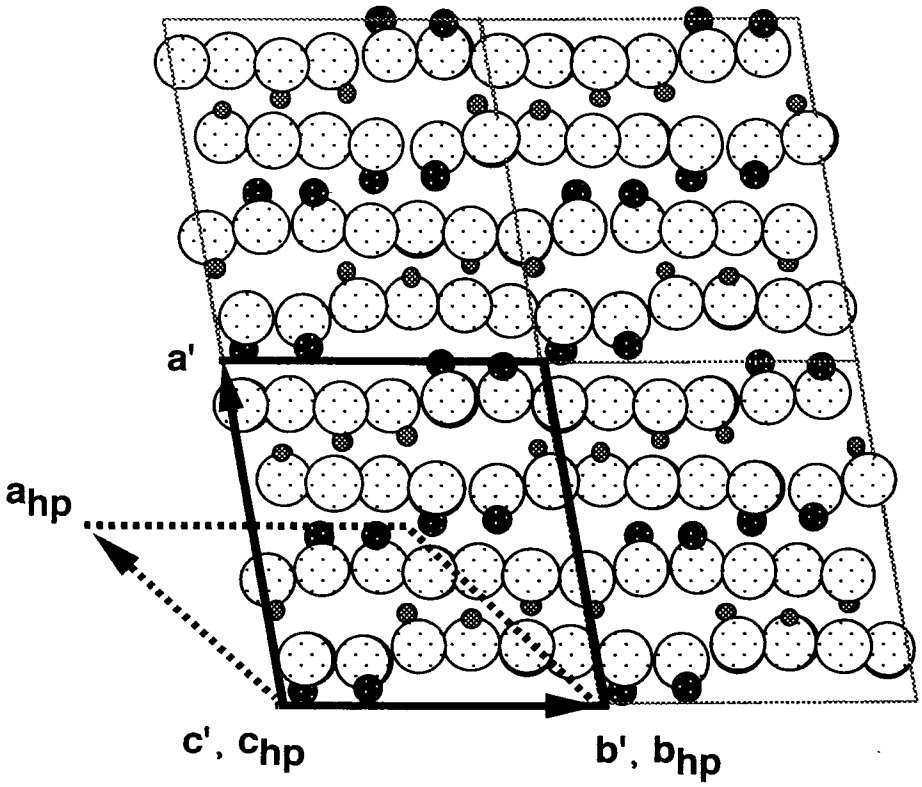

Fig. 4.1.3 Cell axes taken in the refinements.

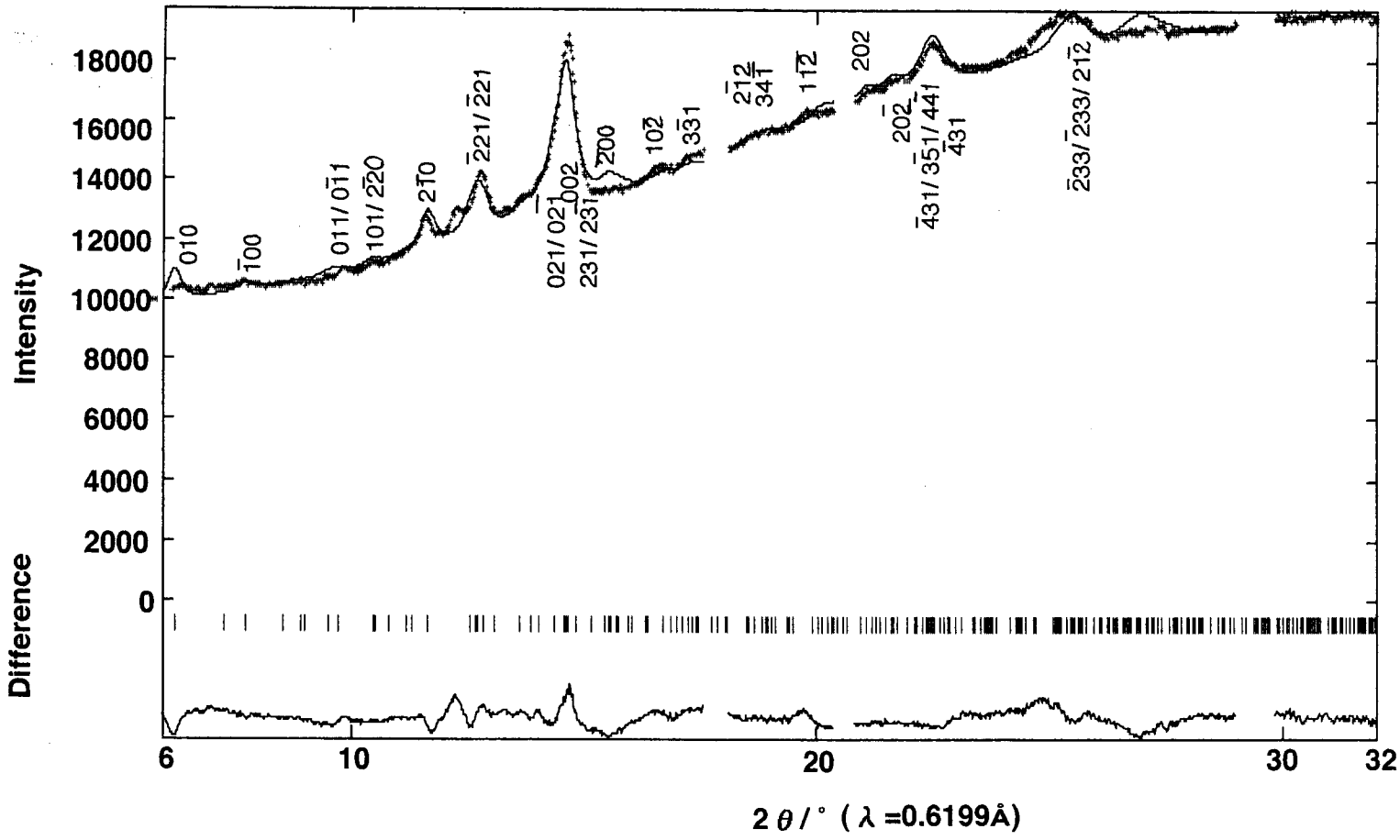

Fig. 4.1.4 Observed and simulated X-ray patterns of the $FeGeO_3$ (II)

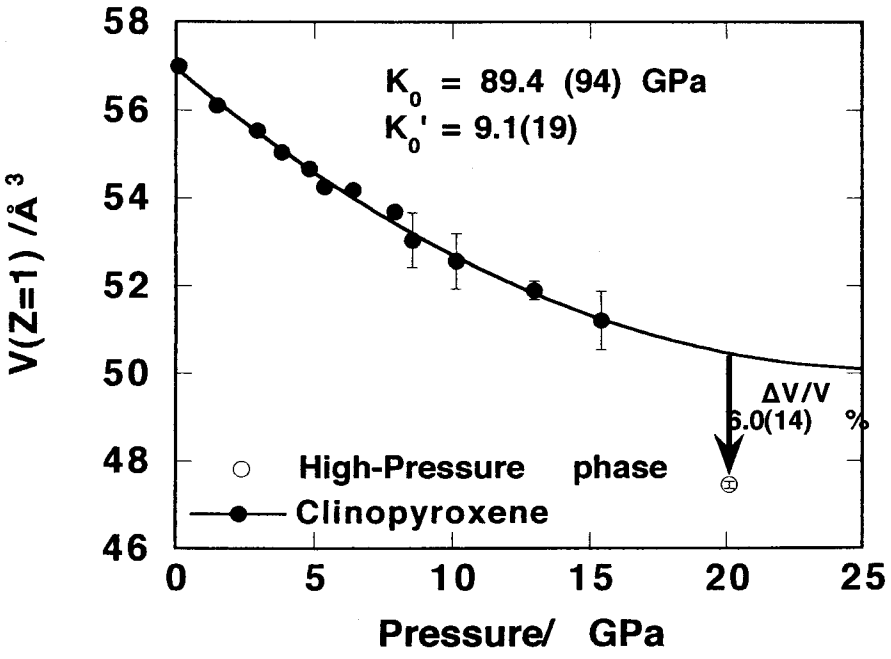

Fig. 4.1.5 Cell volumes per one chemical formula ($Z = 1$) of the clinopyroxene and $FeGeO_3$ (II)

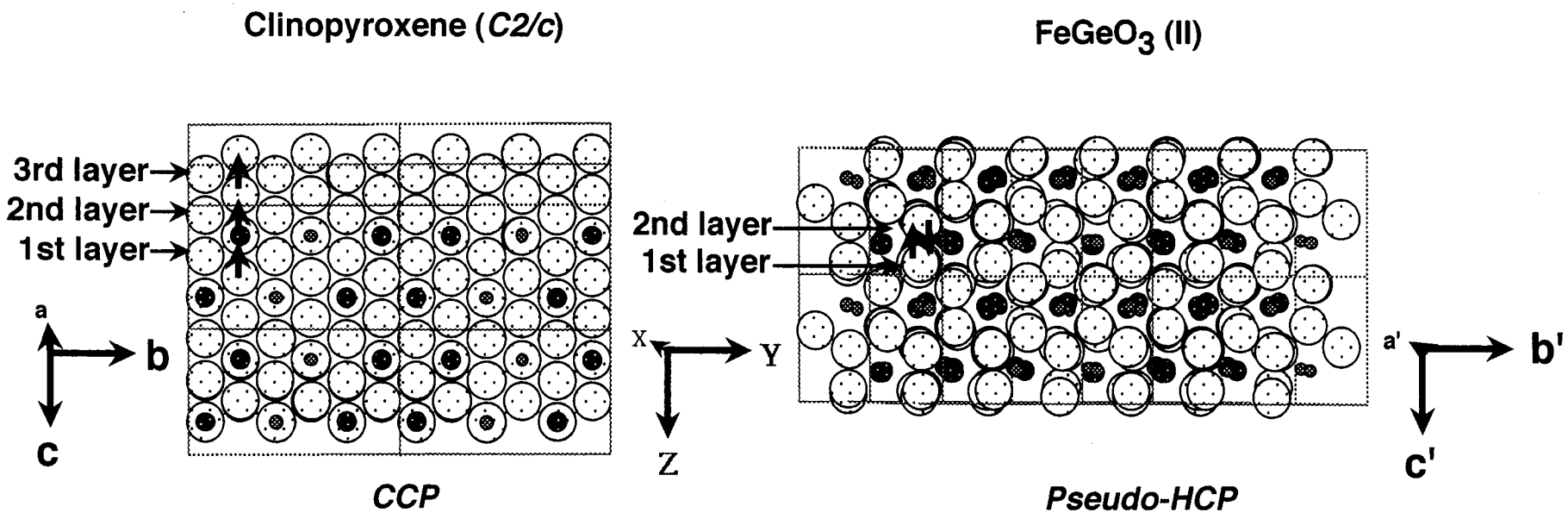

Fig. 4.1.6 (a) Schematic views of clinopyroxene and $FeGeO_3$ (II) along their stacking directions.

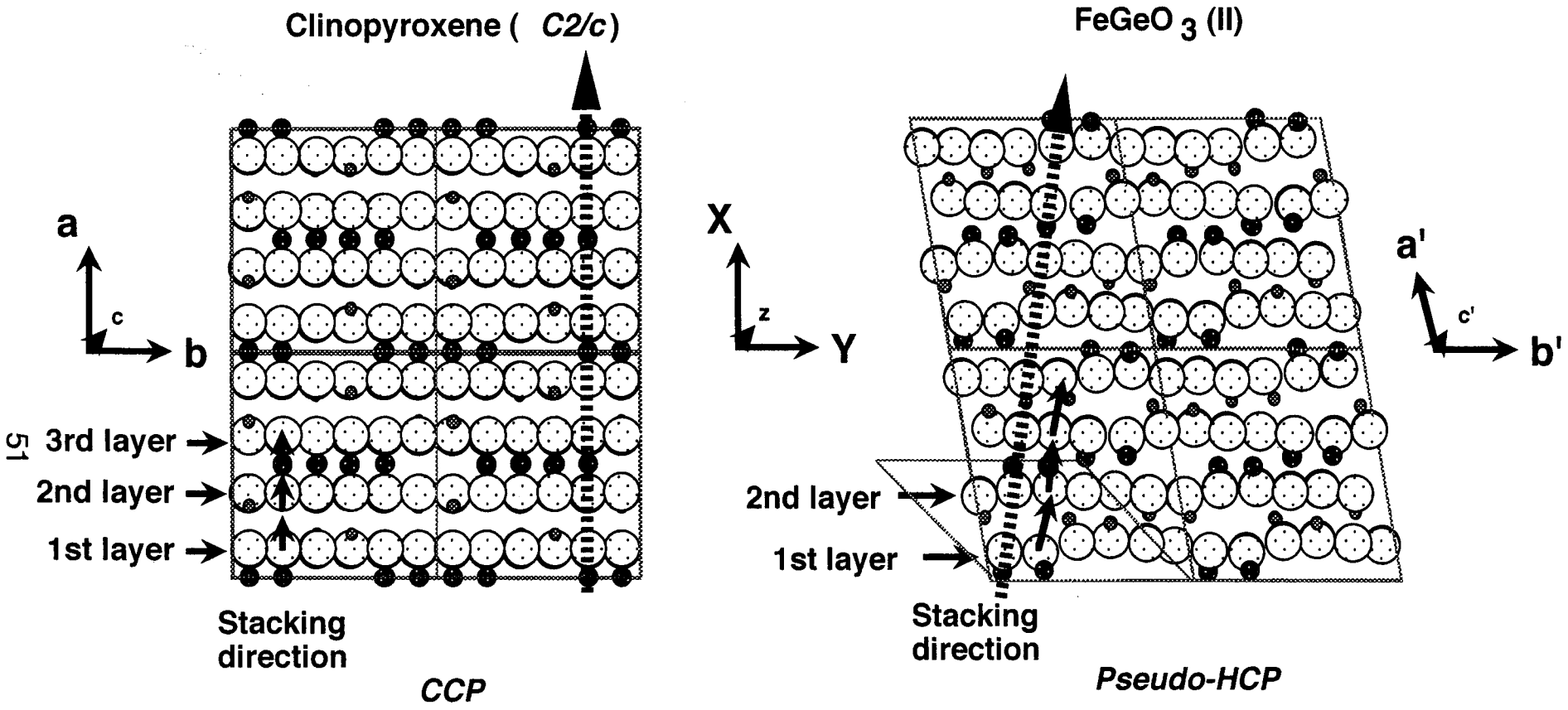

Fig. 4.1.6 (b) Schematic views of clinopyroxene and $FeGeO_3$ (II) along *c*-axes

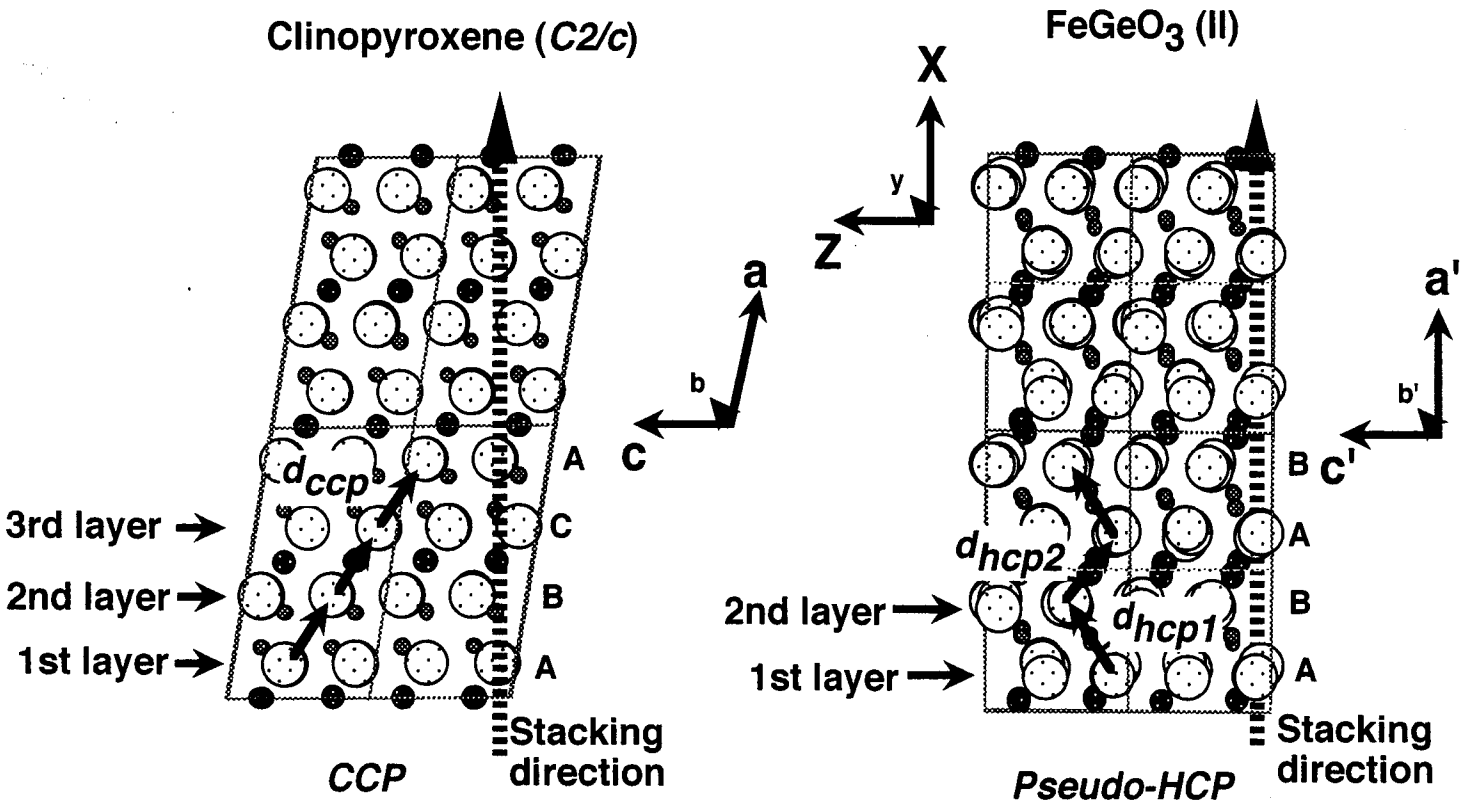

Fig. 4.1.6 (c) Schematic views of clinopyroxene and $FeGeO_3$ (II) along *b*-axes.

Table 4.1.1 Lattice parameters and the estimated standard deviations of $FeGeO_3$ clinopyroxene at high pressures

	P(GPa)	a(Å)	b(Å)	c(Å)	beta(deg.)	a/b	c/b	V(Å^3)
s.c.	0	9.7942(16)	9.1446(13)	5.1984(10)	101.866(14)	1.0710(2)	0.5685(1)	455.64(13)
s.c.	1.5	9.7464(14)	9.0835(10)	5.1747(7)	101.517(17)	1.0730(2)	0.5697(1)	448.90(11)
s.c.*	2.9	9.714(7)	9.043(3)	5.156(6)	101.27(14)	1.0742(8)	0.5702(7)	444.19(66)
s.c.*	4.1	9.682(6)	9.014(1)	5.141(2)	101.11(5)	1.0741(7)	0.5703(2)	440.27(33)
s.c.	4.5	9.651(5)	8.9882(8)	5.1357(8)	100.971(21)	1.0737(6)	0.5714(1)	437.34(25)
s.c.*	5.4	9.649(10)	8.962(4)	5.110(3)	100.85(10)	1.0767(12)	0.5702(4)	433.98(57)
s.c.	6.0	9.636(4)	8.9461(7)	5.1190(5)	100.820(16)	1.0771(5)	0.5722(1)	433.43(20)
s.c.	7.4	9.600(5)	8.9122(7)	5.1078(10)	100.666(23)	1.0772(5)	0.5731(1)	429.48(23)
s.c.	8.2	9.583(3)	8.883(3)	5.0932(15)	100.56(4)	1.0788(5)	0.5734(3)	426.22(24)
pwd	8.6	9.558(55)	8.8829(6)	5.082(35)	100.50(60)	1.076(10)	0.572(6)	424.3(49)
pwd	10.1	9.542(22)	8.831(28)	5.072(14)	100.35(25)	1.081(4)	0.574(2)	420.5(21)
pwd	13.0	9.517(20)	8.780(21)	5.046(10)	100.02(21)	1.084(3)	0.575(2)	415.2(16)
pwd	15.4	9.518(70)	8.743(67)	4.998(34)	99.90(90)	1.089(11)	0.572(6)	409.7(53)

s.c and pwd respectively represent the data determined by single crystal X-ray diffraction and powder X-ray diffraction methods.
*These data were taken by the 4-circle diffractometer in our laboratory.
Standard deviation for each value is shown in the parenthesis.

Table 4.1.2 Results of the refinement

(a) Sample (conditions) : $FeGeO_3$ (at R. T. and 20.1 GPa)

(c) Correction of diffraction intensity

(i) X-ray absorption of DAC

Linear absorption cofficient of Diamond, μ_{dia} :1.677[cm^{-1}]

Hight of diamond anvil :0.22[cm]

(ii) X-ray absorption of sample

Linear absorption cofficient of sample, μ_{FeGeO3} :139.053[cm^{-1}]

Thickness of sample :0.002[cm]

(d) Used regions of data for refinement

Used regions :6.00- 32.00

Excluded regions in the data :17.60- 18.10
:20.40- 20.80
:29.00- 29.80

(e) Fixed parameters

(i) Space group : *PT*

(ii) Peak profile function

Gaussian FWHM parameter, V : -3.227470E-02

Gaussian FWHM parameter, W : 1.398220E-03

(ii) Atomic positions

		neq*	g	n	x	y	z	B
Fe	(1)	2	1.0000	2.0000	0.05070	0.31550	0.23800	0.494
Fe	(2)	2	1.0000	2.0000	0.04595	0.11800	0.74550	0.494
Ge	(1)	2	1.0000	2.0000	0.53650	0.11475	0.74350	0.345
Ge	(2)	2	1.0000	2.0000	0.53800	0.30675	0.26550	0.345
O	(1)	2	1.0000	2.0000	0.22700	0.20030	0.10590	0.570
O	(2)	2	1.0000	2.0000	0.25300	0.40900	0.59050	0.570
O	(3)	2	1.0000	2.0000	0.28950	0.62020	0.07980	0.570
O	(4)	2	1.0000	2.0000	0.29550	0.78615	0.59600	0.570
O	(5)	2	1.0000	2.0000	0.27050	0.93650	0.05600	0.570
O	(6)	2	1.0000	2.0000	0.26800	0.08375	0.55650	0.570

neq: multiplicity of the Wyckoff position (number of equivalent points per unit cell)

n: number of equivalent atoms per unit cell

(f) Refined parameters

(i) Background

Background paramter, b1	: 14929.0	61.5910
Background paramter, b2	: 5475.91	39.4409
Background paramter, b3	: -486.275	90.7200
Background paramter, b4	: -892.430	92.3802
Background paramter, b5	: 62.2171	116.083
Background paramter, b6	: 168.705	177.815

(ii) Scale factor

Scale factor, s	: 2.354108E-05	5.215078E-07

(iii) Profile fuctions

Gaussian FWHM parameter, U	: 0.272290	4.958711E-03
Scherrer coefficient for Gaussian broadening, P	: -3.442099E-04	8.126802E-05
Lorentzian Scherrer broadening X	: 0.279502	8.591460E-03
Strain broadening, Y	: 1.17048	6.833099E-02

(vi) Lattice parameters

Lattice parameters (Å or deg.) and unit-cell volume ($Å^3$)

	a	b	c	alpha	beta	gamma	V (Z=4)
	6.843	8.473	4.880	89.70	89.24	137.86	189.8
e.s.d.	0.028	0.035	0.005	0.19	0.18	0.18	1.1

(g) R factors (%)

R_{wp}	R_p	R_e	R_I	R_F
1.57	1.17	0.80	3.76	2.16

(All these parameters are based on Izumi (1985))

4.2 TEM observation of the recovered sample

4.2.1 Purpose

In order to get the information of the mechanism of high-pressure transformation, the recovered samples from above the transformation pressure were observed by the transmission electron microscope (TEM). Their chemical compositions were also investigated by the analytical transmission electron microscopy (ATEM) to examine the possibility of the transformation into the mixture of Fe_2GeO_4 (spinel) and GeO_2 (rutile).

4.2.2 Experimental

Sample preparation

The sample for the TEM observation is usually prepared by the ion thinning method. However, it often damages the sample due to the sputtering by the high-energy gas molecule and the temperature increase of sample. In the present study, most of the samples recovered from the high pressures and room temperature condition is thought to be unstable because of the sample was mechanically compressed and deformed at room temperature. Therefore, the ion thinning was not undertaken in the present study and the samples were prepared by the following procedure. The powder sample of $FeGeO_3$ was pressurized up to the desired pressures by the Mao-Bell type DAC. The sample was recovered from the gasket hole after the duration of at least 30 hours under high-pressure condition. The recovered sample was ground by the mortar with the methanol in order to disperse the grains of the compressed sample. The dispersed fine powder was scooped up by the Cu micro grid with the size of 3 mm ϕ. The samples recovered from several pressures between 8 and 23 GPa were examined. The starting samples before the compression, which were prepared by the same procedure to the recovered sample, were also observed for the comparison.

TEM observation and chemical analysis

The samples were observed by the 200 kV TEM (HITACHI H-8000) at Kitamura laboratory in Kyoto University. The side holders with two-axis of tilt and azimuth were used. The observation was undertaken at the accelerating voltage of 160 ~ 200 kV and the filament current of 1.0 μA. The chemical composition of the samples were determined by ATEM with an energy dispersive X-ray micro analyzer (EDX: KEVEX Delta Series) system. The analyses were performed by the detection of the characteristic X-ray from the electron radiated area in the sample. The spacial resolution was about 150 nm. The diffraction images were analyzed on the C-language program coded by Tsuchiyama (personal communication).

4.2.3 Result

Observation of the starting sample

A typical example of dark-field images and the selected area diffraction images of the starting sample is shown in Fig. 4.2.1. All the diffraction patterns are indexed as clinopyroxene. No phase except clinopyroxene is not observed in the stating sample. Each clinopyroxene particle has the good crystallinity.

The results of the qualitative analyses are shown in Fig. 4.2.2, where the relative ratio of the Ge to the sum of the Fe and Ge, $I_{Ge}/I_{Fe}+I_{Ge}$ are shown. Fe and Ge element are detected at all examined points. No other chemical element is detected. Most results show that the chemical ratio of Fe : Ge are 1: 1 within the experimental error. These results suggest that the starting material has the good crystallinity and no chemical inhomogeneity.

Observation of the recovered sample from high pressure

A typical example of the dark field images and the selected area diffraction images of the sample recovered from 21 GPa is shown in Fig. 4.2.3. The diffraction image is indexed as a

clinopyroxene structure, though the spots are slightly elongated along the radius. This elongation of the diffraction spot originates in the difference of the orientations of grains in the diffraction area. This may be caused by the high-shear stress applied on the sample during the compression or the stress caused by the high-pressure transformation. The result of chemical analyses are shown in Fig. 4.2.4. The recovered samples are very weak against the converged analytical electron beam. Under such conditions, Fe or Ge elements are sometimes vaporized during the analysis. Most results shows the chemical composition of Fe : Ge = 1 : 1. These suggests that the chemical composition dose not change during the transformation. The decomposition process is not observed within the spatial resolution of TEM.

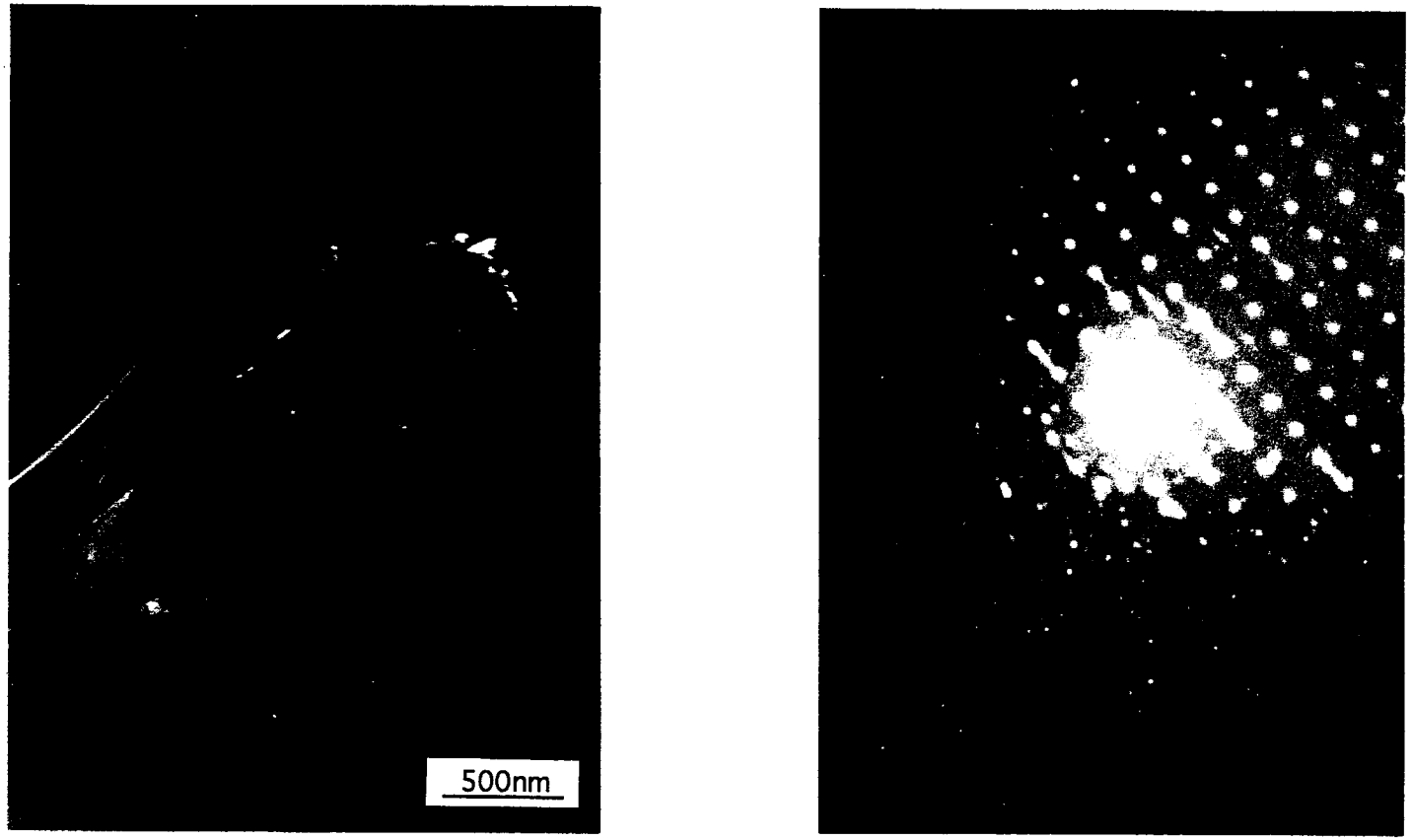

Fig. 4.2.1 A dark-field image and the selected area diffraction image of the start sample before the compression.

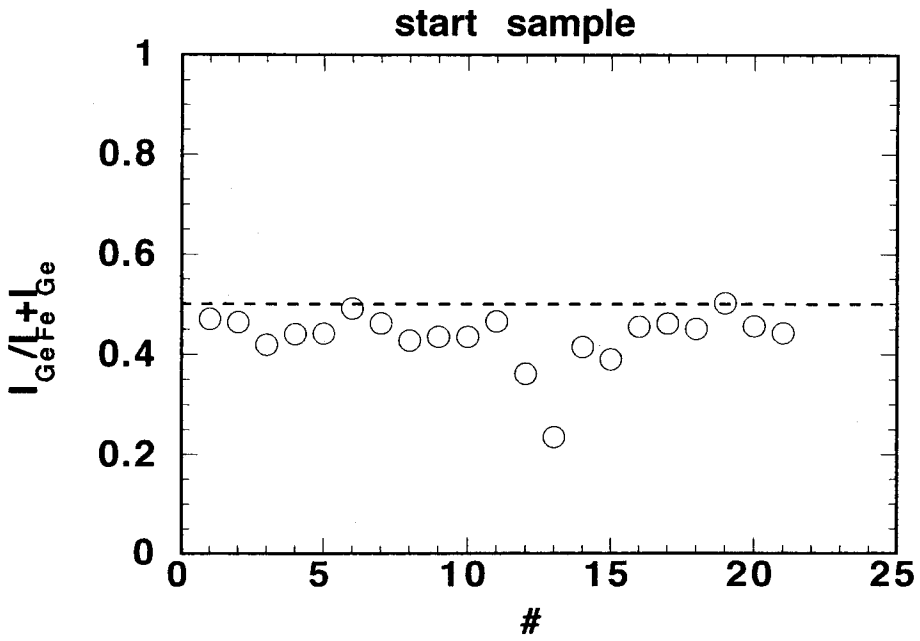

Fig. 4.2.2 Chemical compositions of the start sample

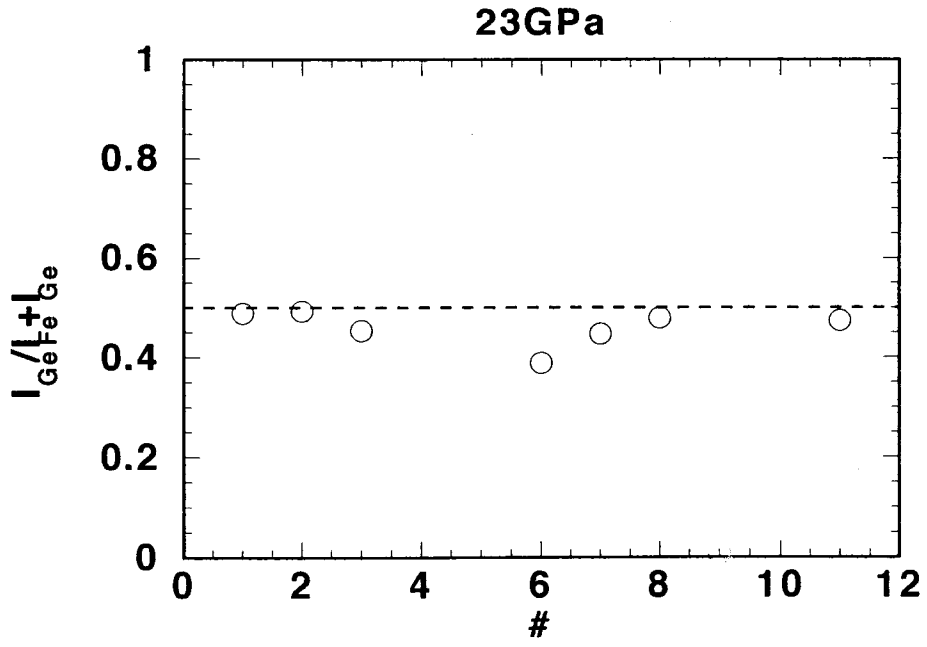

Fig. 4.2.4 Chemical compositions of the recovered sample from 23 GPa.

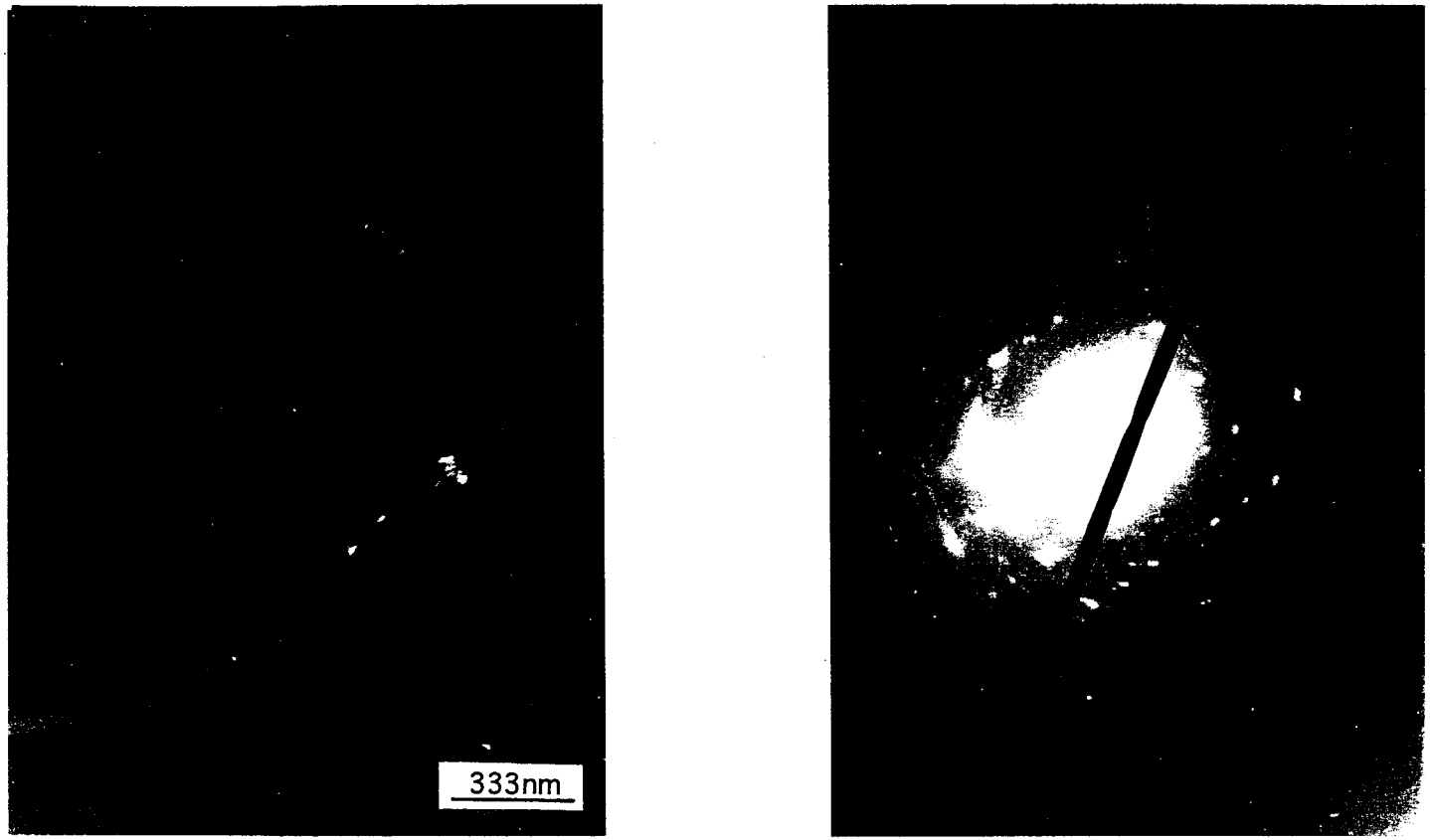

Fig. 4.2.3 A dark-field image and the selected area diffraction image of the recovered sample from 21 GPa.

4.3 Pressure-induced change of the crystal structure

4.3.1 Tetrahedral chain configuration

The changes of the O3-O3-O3, Ge-O-Ge and tilt angle at high pressures are shown in Fig. 4.3.1. The O3-O3-O3 angle and tilt angle are respectively 131.1 ° and 5.8 ° at the ambient pressure. These angles are deviated slightly from their respect values of 120 ° and 0 ° for ideal clinopyroxene. The O3-O3-O3 angle and tilt angle continuously decreases up to their respective values of 129.3 ° and 4.2 ° with increasing pressure. The linear regression analyses show that the relations between these angles and the pressure are expressed by the following relations;

$$< O3 - O3 - O3 = 131.1(3) - 0.155(7)P$$

$$Tilt - angle = 6.1(4) - 0.29(8)P$$

where the estimated standard deviations are written in their parentheses. The tetrahedral chain kinks more severely and approaches the ideal configuration with increasing pressure. The completion of the approach to that of ideal clinopyroxene is not observed within the pressure range of the present study.

The Ge-O-Ge is 120.1 ° at ambient pressure, which is slightly larger than that of ideal clinopyroxene (109.47 °). The Ge-O-Ge angles at high pressures are shown in Fig. 4.3.1. A kink point is observed in the Ge-O-Ge angle versus pressure curve. The Ge-O-Ge angle smoothly decreases up to 117.9 ° with increase pressure up to 4.5 GPa, whereas the decrease ceases at higher pressure. The completion of the approach of Ge-O-Ge angle to the ideal angle of 109.47 ° is not observed. The kink mode appears to be changed at about 4.5 GPa. The linear regression analysis in the each pressure region shows the relation between Ge-O-Ge angle and pressure of

$$< Ge - O - Ge = 120.13(9) - 0.52(9)P \qquad (P < 4.5GPa)$$

$$< Ge - O - Ge = 117.95(2) - 0.010(3)P \qquad (P \geq 4.5GPa)$$

Compression of polyhedra

The normalized volume of the polyhedra, void space and unit cell are plotted in Fig. 4.3.2. The remarkable change of the compression process is observed in the polyhedral volume. Below 4.5 GPa, the $M1O_6$ and $M2O_6$ octahedra are compressed more significantly than tetrahedron. No remarkable compression of the tetrahedron is observed. The volume compressibilities for the polyhedra below 4.5 GPa are β_v [$M1O_6$] = 0.0134(27) GPa^{-1}, β_v [$M2O_6$] = 0.0175(13) GPa^{-1} and β_v [TO_4] = -0.00055(50) GPa^{-1}. The compressional process below 4.5 GPa is common in many pyroxenes (Levien and Prewitt 1981; Zhang et al. 1997).

Above 4.5 GPa, the GeO_4 tetrahedra are significantly compressed. The volume decrease of tetrahedra up to 8.2 GPa is 2.6 $\sigma(V)_{8.2GPa}$, where $\sigma(V)_{8.2GPa}$ is the estimated standard deviation of the tetrahedral volume at 8.2 GPa. The compressibilities for polyhedra are determined as β_v [$M1O_6$] = 0.0042(36) GPa^{-1}, β_v [$M2O_6$] = 0.0021(1) GPa^{-1} and β_v [TO_4] = 0.0066(11) GPa^{-1} between 4.5 GPa and 8.2 GPa. The volume compressibility of the tetrahedron is well consistent with that of $MgGeO_3$ (β_v [GeO_4] = 0.0074 GPa^{-1}) which has been determined by in-situ high-pressure EXAFS (Andrault et al. 1992). It is noticeable that the tetrahedra is as compressible as, or more compressible than the octahedra between 4.5 and 8.2 GPa.

To understand the reason of the change of the compression process at 4.5 GPa, the mean Ge-O bond bonds at high pressure are shown in Fig. 4.3.3. No significant change of mean Ge-O bond length is observed below 4.5 GPa, whereas the Ge-O bond length decrease above 4.5 GPa. The linear regression analysis of the Ge-O length below 4.5 GPa and above 4.5 GPa shows the relation between Ge-O angle and pressure of

$$d(Ge - O) = 1.763(2) + 0.0003(6)P \qquad (P < 4.5GPa)$$

$$d(Ge-O) = 1.783(3) - 0.0042(5)P \qquad (P > 4.5GPa)$$

In summary, the compression behavior changes at 4.5 GPa from the preferential compression of octahedra with decrease of Ge-O-Ge angle, to the homogeneous compression of all the polyhedral with no change in Ge-O-Ge angle

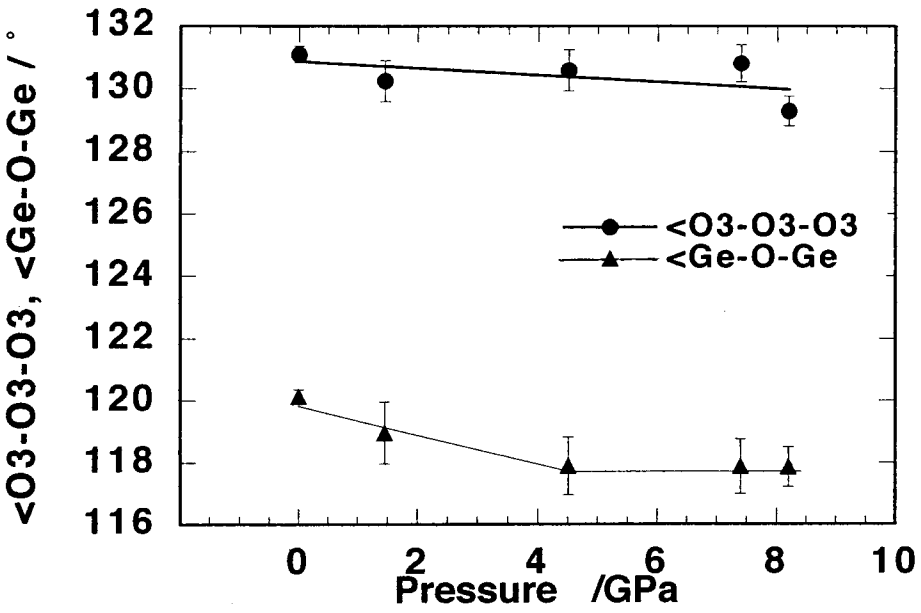

Fig. 4.3.1a O3-O3-O3 and Ge-O-Ge angles of tetrahedral chain at high-pressures.

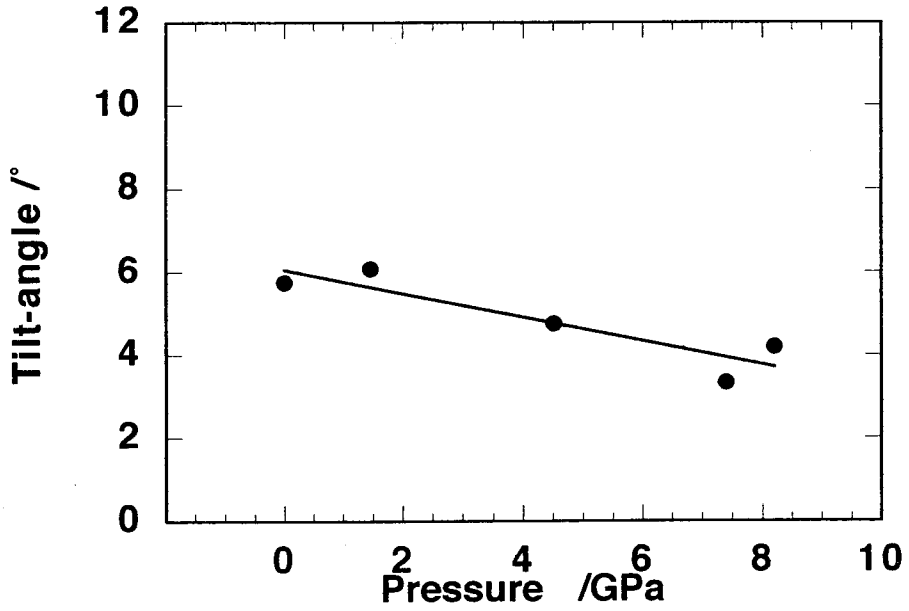

Fig. 4.3.1b Tilt angle of tetrahedral chain at high-pressures.

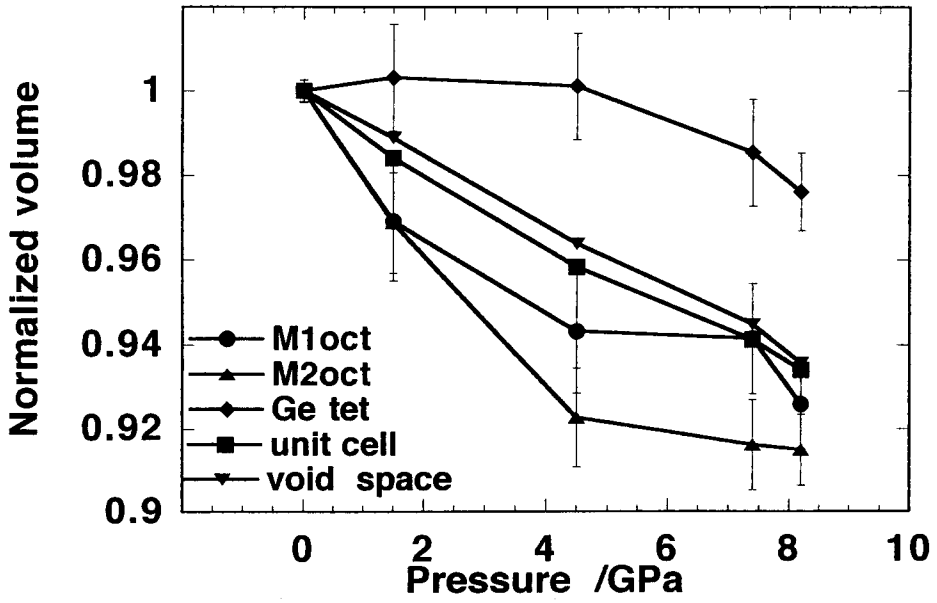

Fig. 4.3.2 Normalized volumes of the polyhedra, void space and unit cell at high pressures

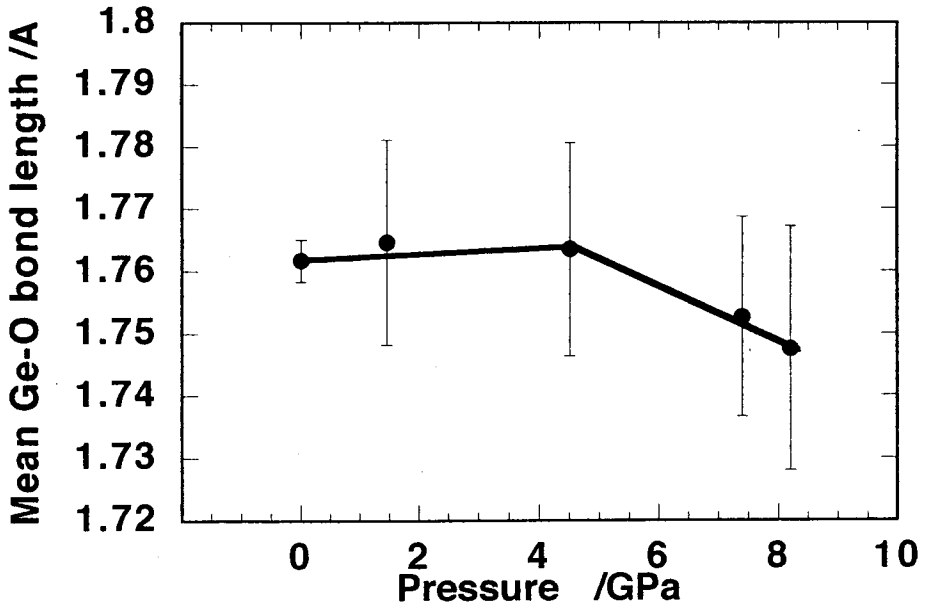

Fig. 4.3.3 Mean Ge-O bond length at high pressures

4.4 Molecular orbital calculation

4.4.1 Previous study

Computational quantum chemistry has been developed to elucidate bond length and angle variation, electron density distributions, reactions and energetics of a small molecules. From the similarity of the bond length and angles of the TOT groups (T = Si, Ge) between small gas molecules and crystalline phases, the method has been employed to generate potential surfaces and deformation maps for a variety of molecules especially designed to understand the chemical bonding in minerals (Gibbs 1982, Tsuneyuki et al 1988, Gibbs et al 1998). Gibbs et al. (1987) calculated the total energy of $H_3GeOGeH_3$ (H_6Ge_2O) cluster, which was the model of the tetrahedral linkage in minerals, as a function of Ge-O bond length and Ge-O-Ge bond angle by the molecular orbital (MO) calculation. The calculated potential energy curve showed a good correspondence with the experimentally observed geometries in real crystals. It supports that the calculation results for the corresponding molecule are applicable to the understanding of the chemical properties of the crystals.

4.4.2 Purpose of this study

The present powder diffraction study showed that the $FeGeO_3$ clinopyroxene change the Ge-O-Ge linkage during the transformation. The single crystal study on $FeGeO_3$ showed unusual compressional behavior above 4.5 GPa in terms of the tetrahedral compressibility and Ge-O-Ge angle. The results suggest that the stability of Ge-O-Ge linkage may affect the high-pressure transformation into $FeGeO_3$ (II). In order to reveal the relationship, it is important to estimate the strain energy of Ge-O-Ge linkage as functions of Ge-O bond length and Ge-O-Ge angle. In the present study, the attention was paid especially to the strain energy of Ge-O-Ge linkage.

Gibbs et al. (1987) has calculated the total energy curve of the H_6Ge_2O molecule around the

potential minimum geometry as a function of Ge-O bond distance and Ge-O-Ge angles. The H_6Ge_2O molecule has the energy potential minimum at the geometry of the Ge-O bond length of 1.756 Å and Ge-O-Ge angle of 133.4 ° and the energy increases with the deviation of the geometry from the energy minimum one. However, these calculation results are insufficient to discuss the stability of the Ge-O-Ge linkage near at the transformation pressure, because the geometry of the Ge-O-Ge linkage near at transformation pressure will be largely deviated from the potential minimum geometry. To discuss the stability of the tetrahedral linkage near at the transformation pressure, it is needed to elucidate the stability of the tetrahedral linkage with the geometry deviated largely from the potential minimum geometry. Therefore, the energy potential surface of germanate cluster is calculated over wide Ge-O bond length and Ge-O-Ge angle in this study.

4.4.2 Experimental

The total energy of the $H_6Ge_2O_7$ (vertex-shared tetrahedra) cluster was calculated as functions of Ge-O bond length and Ge-O-Ge angle by a general *ab initio* quantum chemistry package of General Atomic and Molecular Electronic Structure System (GAMESS) which has been developed by the Gordon research group at Iowa State University. The calculation was performed on personal DOS/V computers.

The calculation was performed by the following procedures. First, the energy minimum configuration of the electrically neutral H_4GeO_4 tetrahedral molecule (Fig. 4.4.1a) was examined to determine the reasonable distance of H-O bond. This procedure was performed by the approach of geometry toward the one with the lower total energy (optimization). In the calculation, an 6-31G** basis set was used for Ge and the geometry of cluster was not constrained symmetrically. The optimized geometry of H_4GeO_4 tetrahedral molecule is shown in Table 4.4.1, together with

those of the previous calculation by Gibbs et al. (1987) and the experimentally determined one (Shannon 1976). The presently determined Ge-O distance and H-O distance are slightly shorter than those of Gibbs (1987) and the experimental determined values. It may be due to the small cluster size used in the calculation or the insufficient basis set for Ge. The total energies of the $H_6Ge_2O_7$ (vertex-shared tetrahedra) were calculated using the calculated H-O distance (*d(H-O)* =0.926 Å).

The total energy of the $H_6Ge_2O_7$ cluster (vertex-shared tetrahedra) was calculated as functions of Ge-O distance and Ge-O-Ge angle. The tetrahedral chain in clinopyroxene was modeled by the linkage of two neutral tetrahedra with sharing one of their vertexes. The cluster was constrained to have the mirror symmetry on the shared oxygen between two tetrahedra (Fig. 4.4.1b). The H atoms were located at the distance of *d(H-O)* =0.926 Å from the oxygen on the opposite side of the center Ge-cation. The 6-31G** basis set was used for Ge. The total energies of the molecules with the geometries of the Ge-O distances from the 1.55 Å to 1.90 Å with interval of 0.5 Å and the Ge-O-Ge angles from 90 ° to 180 ° with the interval of 10° were calculated. The potential surface of $H_6Ge_2O_7$ molecule (vertex-shared tetrahedra) as a functions of Ge-O distance and Ge-O-Ge angle was obtained by contouring the calculated energy points. To know the energy minimum geometry of the $H_6Ge_2O_7$ molecule, the geometry was also optimized by the same way as that of H_4GeO_4 molecule. (An 6-31G** basis set was used for Ge and the geometry of molecule was not constrained symmetrically).

4.4.3 Result

The potential minimum geometry of $H_6Ge_2O_7$ molecule determined in the present study is shown in Table 4.4.2, together with that of previous study (Gibbs et al. 1987) and the experimental values. The experimental values are determined by averaging the Ge-O distances and Ge-O-Ge

angles of the 86 geometries of 39 germanates in Table 4.4.3. The presently determined potential minimum geometry is not close to the experimentally determined geometry, while it is close to the previously calculated value of Gibbs et al. (1987). The reason of the difference might be due to the small cluster size used in the MO calculation or the insufficient basis (6-31G**) for Ge used in the calculations. Especially, the Ge-O bond length of the energy minimum geometry is thought to be very sensitive to the H-O distance because the approach of proton toward oxygen would directly change the electronic charge of oxygen. Therefore, the absolute values of the minimum Ge-O bond length is doubtful, while the relative change of the stability of Ge-O-Ge linkage with the Ge-O bond length would be credible.

The calculated total energies of the $Ge_2O_7H_6$ molecules with the various geometries are shown in Table 4.4.4. The energy contour map is shown in Fig. 4.4.2. The contour is drawn with the energy interval of 0.020 a.u. The potential surface has the steep slope against Ge-O bond length and has the wide slope against Ge-O-Ge angle. In order to show it more clearly , the total energy curves around the potential minimum geometry against Ge-O distance and Ge-O-Ge angle are shown in Fig. 4.4.3. The total energy is almost constant with change of the Ge-O-Ge angle in the range between 120 ° and 180 °, thought it remarkably increases out of this range. While the total energy remarkably and continuously increases with the deviation of Ge-O distance from the energy minimum distance. These results suggest that the GeO_4 tetrahedral linkage becomes unstable remarkably with the departure of the Ge-O length and slightly with the change of Ge-O-Ge angle from the respective values of energy minimum geometry.

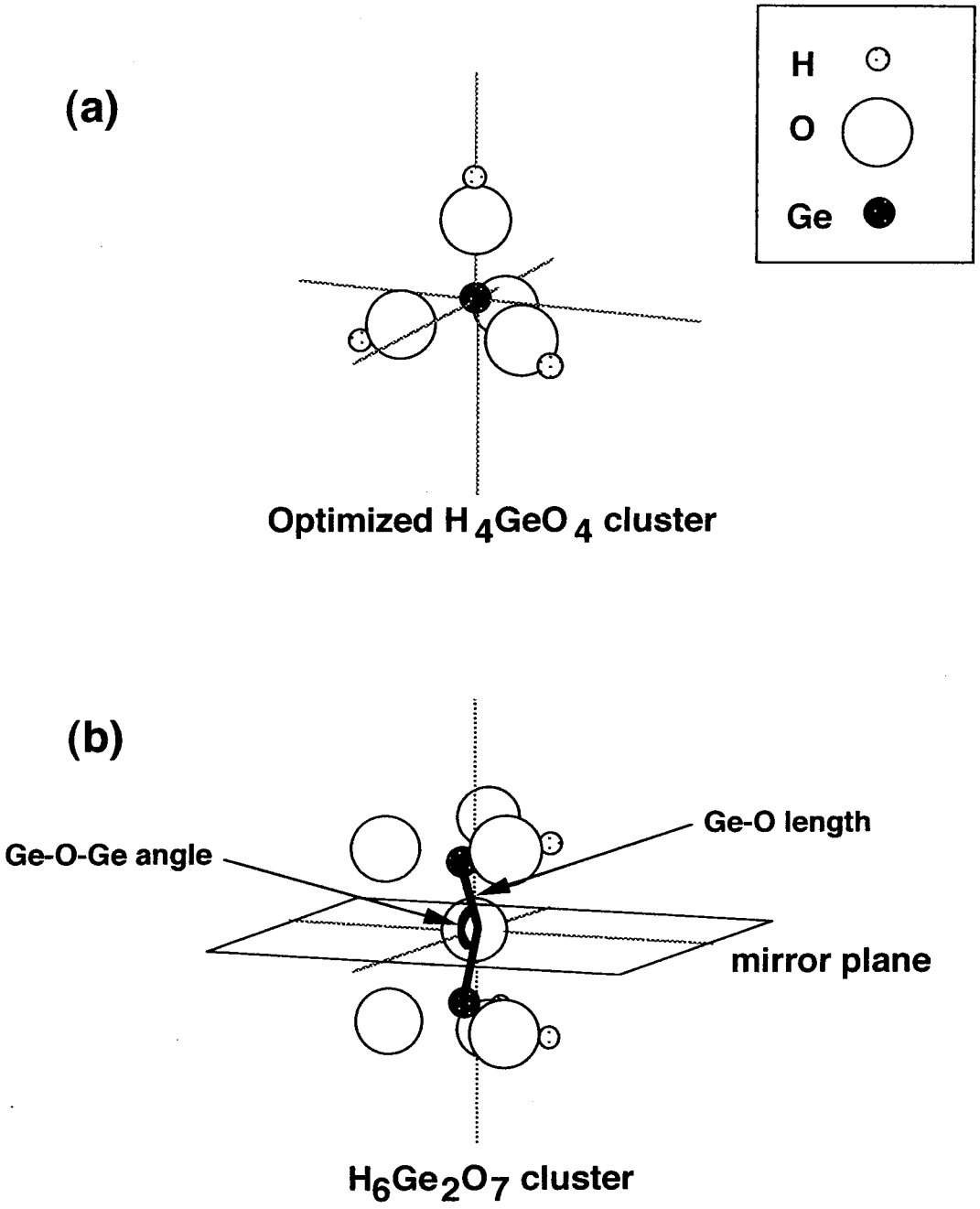

Fig. 4.4.1 (a) Optimized geometry of H_4GeO_4 cluster. (b) $H_6Ge_2O_7$ cluster used in the calculation.

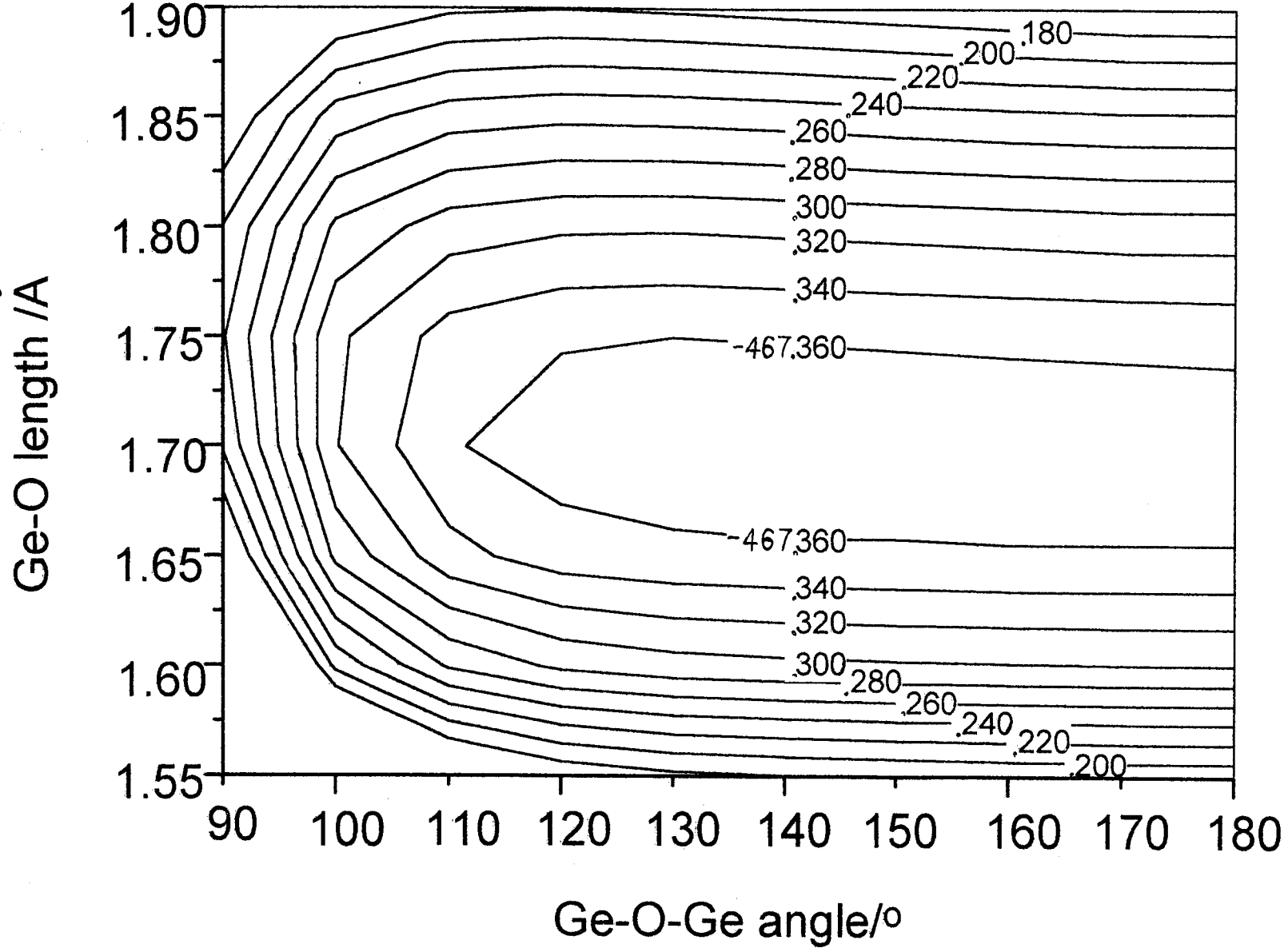

Fig. 4.4.2 Energy contour map of $H_6Ge_2O_7$ as functions of Ge-O bond length and Ge-O-Ge angle.

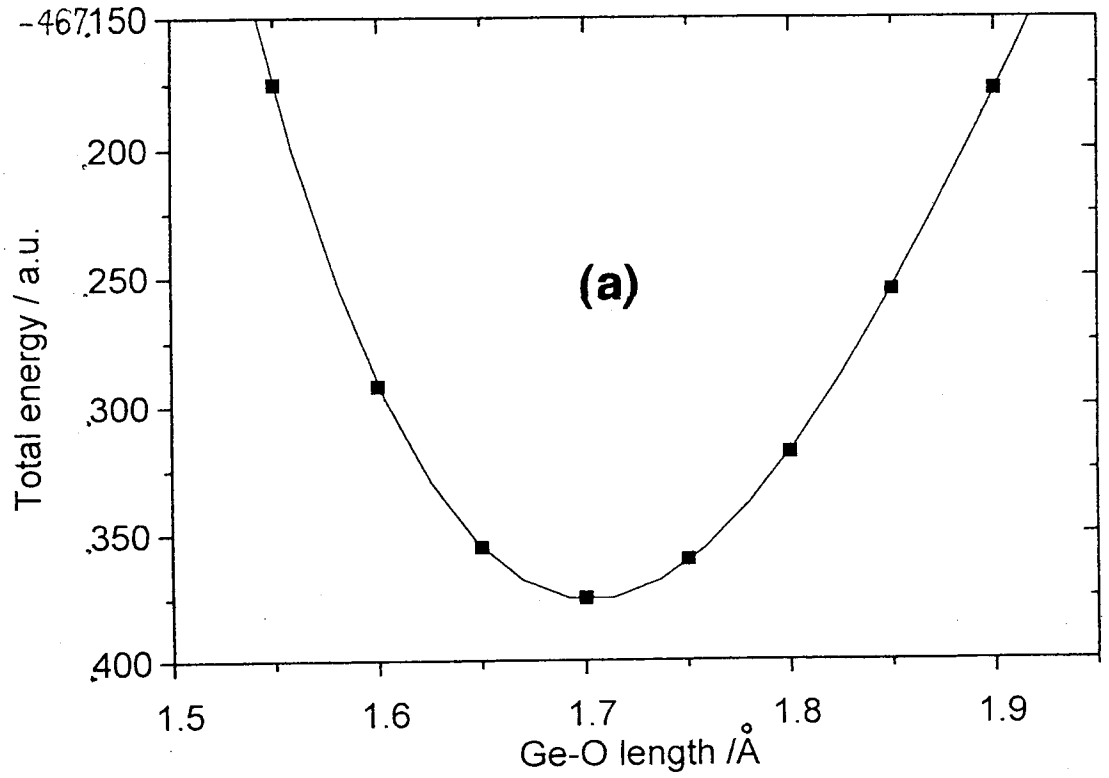

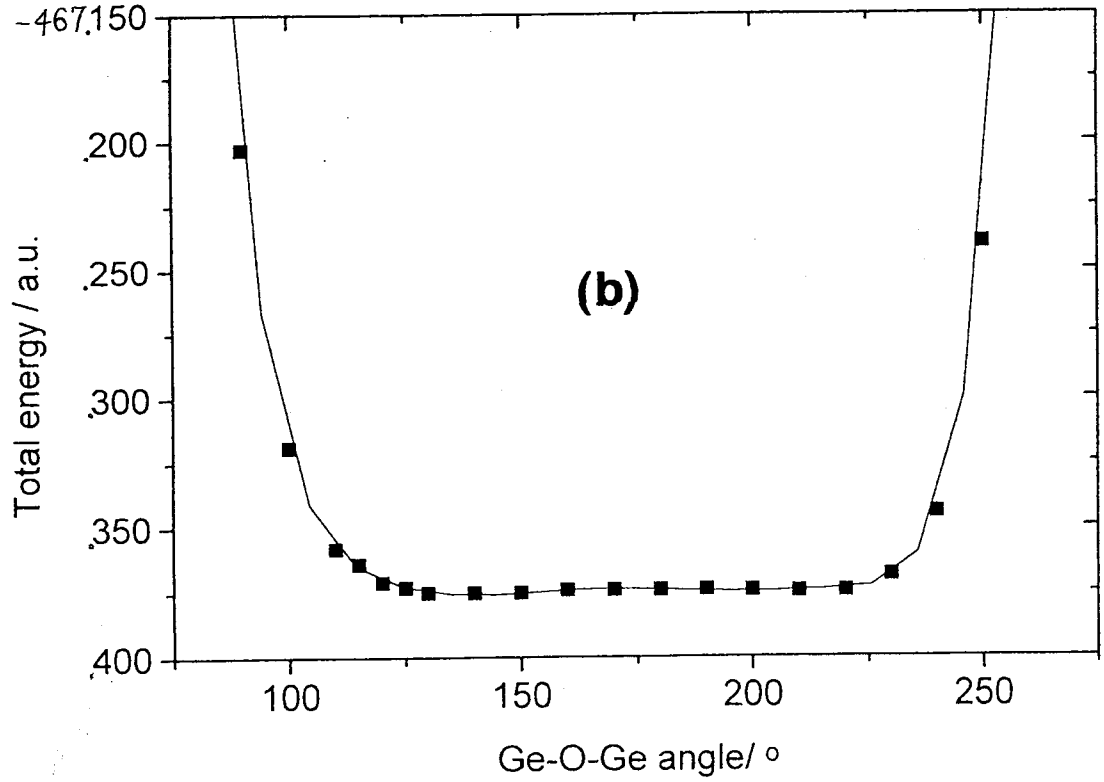

Fig. 4.4.3 Total energy curves around the potential minimum geometry (a) against the Ge-O bond length and (b) against Ge-O-Ge bond angle.

Table 4.4.1 Optimaized geometries of H_4GeO_4 cluster.

	d(Ge-O) /Å	d(H-O)/ Å	*Et* / a.u.
Calculate			
Gibbs (1987) (3-21G*)	1.742	0.965	-2365.80960
This study (6-31G**)	1.693	0.926	-2375.17606
Experimental			
Shannon (1976)	1.74†	0.97†	

†Ionic radii of $r\,(^{IV}Ge^{4+}) = 0.39$ Å, $r\,(^{II}O^{2-}) = 1.35$ Å and $r\,(^{I}H^{+}) = -0.38$ Å are used.

Table 4.4.2 Optimaized geometries of $Ge_2O_7H_6$ and Ge_2OH_6 clusters.

basis set for Ge	d(Ge-O) /Å	d(H-O)/ Å	<Ge-O-Ge	*Et* / a.u.
Calculated				
Gibbs (1987) Ge_2OH_6 (3-21G*)	1.756	0.965	133.4	-4209.4365
This study $Ge_2O_7H_6$ (6-31G**)	1.735	0.943	133.8	-4674.4769
Experimental††				
	1.787	-	126.0	

††The Ge-O distance and Ge-O-Ge angle were the averaged values of those of 86 geometries in 39 gemanates, respectively (Table 4.4.3)

Table 4.4.3 Germanates compounds used in the determination of the experimental values of the Ge-O bond length and Ge-O-Ge angle.

$LaGaGe_2O_7$	Kaminskii et al. (1986)
$Gd_4(Ge_2O_7)(GeO_4)(OH)_2$	Mamin et al. (1987)
$Tb_2Ge_2O_7$	Geller et al. (1987)
$Na_4K_2Ge_2O_7$	Halwax et al. (1987)
$Na_2ZrGe_2O_7$	Ilyushin (1989)
$Li_6Ge_2O_7$	Vollenkle (1980)
$Eu_2Ge_2O_7$	Smolin (1970), Chiragov et al. (1983)
$CaCuGe_2O_6$	Berruzi et al. (1986)
$KInGe_2O_6$	Genkina et al. (1988)
$K_2ZnGe_2O_6$	Grins et al. (1989)
$K_4SrGe_3O_9$	Baumgartner et al. (1977)
$Ca_{1.15}Na_{3.70}Ge_3O_9$	Nishi et al. (1988)
Na_2GeO_3	Cruickshank et al. (1978)
Li_2GeO_3	Vollenkle (1981)
α-$SrGeO_3$	Nadezhina et al. (1981)
$NaKGeO_3$	Halwax et al. (1984)
$SrGeO_3$	Nadezhina et al. (1981), Hilmer (1962)
$Ca_{1.75}Na_{2.50}Ge_3O_9$	Nishi et al. (1991)
$Ca_{1.5}Na_3Ge_3O_9$	Nishi et al. (1990)
β-$SrGeO_3$	Nadezhina et al. (1981)
K_2GeO_3	Halwax et al. (1984)
$Pb_{2/3}Sr_{1/3}Ge_4O_9$	Venevtsev et al. (1982)
$Li_2Ge(GeO3)_2(OH)_2$	Nevskii et al. (1978)
$K_2Ba(Ge_4O_9)_2$	Baumgartner et al. (1978)
$BaGe_4O_9$	Venevtsev et al. (1982)
$PbGe_4O_9$	Venevtsev et al. (1982)
GeO_2 (Cristbalite)	Okuno et al. (1986)
GeO_2 (Low-quartz)	Smith and Isaacs (1964), Okuno et al. (1986)
$La_4(Ge_3O_{10})(GeO_6)$	Vetter et al. (1988)
$MnGeO_3$	Fang et al 1969
$BaGeO_3$	Hilmer (1962)
$Na_4Ge_9O_{20}$	Ingri and Lundgren (1963)
$Na_8Sn_4Ge_{10}O_{30}(OH)_4$	Larsen et al. (1967)
β-Mn_2GeO_4	Morimoto et al. (1972)
$CoGeO_3$	Peaor (1968)
$K_2Ge_4O_9$	Vollenkle and Wittemann (1969)
Na_2GeO_3	Vollenkle (1971)
$MgGeO_3$ (cpx) (20, 210, 420, 620, 750°C)	Yamanaka et al (1985)
$MgGeO_3$(opx) (20, 950°C)	Yamanaka et al (1985)
q-GeO_2 (10^{-4}, 4.0, 7.2, 10.2 GPa)	Glinnemann et al (1992)

Table 4.4.4 Total energies of the $Ge_2O_7H_6$ molecules with various Ge-Obond lengths (Å) and Ge-O-Ge angles (°).

d(Ge-O)	<Ge-O-Ge	E_T(a.u.)
1.55	90	-4673.8764
1.60	90	-4674.0439
1.65	90	-4674.1486
1.70	90	-4674.2032
1.75	90	-4674.2179
1.80	90	-4674.2012
1.85	90	-4674.1599
1.90	90	-4674.0999
1.55	100	-4674.0685
1.60	100	-4674.2059
1.65	100	-4674.2854
1.70	100	-4674.3189
1.75	100	-4674.3159
1.80	100	-4674.2842
1.85	100	-4674.2301
1.90	100	-4674.1592
1.55	110	-4674.1373
1.60	110	-4674.2629
1.65	110	-4674.3327
1.70	110	-4674.3580
1.75	110	-4674.3480
1.80	110	-4674.3103
1.85	110	-4674.2512
1.90	110	-4674.1760
1.55	120	-4674.1643
1.60	120	-4674.2844
1.65	120	-4674.3496
1.70	120	-4674.3711
1.75	120	-4674.3578
1.80	120	-4674.3173
1.85	120	-4674.2559
1.90	120	-4674.1788
1.55	130	-4674.1749
1.60	130	-4674.2922
1.65	130	-4674.3551
1.70	130	-4674.3746
1.75	130	-4674.3597
1.80	130	-4674.3179
1.85	130	-4674.2553
1.90	130	-4674.1770

d(Ge-O)	<Ge-O-Ge	E_T(a.u.)
1.55	140	-4674.1792
1.60	140	-4674.2950
1.65	140	-4674.3566
1.70	140	-4674.3751
1.75	140	-4674.3592
1.80	140	-4674.3164
1.85	140	-4674.2527
1.90	140	-4674.1734
1.55	150	-4674.1816
1.60	150	-4674.2965
1.65	150	-4674.3522
1.70	150	-4674.3747
1.75	150	-4674.3579
1.80	150	-4674.3142
1.85	150	-4674.2495
1.90	150	-4674.1692
1.55	160	-4674.1836
1.60	160	-4674.2977
1.65	160	-4674.3576
1.70	160	-4674.3743
1.75	160	-4674.3566
1.80	160	-4674.3120
1.85	160	-4674.2464
1.90	160	-4674.1652
1.55	170	-4674.1852
1.60	170	-4674.2985
1.65	170	-4674.3578
1.70	170	-4674.3739
1.75	170	-4674.3556
1.80	170	-4674.3104
1.85	170	-4674.2443
1.90	170	-4674.1625
1.55	180	-4674.1858
1.60	180	-4674.2989
1.65	180	-4674.3579
1.70	180	-4674.3737
1.75	180	-4674.3553
1.80	180	-4674.3098
1.85	180	-4674.2435
1.90	180	-4674.1615

5. Discussion

5.1 Transformation process under room-temperature condition

5.1.1 Inhibition of decomposition process

$FeGeO_3$ clinopyroxene is known to decompose into the mixture of Fe_2GeO_4 spinel and GeO_2 rutile at 1 GPa and at 700 °C (Ringwood and Seabrook 1963). In the present study, in-situ X-ray diffraction study showed the transformation into another phase, instead of the decomposition. The nuclei of the decomposed phases could not be detected within the spatial resolution of TEM and no remarkable change of the chemical composition was detected by ATEM. These results strongly suggest that the decomposition was inhibited under room-temperature condition. The clinopyroxene reversibly transformed into $FeGeO_3$ (II) in the present study. To examine whether the presently observed transformation into $FeGeO_3$ (II) is accompanied by atomic diffusion process, the transformation rate at room temperature of the transition involving the atomic diffusion process was estimated from the kinetic study of the high-pressure transformation of GeO_2.

GeO_2 is known to transform from quartz-type to rutile-type with the atomic diffusion process under high-pressure and high-temperature conditions. The transformation kinetics of GeO_2 have been investigated by several authors (Zeto and Roy 1969, Brar and Schloessin 1981, Yamanaka et al 1992). In this discussion, the results of Zeto and Roy (1969) are used. By the exploration of the regression line of rate constant toward room temperature, the kinetic time required for the transformation of the volume fraction of 15 % is calculated as 1.05×10^{13} sec. (3.3×10^5 year) at 300 K. This value is so small that the transformation involving atomic diffusion would not occur under room temperature condition. This suggests that the transformation from clinopyroxene into $FeGeO_3$(II) was accompanied by a diffusionless process.

5.1.2 Martensite transformation

Christian classified the transformations on the basis of the transformation mechanism (Fig. 5.1). The presently observed transformation had the characters of "all phases have same composition", "athermal" and " semi-coherent". Based on these characters, the transformation is thought to be classified into "martensite".

Martensite transformations generally have the following characters (Rao and Rao, 1978),

(i) Transformation is from single phase to single phase

(ii) All phases have the same composition on transformation. Transformation is accompanied by the cooperative movements of the atoms and is diffusionless.

(iii) The surface roughening is observed in the transformed phase.

(iv) Crystallographic relations are observed between the parent and transformed phases. The martensite is formed on the habit plane.

(v) A lot of lattice defects was observed in the martensite.

In the transformation between clinopyroxene and $FeGeO_3$(II), the following characters were observed:

(i) Both phases of clinopyroxene and $FeGeO_3$ (II) were single phase.

(ii) The chemical compositions of both phases were invalid during the transformation. The atomic movements on the transformation would be cooperative, as is mentioned later.

(iii) The surface roughening of the transformed phase could not be confirmed because of the difficulty in the observation of the surface of the tiny powder sample in DAC.

(vi) The orientation between the parent and transformed phases could not be identified by the powder X-ray diffraction.

(v) The existence of the lattice defects was inferred from the distortion of the diffraction spots of

recovered sample in TEM observation.

These characters of the presently observed transformation were well consistent with those of the martensite. It suggests that the presently observed transformation is martensite transformation, although some characters have not been confirmed yet .

The nucleation of martensite is generally induced by the strain in the parent phase, rather than by the thermal activated process. Therefore, the parent phase can be transformed without large thermal energy (Athemal transformation). The transformation rate is generally very large even at room temperature, because the transformation does not involve the atomic diffusion. For example, one fragment of martensite of Fe-Ni-C alloy completes the nucleation within 10^{-7} sec and the growth rate is within 10^{5}cm/sec (Bunshah Mehl 1953). In the present study, the clinopyroxene would be transformed into $FeGeO_3$ (II) even at room temperature by martensite mechanism.

5.1.3 Transformation mechanism

Atomic movements during the transformation

In this section, the atomic movements during the martensite transformation are discussed on the basis of the crystal structures of the clinopyroxene and $FeGeO_3$(II). The crystal structures of the clinopyroxene and $FeGeO_3$ (II) are shown in Fig. 4.1.6. Main structural difference between two phases is the oxygen arrangement: the clinopyroxene has *CCP* and the $FeGeO_3$ (II) has the deformed *HCP*. No remarkable difference is observed in their cation arrangements of Fe^{2+} and Ge^{4+}. The transformation between these phases is possible by the change of the stacking sequence of the oxygen layers. The displacements of the second and fourth oxygen layers of $\Delta \boldsymbol{d}$ = (0, +Δ, +1/√3r) change the oxygen arrangement from *CCP* of clinopyroxene to the deformed *HCP* of the $FeGeO_3$ (II). The movements are shown in Fig. 5.2. This displacement of the oxygen packing plane is reasonable in terms of the deformation of the crystal because the slip on (100) is easiest

among the other planes in clinopyroxene structures (Kolle and Blacic 1982) and because it does not involve the breaking of the tetrahedral chain. In this process, two slip directions toward $+b$- and $-b$ of clinopyroxene are possible (Fig. 5.3). When the oxygen plane slipped toward both directions randomly, the periodicity of (010) plane (based on a_{hp}, b_{hp}, c_{hp} axes) in $FeGeO_3$ (II) phase will be reduced. This would cause the decrease in the diffraction intensity of *0k0* of $FeGeO_3$ (II) compared to that of simulated pattern.

The displacements of the second and fourth oxygen layers increase the coordination number of Ge^{4+} without the atomic diffusion, as is shown in Fig. 5.2. By this way, the coordination of Ge^{4+} cation is considered to increase from fourfold to six-fold during the transformation.

Crystallographic orientation and coherency on habit plane

When the transformation is performed by the above mechanism, the following crystallographic orientations would be observed between the clinopyroxene and $FeGeO_3$ (II) phases:

$a_{cpx} \wedge a' = 10.34°$

$b_{cpx} // b'$

$c_{cpx} // c'$

where a_{cpx}, b_{cpx} and c_{cpx} are the cell axes of the clinopyroxene and a' , b' and c' are those of $FeGeO_3$ (II). The habit plane is the (100) of clinopyroxene. The coherency of both phases are calculated from their lattice parameters at 20.1 GPa, where the lattice parameters of clinopyroxene at 20.1 GPa are determined by extrapolating their compression curves. The coherency are calculated as:

$$\delta_a = \frac{a_{cpx} - a'}{a_{cpx}} = 1.1\%$$

$$\delta_b = \frac{b_{cpx} - b'}{b_{cpx}} = 2.1\%$$

$$\delta_c = \frac{c_{cpx} - c'}{c_{cpx}} = 1.4\%$$

The interface of both phase are coherent and, therefore, both phases can easily transform smoothly each other.

5.1.4 Effects of the pressure and stress on the martensite transformation

It is well-known that the martensite transformation is affected by the stress field. For example, the martensite transformations of carbon steel and Fe-30~33%Ni alloy is enhanced by stress field due to the formation of a initial martensite nucleus (auto-catalytic effects). In some case, the martensite transformation occurs even above M_s point (and below M_d points) by application of the stress or by plastic working. As the most extreme case, the ß-brass and In-Tl alloys form the martensite reversibly only by the application of external stress.

In the present study, the transformation was induced by application of pressure (or stress). The nucleation process of martensite is explained as follows. As shown in chapter 4.1, the clinopyroxene was metastably compressed and changed the atomic arrangements with pressure. In this process, the Ge-O bond length and Ge-O-Ge angle decreased with pressure. As discussed in the next section, these changes increase the local energy of tetrahedral chain. This pressure-induced increase of the strain energy of tetrahedral chain would give the strain sufficient for the formation of the nucleus of the martensite. Actually, the martensite transformation was performed by changing the geometry of tetrahedral chain. These suggests that the pressure contributes to increase the strain energy of the local unit and this pressure-induced strain helps the nucleation of the martensite.

5.1.5 Difference of the transformation process

In the present study, the transformation by diffusionless mechanism was clearly found. From the present results, at least two mechanisms play the main role in determining the transformation process. One is diffusion mechanism and the other is strain-induced (diffusionless) mechanism.

Each mechanism has the following characters.

(i) Diffusion mechanism

If the transformation is accompanied by the diffusion mechanism, the parent phase changes the crystal structure completely and is transformed into lowest free energy phase. This process needs large activation energy, so the diffusion mechanism is scarcely observed at room temperature.

(ii) Strain-induced (diffusionless) mechanism

The transformation is accompanied by the short-range atomic movements and the parent phase transforms into the lower energy phase. The diffusionless mechanism is accompanied by the small activation energy, therefore, this mechanism is often observed under low temperature condition.

It depends on the temperature which mechanism controls the transformation process. The difference of the transformation process of minerals between at high-temperature and room temperature (Fig 1.1 and Fig 1.2) would originated in the difference of the transformation mechanisms. The metastable phase, that were formed by the room temperature compression, would be accompanied by the diffusionless mechanism, while most transformations at high temperature in Fig. 1.1 are accompanied by diffusion mechanism.

5.2 Pressure-induced instability of clinopyroxene

5.2.1 Instability of tetrahedral chain in clinopyroxene

The 86 geometries in 39 germanates observed in real crystals are shown in Fig. 5.4 as functions of Ge-O bond length and Ge-O-Ge angle, where the averaged geometry is shown by the symbol "X". Many geometries of tetrahedral linkage distribute around the averaged geometry. The distribution decreases with the deviations of the Ge-O distance and Ge-O-Ge angle from the averaged values. It is noticeable that only a few geometry is observed in the region out of the

dotted curve.

MO calculation showed that the total energy of vertex-shared tetrahedra increases with the deviation of Ge-O bond length and Ge-O-Ge angle from the potential minimum geometry as mentioned in Chapter 4.4. To know the correlation between the calculated energy surface and the distribution of geometry of the real crystal, the calculated potential surface is imposed on the Fig. 5.4, where it was imposed so that the potential minimum Ge-O distance coincides with the averaged Ge-O distance of real crystals because the absolute value of the energy minimum Ge-O distance of MO calculation have the large uncertainty. The good correlation was observed between the potential surface and the distribution of the tetrahedral geometries in real crystals. It suggests that the stability of the crystal are strongly related to local stability of tetrahedral linkage.

The presently observed change of tetrahedral geometry in $FeGeO_3$ clinopyroxene at high pressures is shown by solid circles in Fig. 5.4. The Ge-O-Ge angle decreased with increasing pressure up to 4.5 GPa. The calculated potential surface suggests that the local energy of tetrahedral chain increases with pressure. The Ge-O-Ge angle stopped decreasing at 4.5 GPa where the angle approached at 117.8 °. This may be related to the steep potential surface below about 120 °. At higher pressure, the Ge-O is observed to start decreasing with pressure. It would contribute to the increase of the local energy of the tetrahedral chain, as is shown by the potential surface. The local instability of the tetrahedral chain would induce the transformation of the clinopyroxene under high-pressure condition.

5.2.2 Comparison with other germanates

Above results suggest that the transformation from the metastable into high-pressure phase is induced by the instability of tetrahedral linkage under high-pressure condition. In order to check

the validity of this concept, it is applied to the previously reported transformations of the germanates involving the tetrahedral linkage. Furthermore, the critical geometries at the transformation pressure are also investigated to know the stability limit of tetrahedral linkages.

$FeGeO_3$ clinopyroxene (this study)

The critical geometry at the transformation pressure can be estimated from the extrapolation of the pressure-induced change of Ge-O distance and Ge-O-Ge angle toward the transformation pressure. The Ge-O distance and Ge-O-Ge angles at the transformation pressure of 13 GPa are calculated as *d(Ge-O)* = 1.728(20) Å and <*Ge-O-Ge* = 117.8(10) °. The geometry is shown by the symbol "F" in Fig. 5.4.

q-GeO_2

GeO_2 quartz (q-GeO_2) is reported to transform into amorphous state at about 6.5 GPa (Yamanaka et al. 1992). The detailed single-crystal structure analysis of q-GeO_2 was performed up to 5.8 GPa by Glinnemann et al. (1992). The change of the Ge-O distance and Ge-O-Ge angle with pressure is shown in Fig. 5.4. It is found that the local energy of the tetrahedral linkage increase with increasing the pressure. The regression analysis of the Ge-O distances and Ge-O-Ge angles at high pressures suggests that the tetrahedral geometry at transformation pressure is*d(Ge-O)* = 1.732(5) Å and <*Ge-O-Ge* = 123.0 (3). These are shown by the symbol "Q" in Fig. 5.4.

a-GeO_2

GeO_2 glass (a-GeO_2) is formed by the quench of the molten GeO_2 to ambient temperature. The a-GeO_2 is known to be construed by the vertex shearing tetrahedra. The Ge-O distances in a-GeO_2 distribute in the narrow range, while the Ge-O-Ge angles have the variation in some extent (Lapeyre et al. 1983). The high-pressure EXAFS study of a-GeO_2 revealed that the a-GeO_2 transformed into high-pressure state by the coordination increase of Ge^{4+} at 6.6 GPa (Itie

et al. 1992). The pressure-induced change of the Ge-O distances are shown in Fig. 5.5. The Ge-O distance decrease with increasing the pressure up to 6.6 GPa. This process increase the local energy of the tetrahedral linkage. The critical Ge-O distance seems to be *d(Ge-O)* = 1.73 ~ 1.77 Å. The change of the Ge-O-Ge angles at high-pressures cannot be known.

$MgGeO_3$ clinopyroxene (*C2/c*)

$MgGeO_3$ clinopyroxene (*C2/c*) has the same structure as $FeGeO_3$ clinopyroxene. The tetrahedral chain is more severely kinked than that of $FeGeO_3$ at ambient pressure (<O3-O3-O3 = 129.03 °) . X-ray diffraction and EXAFS studies showed the clinopyroxene transforms into high-pressure phase from 8.7 to 30 GPa, as mentioned in the Chapter 2.3. The change of Ge-O distance is shown in Fig. 5.5. The decrease of the Ge-O distance is expected to increase the local energy of the tetrahedral linkage, where the change of the Ge-O-Ge angle is unknown. The energy increase would induce the above mentioned high-pressure transformation. The Ge-O distance at the transition pressure of 8.5 GPa is about *d(Ge-O)* = 1.725 Å. It is noticeable that this value is same as that of $FeGeO_3$, *d(Ge-O)* = 1.728(20) Å within the experimental error. It is found that the transition pressure is sensitive to the geometry of the tetrahedral chain.

$CaGeO_3$ wollastonite

$CaGeO_3$ has a wollastonite structure at ambient pressure (Liebau 1960). The structure is composed of the one-dimensional tetrahedral chain with repeating the three tetrahedra. The high-pressure X-ray diffraction study of $CaGeO_3$ showed that the wollastonite transform into the high-pressure phase at about 6 GPa (Nagai et al. 1985). The high-pressure EXAFS study also showed the coordination increase of Ge^{4+} at about 7 GPa (Andrault et al. 1992). The pressure-induced change of the Ge-O distances of $CaGeO_3$ determined by the EXAFS are shown in Fig.5.5. The decrease of the Ge-O distance is observed with increasing pressure, which would

contribute to the local instability of tetrahedral chain. The Ge-O distance is about *d(Ge-O)* = c.a. 1.75 Å at the transition pressure.

The geometry of the tetrahedral linkage shifts toward those with the high local energy. The values of Ge-O distances at transformation pressures have the similar values of *d(Ge-O)* = 1.72 ~ 1.75 Å among the above compounds. It suggests that the transformation of these germanates occurs when the geometry of the tetrahedral linkage approaches the geometrical limit which is defined by the local energy of the tetrahedral linkage. The onset of the transformation of the metastably compressed phases at low temperature would be controlled by the stability of the local unit in their structure, rather than the thermodynamic stability.

5.3 Effects of the crystal structure on the transformation process

As observed in the present study, the transformation is accompanied by the short-range movements of the atoms under low temperature where the atomic diffusion is suppressed. Under such condition, it is expected that the transformation processes are strongly related to the atomic arrangements in the parent phases. Based on this concept, the transformation processes of germanates compounds induced by the room temperature pressurization are discussed.

The transformation processes of several germanates under high-pressure and room-temperature conditions are already shown in Fig. 1.2. Among these transformations, chain germanates of $CaGeO_3$ pyroxenoid and $MgGeO_3$ and $FeGeO_3$ pyroxenes transform into high-pressure crystalline state with coordination increase of Ge^{4+} cation (Nagai et al 1995). On the other hand, a framework germanate of GeO_2 quartz and a orthogermanates of Mg_2GeO_4 olivine are also known to transform into high-pressure amorphous state with the same coordination increase of Ge^{4+} (Wolf et al 1992, Yamanaka et al. 1992, Mardon et al. 1991). The crystal structures of these phases are summarized as follows.

Comparison of the crystal structures

(i) Chain gemanates

The crystal structures of pyroxene and pyroxenoid are shown along the direction parallel to the oxygen stacking plane in Fig. 5.6. All these structures are based on the deformed *CCP* of oxygen. It is noticeable that the cations of Ge^{4+} or A^{2+} (A = Ca^{2+}, Mg^{2+}, Fe^{2+}) occupies the interstices between the oxygen stacking layers alternately along the stacking direction. Each interstices between the layers is occupied by either Ge^{4+} or A^{2+} cations.

(ii) Germantes with isolated tetrahedra and framework germanates

The crystal structure of Mg_2GeO_4 olivine is shown along the direction parallel to the oxygen stacking plane in Fig. 5.7. The olivine structure of Mg_2GeO_4 is based on the *HCP* of oxygen. Each interstices between the oxygen stacking layers is occupied by the both cations of Mg^{2+} and Ge^{4+} in the ratio of 1: 2, which is remarkably different from that of chain germanate.

The crystal structure of α-quartz is shown in Fig. 5.8 along the c-axis. Quartz structure is composed of the three-dimensional linkage of tetrahedra and can not be described on the basis of closet packing of oxygen.

Comparison of the transformation mechanism on the basis of crystal structure

Under room temperature condition, the shear of the oxygen stacking planes is effective way for the increase of coordination number of the Ge^{4+} cation in the germanate compounds based on the oxygen closest packing. When the oxygen layers were sheared by pressure or shear stress, the tetrahedral sites transform into octahedral sites and vice versa. In the clinopyroxene and pyroxenoid structures, the shear of the oxygen layers above and below the Ge^{4+} cations can smoothly increase only the coordination number of Ge^{4+} in tetrahedral sites with keeping coordination number of Fe^{2+}, which effectively decrease the cell volume. In this process, the

lattice of the parent phase is preserved through the transformation by the cooperative atomic movements.

On the other hands, the coordination increase by shearing the closest packing layers of oxygens is impossible in the olivine structure, because the shear induces both the increase the coordination number of the Ge^{4+} cations and the decrease of coordination number of the A^{2+} cations in the common interstices between the oxygen layers. This process is not preferable in terms of the volume reduction on the phase transformation. Therefore, the coordination increase of Ge^{4+} may be performed by the local change of the atomic position, rather than by the cooperative movement of the atoms. In such case, the translational symmetry of the parent phase may be almost broken and the high-pressure phase can not have the enough large crystalline size to give the measurable X-ray diffraction intensity. The similar situation would occur in the α -quartz which does not have the shear plane appropriate for the coordination increase of Ge^{4+} cation. The coordination number of Ge^{4+} would be increased by the orientationally random movements of atoms, rather than the cooperative movements. In such processes, the olivine and α -quartz GeO_2 transformed into amorphous state by room temperature compression. It is concluded that the transformation processes of the compounds with the tetrahedra, which increase the coordination number at high pressure, depend on the arrangement of the Ge^{4+} cations in their crystal structures. If the coordination increase by the cooperative movements of the atoms are possible during the high-pressure transformation in a given crystal structure, the parent crystalline phase can directly transform into the high-pressure crystalline state. On the other hand, it is not possible in a crystal structure, the parent phase transforms into the amorphous state by the orientationally random movement of the atoms.

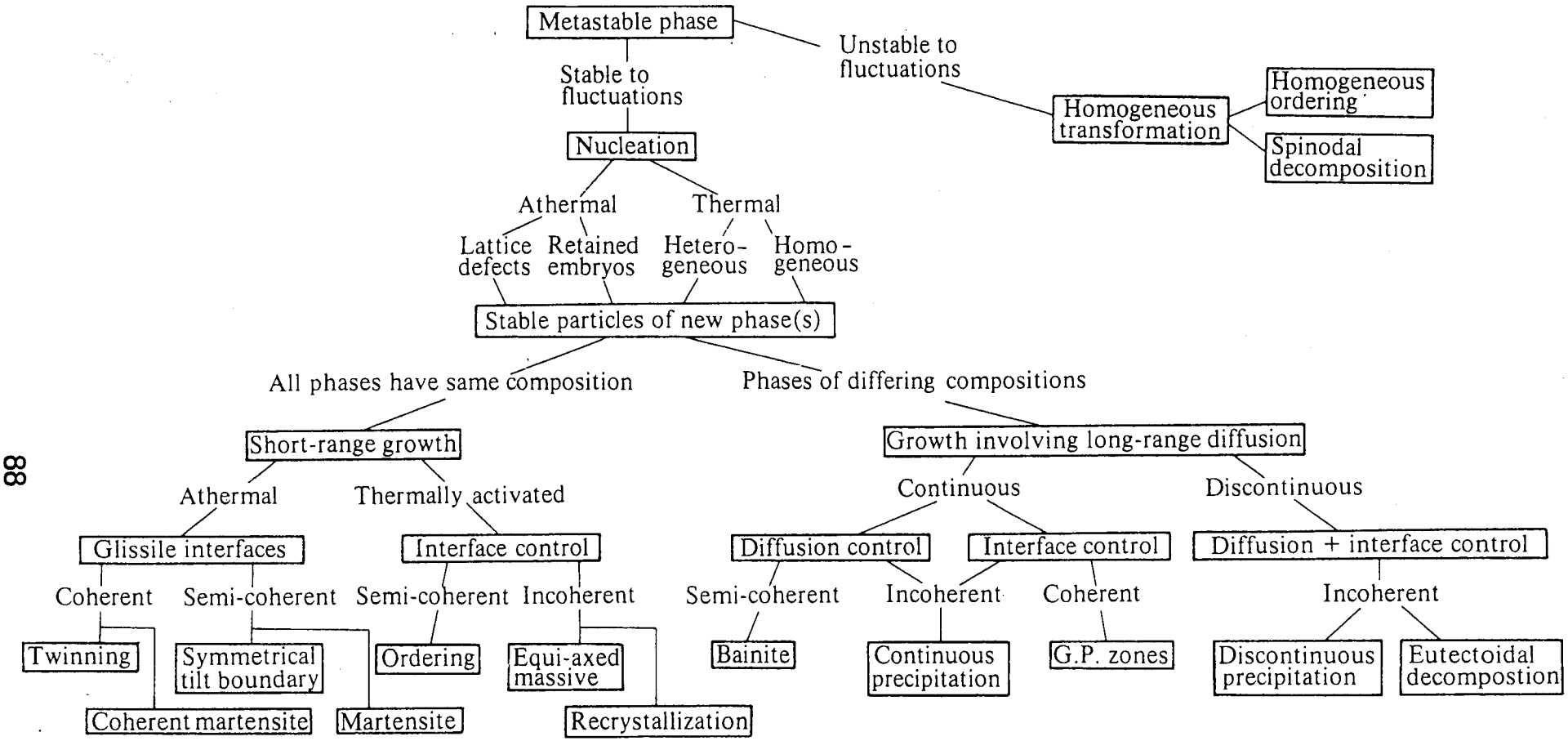

Fig. 5.1 Relations between various transformations in metal systems (Christian 1965)

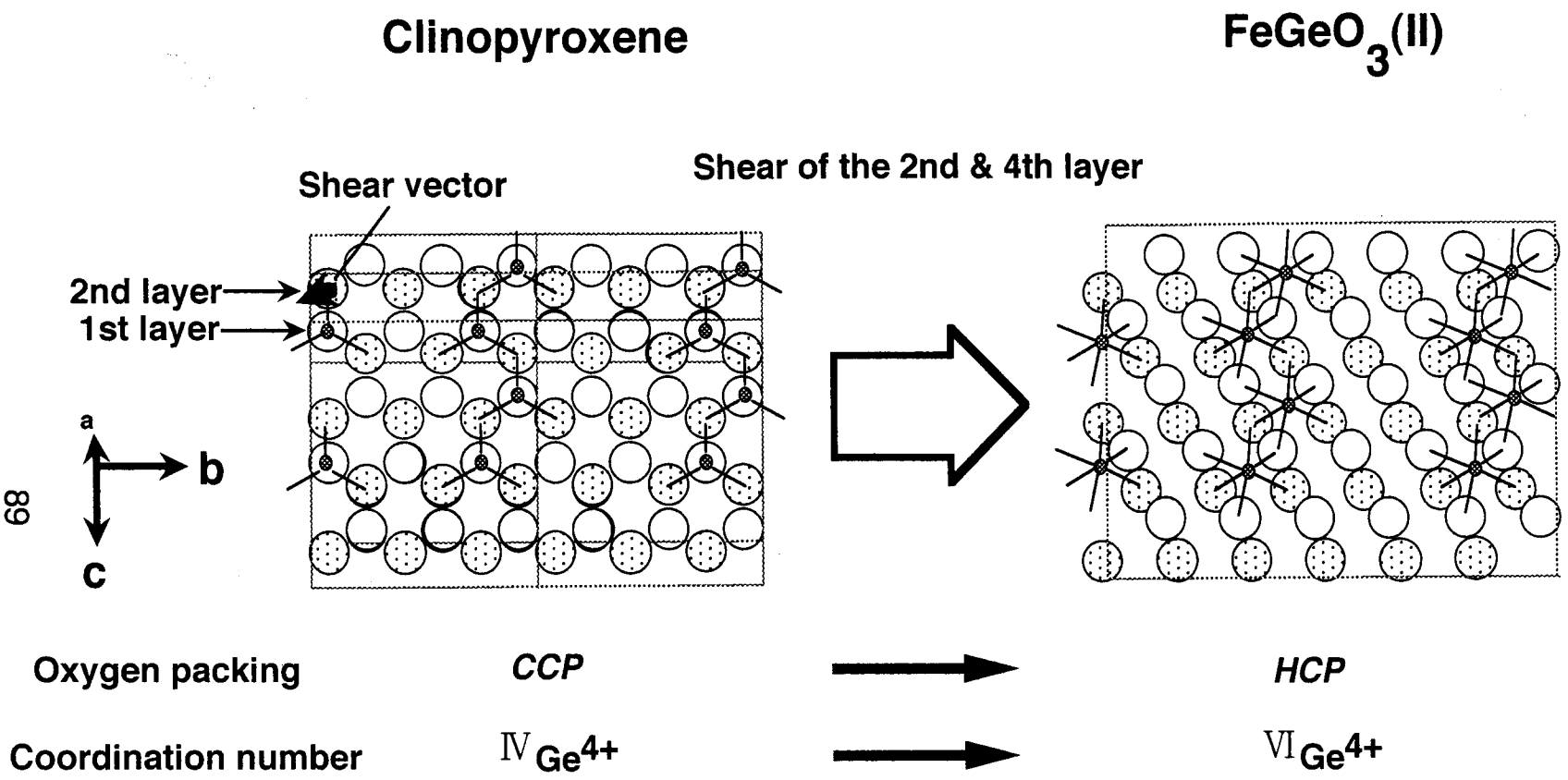

Fig. 5.2 Atomic movements during the transformation. First and second oxygen layers of clinopyroxene and $FeGeO_3$ (II) are shown along a* direction.

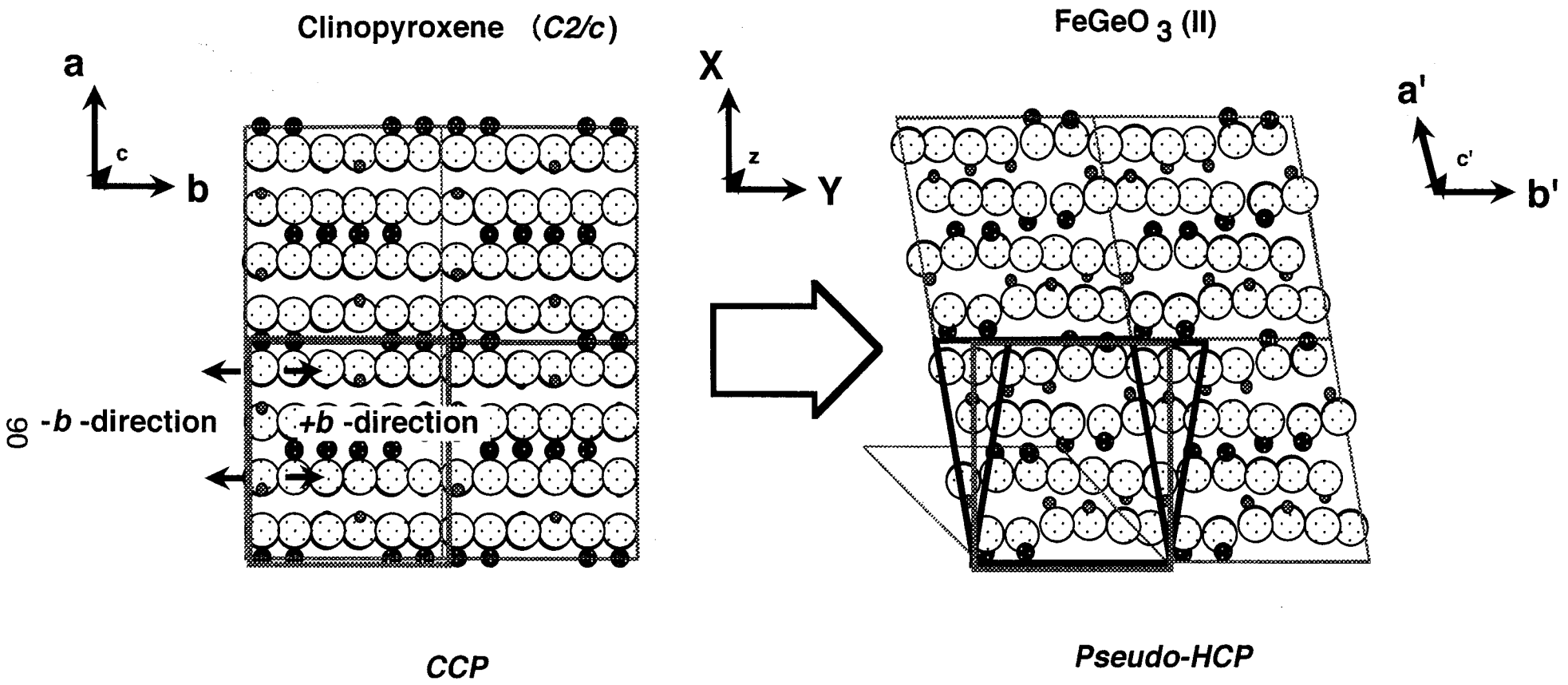

Fig. 5.3 Crystallographic relation between clinopyroxene and $FeGeO_3$(II). Both structure have the common *b*-*c* plane. The cell of t $FeGeO_3$(II) is based on conventinal axes of *a*', *b*' and *c*'.

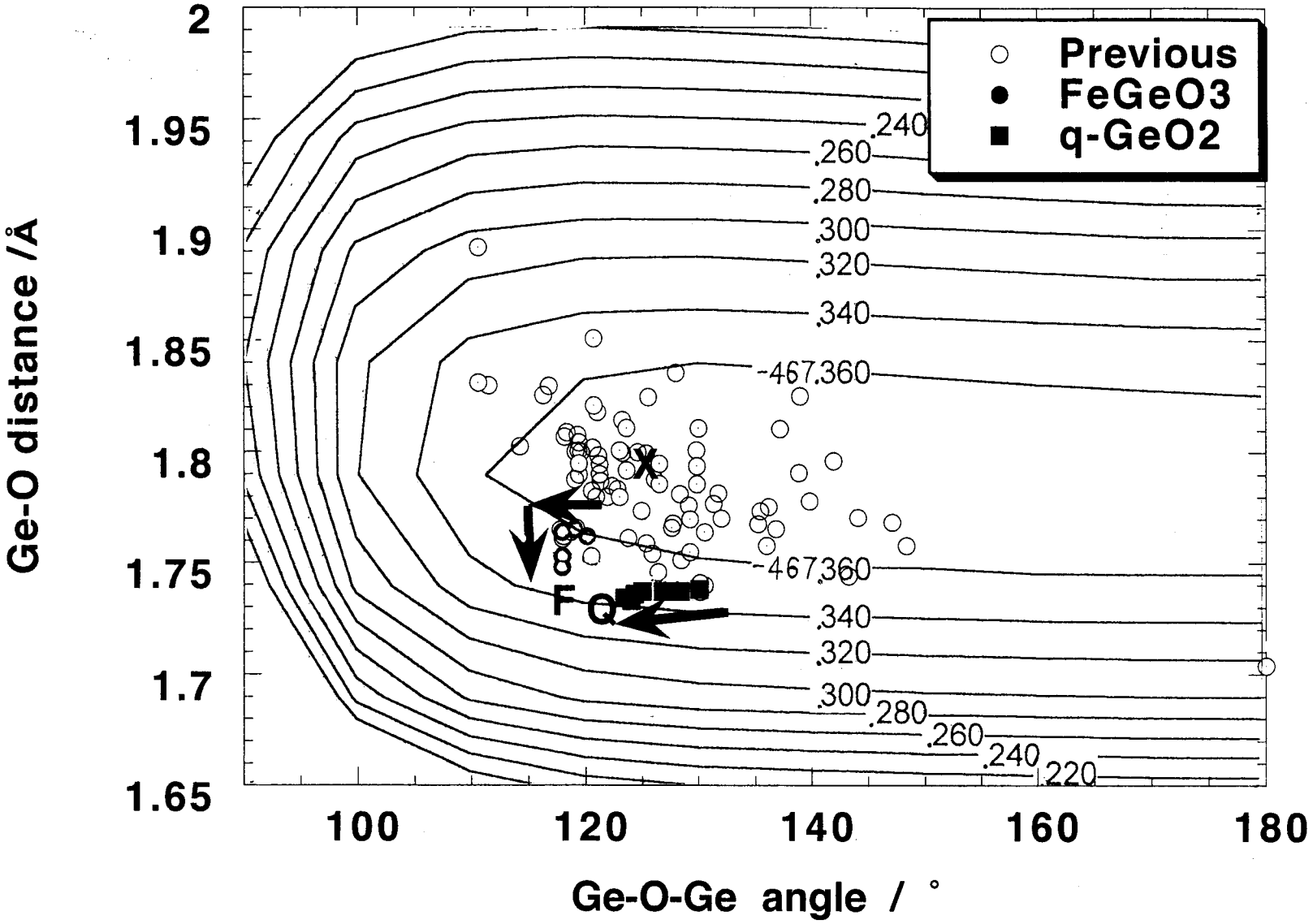

Fig. 5.4 86 geometries in 39 germanates observed in real crystals.

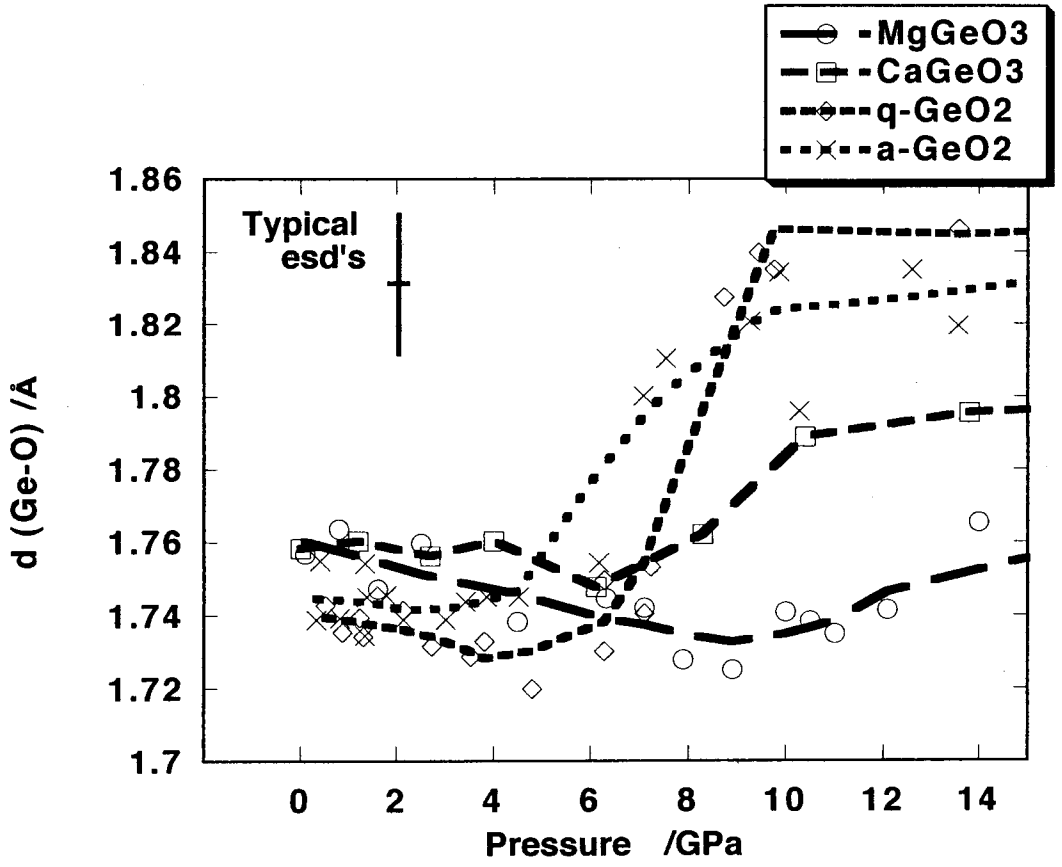

Fig. 5.5 Variation of Ge-O distance of germnates compounds at high pressures.

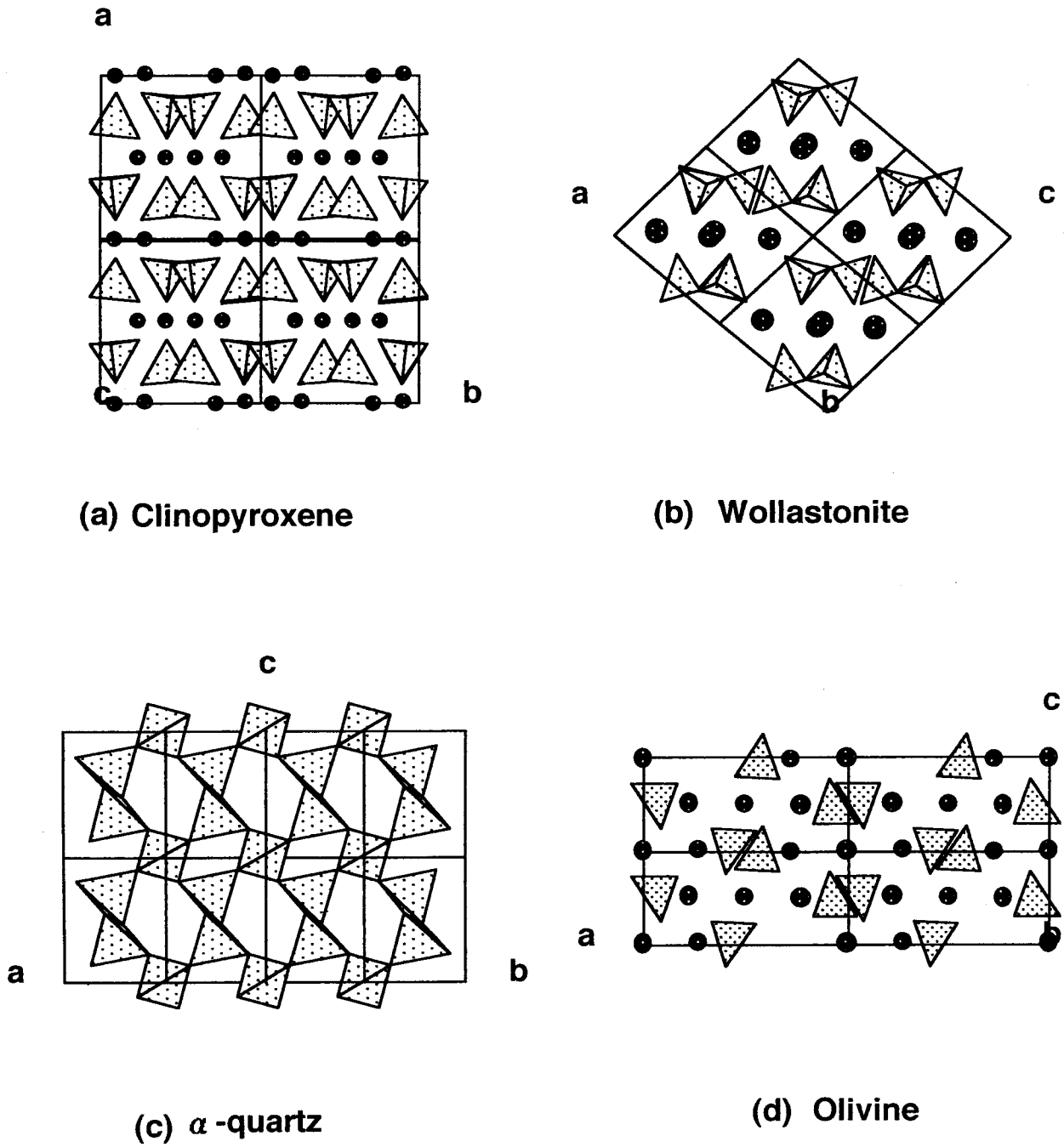

Fig. 5.6 Projections of the crystal structures.
(a) pyroxene along *c*-axis, (b) wollastonite along *b*-axis, (c) olivine along *b*-axis and (d) α -quartz along *110* direction.

6. Conclusions

In order to elucidate the mechanism and the onset of transformation of mineral compounds under high-pressure and low-temperature where the atoms are not thermally activated, the transformation process and the transition mechanism of $FeGeO_3$ clinopyroxene (*C2/c*) were investigated by an in-situ powder X-ray diffraction, a high-pressure single crystal X-ray diffraction, TEM observation and MO calculation.

The results of these experiments clarified the following points:

(i) The transformations involving the atomic diffusion process is strongly hindered at low temperature where the atoms are not thermally activated. Under such condition, the transformations are accompanied with diffusionless mechanism instead of the diffusion mechanism.

(ii) The transformations of the metastably compressed phases with tetrahedral linkage are induced by the local instability of the tetrahedral linkage. The parent phase are transformed into high-pressure phase at the pressure where the geometry of the tetrahedral linkage approaches to the geometrical limit. It is considerably different from the usual transformation at high temperature, in which the transformation starts at the pressure where the free energies of both phase become equal.

(iii) The transformation processes at room temperature and high-pressure conditions are strongly effected by the crystal structures of the parent phases, because the transformations are accompanied by the small movements of atoms. Especially, the states after the transformation (crystalline states or amorphous state) are controlled by the arrangement of the cations which increase coordination number at high pressure.

Appendix

High-pressure transformation of $FeGeO_3$(II) at high temperature

A.1 Purpose

$FeGeO_3$ clinopyroxene (*C2/c*) have transformed into the high-pressure phase of $FeGeO_3$(II) above 13 GPa at room temperature. The structure of the high-pressure phase is based on the deformed hexagonal closest packing and has the cationic arrangement similar to those in the clinopyroxene. This structure has not been reported. To know the stability of this phase, the transformation process of $FeGeO_3$(II) under high-temperature condition was investigated by in-situ powder X-ray diffraction method.

A.2 Experimental

A.2.1 Generation of the high-pressure and temperature

The condition of high-pressure and high-temperature was generated by the electric resistance heater in DAC. The schematics are shown in Fig. A.1. The heater was made by the following procedures. The nicrome wire with diameter of 0.2 mm ϕ was rounded around the alumina ring with the diameter of 17 mm. These were fixed together using the Aron Ceramic (Touagousei). The resistance of this heater was about 4 Ω. This heater was installed inside of the cylinder of the Mao-Bell type diamond anvil cell. The alternating electric current was supplied to the heater by a slide rheostat. The temperature of the sample was monitored by a CA thermocouple fixed nearby the sample. The sample temperature was controlled manually by adjustment of the resistance of the slide rheostat. The DAC body was cooled by a water cycling system to avoid the heat up of DAC stage of X-ray diffraction system.

In the high-pressure and high-temperature experiment, the silicon grease was used as a pressure transmitting medium instead of the mixture of methanol and ethanol because the

mixture often blow out easily under high-temperature condition. The silicon grease froze at about 3 GPa and, therefore, the hydrostaticity in the sample room was considered to be highly deviated from the hydrostatic condition above 4.5 GPa.

A.2.2 Pressure determination at high temperature

In the high-pressure and high-temperature condition, the pressure cannot be determined by the ruby fluorescence method (*ruby scale*) because the wavelength of the ruby fluorescence line are also shifted by temperature as well as pressure. It is known that the lattice parameters of gold change as the functions of pressure and temperature. Thus, the pressure can be determined from the lattice parameters of the gold when the temperature is known by another method independently. Therefore, the pressure at high temperature was determined from the lattice parameters of gold in the sample room. The pressure was calculated from the lattice parameters on the basis of the equation of the state (EOS) (*Au scale*) (Jamieson et al. 1982), where the lattice parameters were determined from at least three reflections by least square refinements. The differences between the pressures determined by Au scale and by ruby scale were within about 1 GPa even at 20 GPa.

A.2.3 Powder X-ray diffraction

In-situ X-ray diffraction was performed at BL-18C in PF. The powder diffraction data was taken by the same procedure as mentioned in Chapter 4.1. The experimental conditions of pressure and temperature and the exposure time are shown in Fig. A.2. The diffraction patterns were taken after the pressure increase up to 20.7 GPa. The temperature was increased up to about 350 °C. The pressure in the sample room was also increased unexpectedly by the heating. Typical exposure time for each X-ray pattern was about one hour.

A.3 Results

A.3.1 Transition process of $FeGeO_3$ clinopyroxene under non-hydrostatic condition

The X-ray diffraction pattern at about 20.7 GPa and at room temperature is shown in Fig. A.3. Most of the peaks are indexed as $FeGeO_3$ (II). Each diffraction peaks appear to be slightly broader than those in the hydrostatic compression. A reflection at the 2θ angle of about 13.6°, which is shown by "†", can be indexed as neither clinopyroxene nor $FeGeO_3$ (II). This reflection is considered to appear due to the shear stress caused by the non-hydrostaticity in the sample room.

A.3.2 Transition process of $FeGeO_3$ (II) at high pressure and high temperature

The newly appeared peaks in the non-hydrostatic compression increases their intensity and the peaks, which are shown by "††" in Fig. A.3, also appears at the 2θ angles of 8.8°, 9.9° 16.7°, 19.9° with increasing temperature up to 365 °C within two hours. At the same time, the peak intensities of the $FeGeO_3$ (II) decreases. All the newly observed peaks are indexed as hexagonal system. It in inferred from the lattice parameters and the diffraction intensities that this phase is one of the corundum related phases. The presence of the *003* reflection suggests this phase has ilmenite structure (*R3̄*) (*00l:* l=3n), neither $LiNbO_3$-type structure (*R3c*) (*00l:* l=6n), nor corundum structure (*R3̄c*) (*00l:* l=6n). These results suggests that most part of the $FeGeO_3$ (II) phase transforms into the ilmenite. The observed peaks in the non-hydrostatic compression is considered to be from ilmenite phase.

The X-ray pattern of the recovered sample at ambient condition is also shown in Fig. A.3. The high background is due to the sample holder. All diffraction peaks are indexed as clinopyroxene or ilmenite phase. It is considered from the reversibility between the clinopyroxene and $FeGeO_3$ (II) that the clinopyroxene peaks is observed because some part of the untransformed $FeGeO_3$ (II) transforms back into the clinopyroxene phase on release of the pressure. These results reveal

that $FeGeO_3$ (II) transforms irreversibly into ilmenite with increasing temperature up to 350 °C.

A.3.3 Volume change during the phase transformation

The lattice parameters of the ilmenite at 19.6 GPa and 0.1MPa under room temperature condition are listed in Table A.1. The volume of ilmenite for one chemical unit (Z=1) at high pressures are shown in Fig. A.4, together with those of clinopyroxene and $FeGeO_3$ (II). The smaller volume of $FeGeO_3$ ilmenite compared to $FeGeO_3$(II) suggests that the $FeGeO_3$ ilmenite is more stable than $FeGeO_3$ (II).

A.4 Discussion

A.4.1 Transformation mechanism from $FeGeO_3$ (II) into ilmenite

The reconstructive phase transformation generally need the larger thermal energy and the longer duration time. In the present study, most part of $FeGeO_3$(II) transformed quickly into ilmenite within the short duration time (< 2 hours) in spite of the relatively low annealing temperature of 365 °C. Thus, the present results on $FeGeO_3$ (II) suggest that the transformation into ilmenite does not involve the long-range diffusion of atoms. The crytal structures of $FeGeO_3$ (II) and ilmenite phases are shown in Fig. A.5. Both structures are based on hexagonal closest packing in common. The only difference is the cationic arrangement of Fe^{2+} and Ge^{4+} cations in their interstices between oxygen stacking layers. Therefore, the transformation from $FeGeO_3$ (II) to ilmenite is possible by the reordering of the Fe^{2+} and Ge^{4+} cation in their interstices. The jump of one-sixth of Fe^{2+} and Ge^{4+} cation into the adjacent octahedral site transforms $FeGeO_3$ (II) into ilmenite without the reconstruction of the oxygen sublattice. Through this mechanism, the $FeGeO_3$ (II) is considered to transform into ilmenite readily even at relatively low temperature.

A.4.2 Effects of the shear stress on transformation of clinopyroxene

The present study under non-hydrostatic condition suggests that the shear stress caused by

the non-hydrostaticity in sample room promotes the transformation of clinopyroxene into ilmenite phase. It is inferred from the above mentioned transformation mechanism into ilmenite that shear stress helps the migration of Fe^{2+} and Ge^{4+} cation between the oxygen stacking layers. Such promotion of the cation diffusion by shear stress are understood by synchroshear (Kronberg 1957; Poirier 1981). In the present study, some part of $FeGeO_3$ clinopyroxene in considered to transform directly into ilmenite through synchroshear mechanism.

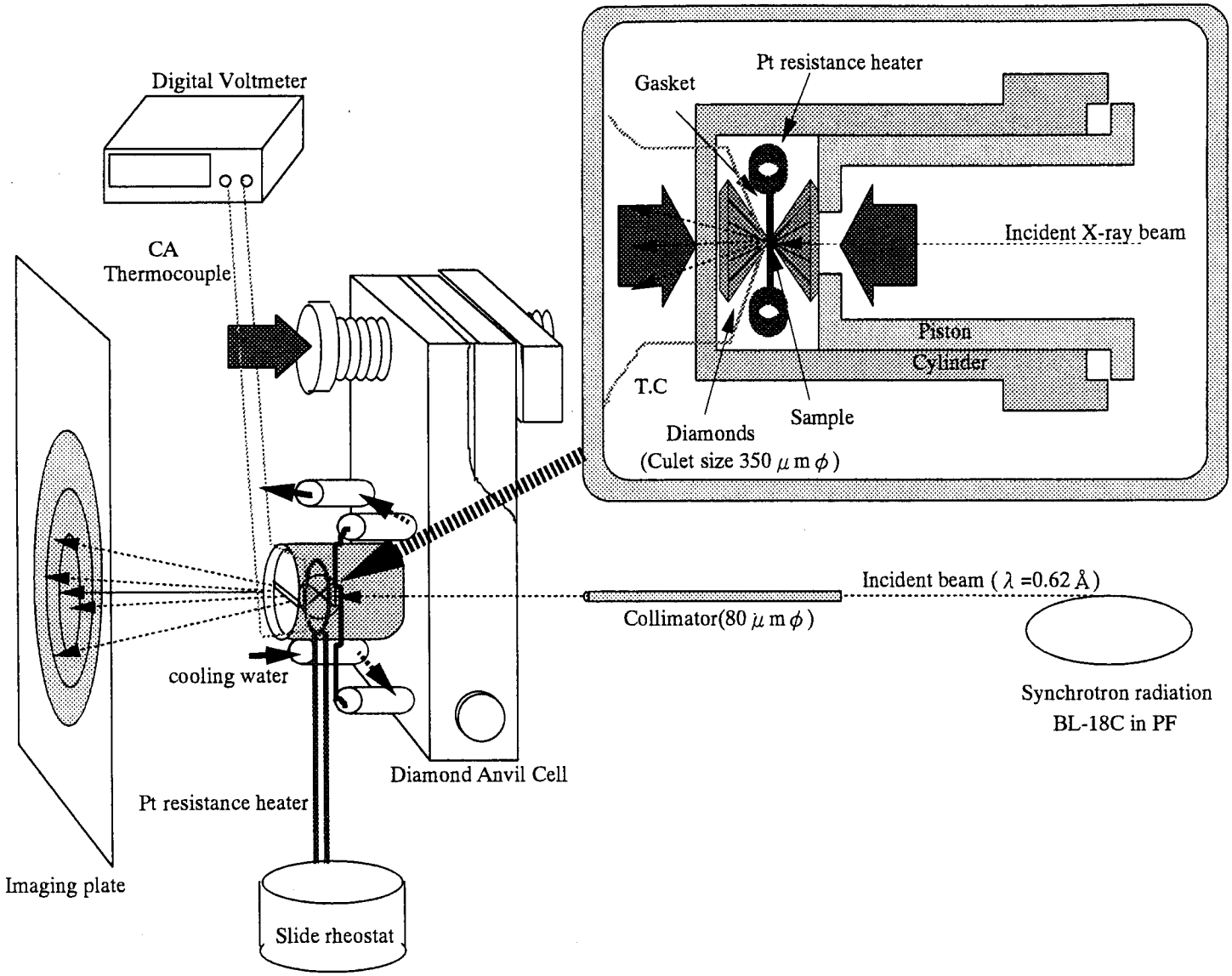

Fig. A.1 Optics of the high-pressure and high-temperature experiments.

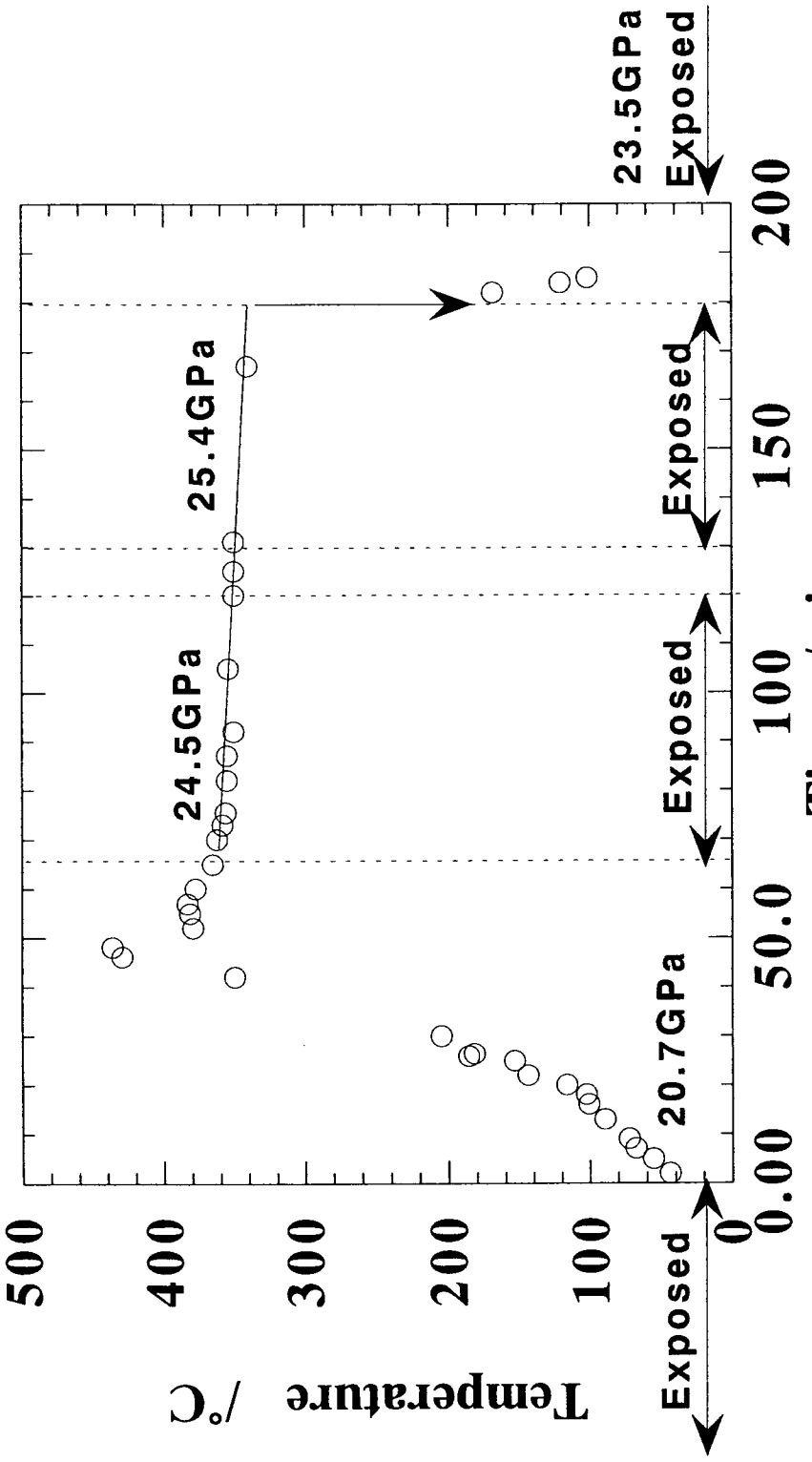

Fig. A.2 Experimental conditions of pressure and temperature and the exposure time

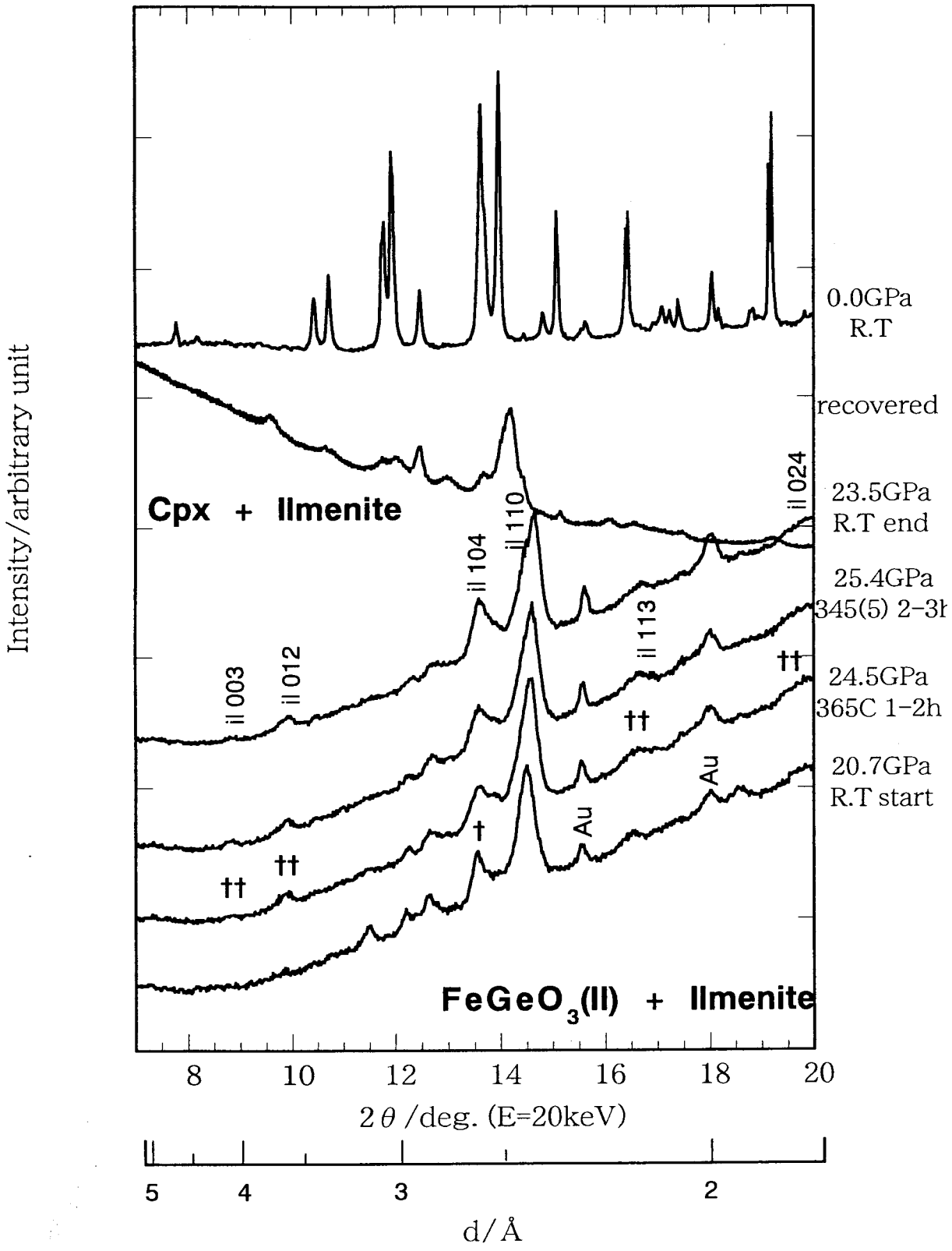

Fig. A.3 X-ray diffraction patterns at high pressures and at various temperatures.

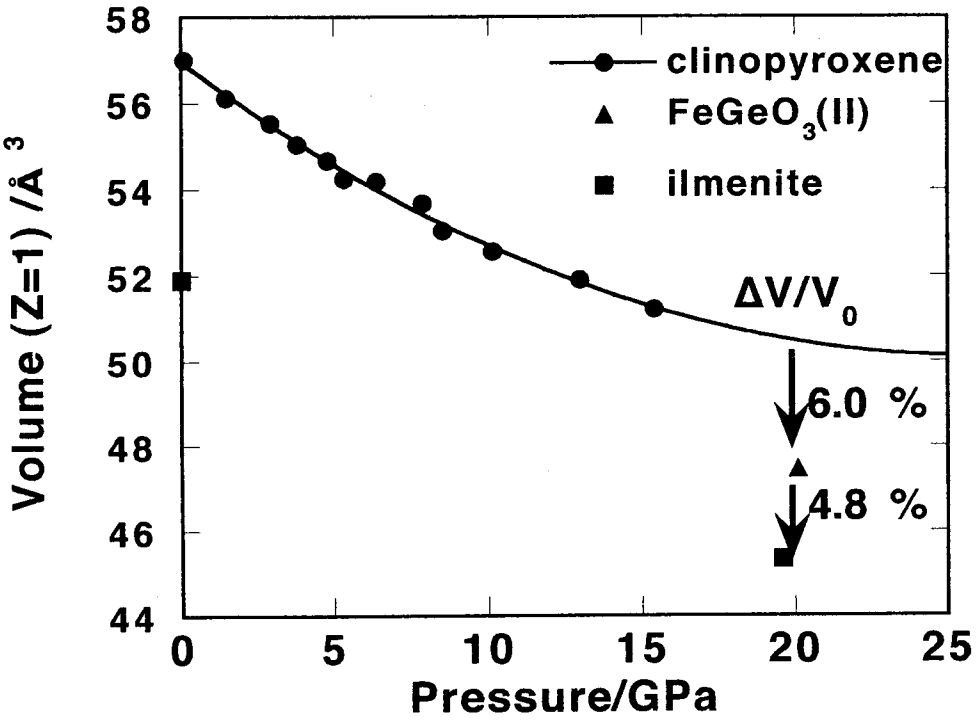

Fig. A.4 Volumes per one chemical formula ($Z = 1$) of the clinopyroxene, $FeGeO_3$ (II) and ilmenite at high pressures.

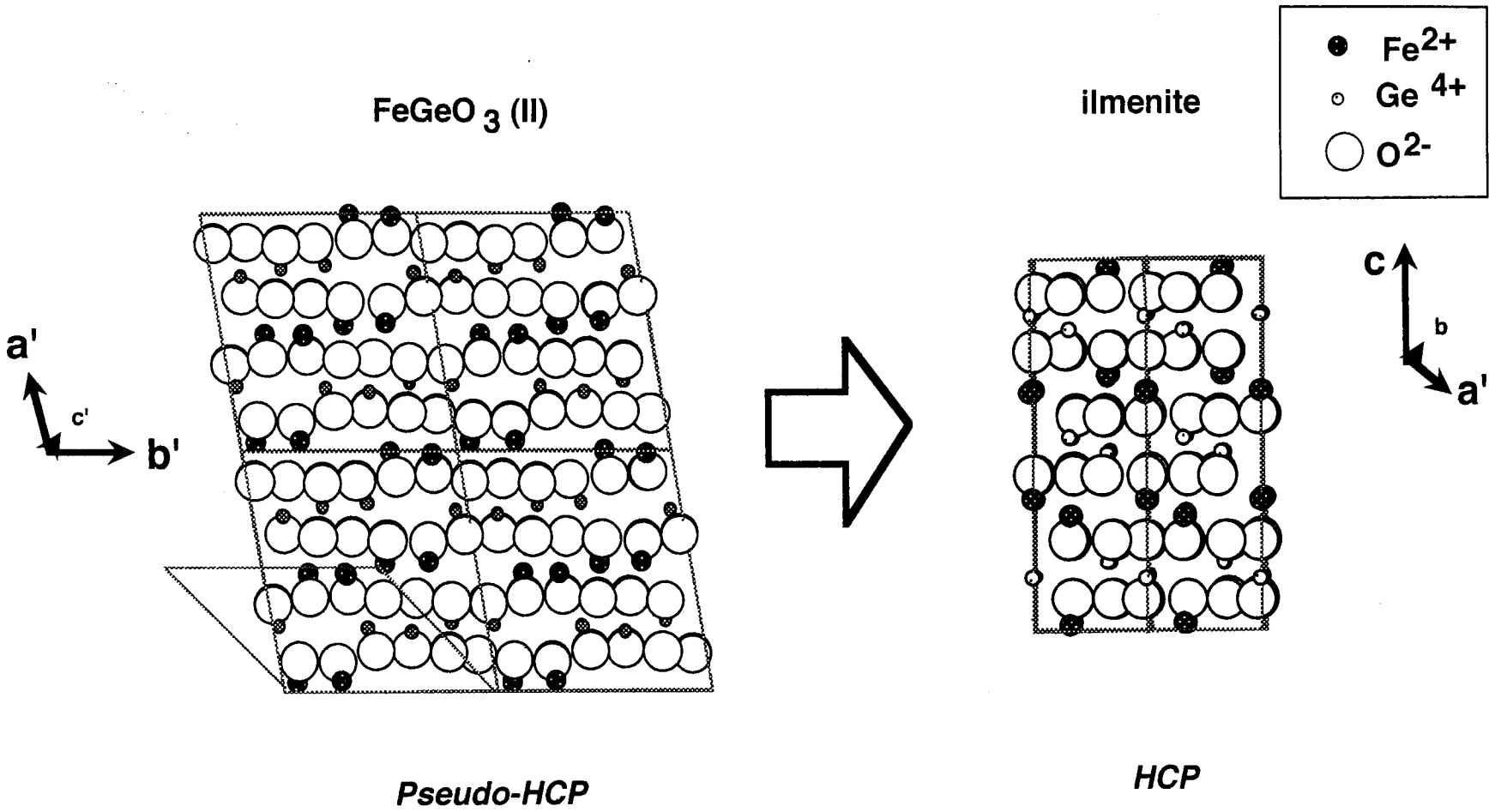

Fig. A.5 Schematic views of $FeGeO_3$ (II) and ilmenite (a) along the direction parallel to the oxygen stacking layer

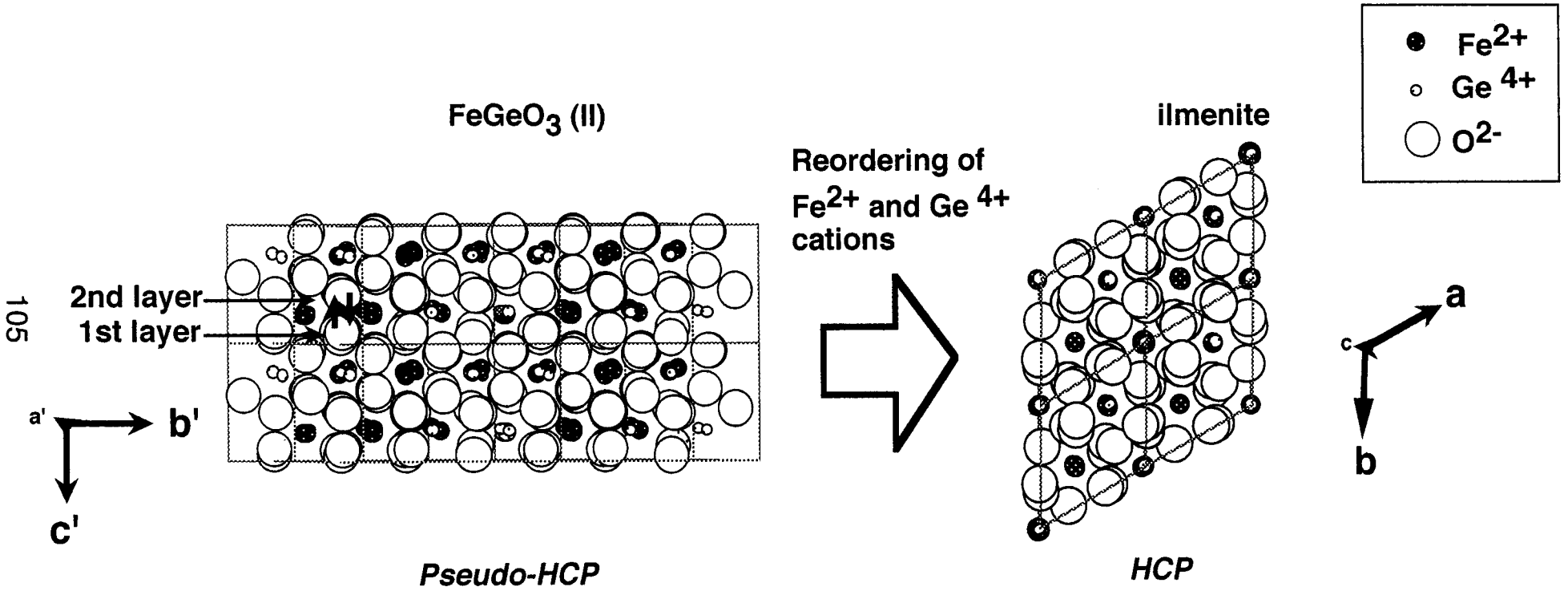

Fig. A.5 Schematic views of $FeGeO_3$ (II) and ilmenite (b) along the stacking direction.

Table A.1 Lattice parameters and the estimated standard deviations of $FeGeO_3$ ilmenite at high pressures at room temperature

P(GPa)	a(Å)	c(Å)	V(Å^3)	V/Z (Å^3)
23.5	4.861(3)	13.29(1)	272.0(4)	45.33(7)
0.0	5.051(11)	14.09(5)	311.4(15)	51.9(30)

Standard deviation for each value is shown in the parenthesis.

References

Ahsbahs, H. (1984) Diamond-anvil high-pressure cell for improved single-crystal X-ray diffraction measurements. Review of Scientific Instruments, 55, 99-102.

Andrault, D., Madon, M., Itie, J.P., and Fontaine, A. (1992) Compression and coordination changes in pyroxenoids : an EXAFS study of $MgGeO_3$ enstatite and $CaGeO_3$ wollastonite. Physics and Chemistry of Minerals, 18, 506-513.

Angel, R.J., Chopelas, A., and Ross, N.L. (1992) Stability of high-density clinoenstatite at upper-mantle pressures. Nature, 358, 322-324.

Brar, N.S. and Schloessin, H.H. (1981) The kinetics of the GeO2 (α-quartz)→(rutile) transformation under high pressure. High Temperatures -High pressures, 13, 313-320.

Buerger, M.J. (1951) In Phase Transformations in Solids. Eds. R. Smoluchowski, John Wiley, New York.

Buerger, M.J. (1961) Fortschritte der Mineralogie, 39, 9.

Bunshah, R.F., and Mehl, R.F. (1953) Journal of Metals, 5, 1250

Cameron, M. and Papike, J.J. (1980) Crystal chemistry of silicate pyroxenes. Mineralogical Society of America Reviews in Mineralogy, 7, 5-92.

Chelikowsky, J.R., King, H.E., Troullier, N., Martins, J.L., and Glinnemann, J. (1990) Structural properties of α - quartz near the amorphous transition. Physical Review Letters, 24, 3309-3312.

Christian, J.W. (1965) In Physical Properties of Martensite and Bainite. Special Report 93, The Iron and Steel Institute.

Finger, L.W. and King, H. (1978) A revised method of operation of the single-crystal diamond cell and refinement of the structure of NaCl at 32 kbar. American Mineralogist, 63,

337-342.

Fujishiro, I., Piermarini, G.J., Block, S., and Munro, R.G. (1982) High Pressure Research Ind. AIRAPT Conference 8th, 608.

Geisinger, K.L., Gibbs, G.V., and Navrotsky, A. (1985) A molecular orbital study of bond length and angle variations in framework structure. Physics and Chemistry of Minerals, 11, 266-283.

Gibbs, G.V. (1982) Molecules as models for bonding in silicates. American Mineralogist, 67, 421-450.

Gibbs, G.V., D'Arco, P., and Boisen, M.B. (1987) Molecular mimicry of bond length and angle variations in germanate and thiogermanate crystals: A comparison with variations calculated for C-, Si-, and Sn-containing oxide and sulfide molecules. The Journal of Physical Chemistry, 91, 5347-5354.

Gibbs, G.V., Boisen, M.B., Hill, F.C., Tamada. D., and Downs, R.T. (1998) SiO and GeO bonded interactions as inferred from the bond critical point propertied of electron density distributions. Physics and Chemistry of Minerals, 25, 574-584.

Glinnemann, J., King, H.E., Schulz, H., Hahn, Th., La Placa, S. J., and Dacol, F. (1992) Crystal structures of the low-temperature quartz-type phases of SiO_2 and GeO_2 at elevated pressure. Zeitschrift fur Kristallographie, 198, 177-212.

Hazen, R.M., Finger, L.W., Hemley, R.J., and Mao, H.K. (1989) High-pressure crystal chemistry and amorphization of α - quartz. Solid State Communications, 72, 507-511.

Hemley, R.J., Jephcoat, A.P., Mao, H. K., Ming, L. C., and Manghnani, M.H. (1988) Pressure-induced amorphization of crystalline silica, Nature, 334, 52-54.

Hugh-Jones, D.A. and Angel, R.J. (1994) A compressional study of $MgSiO_3$ orthoenstatite up to

8.5 GPa. American Mineralogist, 79, 405-410.

Hugh-Jones, D.A., Chopelas, A., and Angel, R.J. (1997) Tetrahedral compression in (Mg, Fe)SiO_3 orthopyroxenes. Physics and Chemistry of Minerals, 24, 301-310.

Itie, J.P., Polian, A., Calas, G., Petiau, J., Fontaine, A., and Tolentino, H. (1989) Pressure-induced coordination change in crystalline and vitreous GeO_2. Physical Review Letters 63, 398-401.

Jamieson, J.C., Fritz, J.N., and Manghnani (1982) In High-Pressure Research in Geophysics, edited by S. Akimoto and M.H. Manghnani, Center for Academic Published, Tokyo.

Kanzaki, M. (1991) Ortho/clinoenstatite transition. Physics and Chemistry of Minerals, 17, 726-730.

Keller, R. and Holzapfel, W.B. (1977) Diamond anvil device for X-ray diffraction on single crystals under pressures up to 100 kilobar. Review of Scientific Instruments, 48, 517-523.

Kim-Zajonz, J., Werner, S., and Schulz, H. (1999) High pressure single crystal X-ray diffraction study on α-quartz. Zeitschrift fur Kristallographie, 214, 324-330.

Koepke, J., Dieterich, W., Glinnemann, J., and Shultz, H. (1985) Improved diamond anvil high-pressure cell for single crystal work. Review of Scientific Instruments, 56, 2119-2122.

Kolle, J.J. and Blacic, J.D. (1982) Deformation of single crystal clinopyroxenes: 1. Mechanical twinning in diopside and hedenbergite. Journal of Geophysical Research, 87, 4019-4034.

Kronberg, M.L. (1957) Plastic deformation of single crystals of sapphire; Basal slip and twinning, Acta Metallurgica, 5, 507-524.

Kudoh, T. and Takeda, H. (1986) Single crystal X-ray diffraction study on the bond compressibility of fayalite, Fe_2SiO_4 and rutile, TiO_2 under high pressure. Physica 139&140B, 333-336.

Lapeyre, C., Petiau, J., Calas, G., Gauthier, F., and Gombert, J. (1983) Bulletin of Mineralogy, 106, 77.

Levien, L. and Prewitt, C.T. (1981) High-pressure structural study of diopside. American Mineralogist, 66, 315-323.

Loveday, J.S., McMahon, M.I., and Nelmes, R.J. (1990) The effect of diffraction by the diamonds of a diamond-anvil cell on single-crystal sample intensities. Journal of Applied Crystallography, 23, 392-396.

Mardon, M., Gillet, P., Julien, Ch., and Price, G.D. (1991) A vibrational study of phase transitions among the GeO_2 polymorphs. Physics and Chemistry of Minerals, 18, 7-18.

Mao, H.K., Bell, P.M., Shaner, J.W., and Steinberg, D.J. (1978) Specific volume measurement of Cu, Mo, Pd and Ag and calibration of the ruby R_1 fluorescence pressure gauge from 0.06 to 1 Mbar. Journal of Applied Physics, 46, 6, 3276-3283.

Mao, H.K., Xu, J., and Bell, P.M. (1986) Calibration of the ruby pressure gauge to 800 kbar under quasi-hydrostatic condition. Journal of Geophysical Research, 91, 4673-4676.

Merrill, L. and Bassett, A. (1974) Miniature diamond anvil pressure cell for single crystal X-ray diffraction studies. Review of Scientific Instruments, 45, 290-294.

Nagai, T. (1995) Pressure-induced structural modifications and amorphization of $CaGeO_3$-wollastonite, $MgGeO_3$-high-clinoenstatite and Mg_2GeO_4-olivine. Ph.D Thesis, Tokyo University.

Peacor, D.R. (1968) The crystal structure of $CoGeO_3$. Zeitschrift fur Kristallographie, 126, 299-306.

Peacor, D.R. and Prewitte, C.T. (1963) Comparison of the crystal structures of bustamite and wollastonite. American Mineralogist, 48, 588-596.

Pacalo, R.E.G. and Gasparik, T. (1990) Reversal of the orthoenstatite-clinoenstatite transition at high pressures and high temperatures. Journal of Geophysical Research, 95, 15853-15858.

Poirier, J.P. (1981) Martensitic olivine-spinel transformations and plasticity of the mantle transition zone, In Anelasticity in the Earth, Geodynamic Series volume 4, edited by F.D. Stacey, M.S. Paterson, and A. Nicholas, pp. 113-117, AGU, Washington, D.C.

Rao, C.N.R. and Rao, K.J. (1978) In Phase Transformations in Solids, McGraw-Hill.

Richard, P. and Gillet, P. (1997) Pressure-induced amorphization of minerals: a review. European Journal of Mineralogy, 9, 907-933.

Sasaki, S. (1987) RADY: A fortran program for the least-squares refinement of crystal structures, KEK internal 87-3, Tsukuba, National laboratory for high energy physics.

Schiferl, D. (1977) 50-kilobar gasketed diamond anvil cell for single-crystal X-ray diffractometer use with the crystal structure of Sb up to 26 kilobars as a test problem. Review of Scientific Instruments, 48, 24-30.

Shannon, R.D. (1976) Revised effective ionic radii and systematic studies of interatomic distances in halides and chalcogenides. Acta Crystllographica, A32, 751-767

Shimobayashi, N. and Kitamura, M. (1991) Phase transition in Ca-poor clinopyroxenes. Physics and Chemistry of Minerals, 18, 152-160.

Takayama, E., Kimizuka, N., Kato, K., Yamamura, H., and Haneda, H. (1981) Journal of Solid State Chemistry, 38, 82-86.

Tsuneyuki, S., Tsukada, M., Aoki, H., and Matsui, Y. (1988) First-principles interatomic potential of silica applied to molecular dynamics. Physical Review Letters, 61(7), 869-872.

Werner, S., Kim-Zajonz, J., Wittlinger, J., and Sieber, M. submitted to Review of Scientific Instruments.

Werner, S., Kim-Zajonz, J., Wittlinger, J., and Schulz, H. (1996) Workshop on the Use of ultrashort Wavelengths. Hasylab. Hamberg, Germany (Proceedings).

Wolf, G.H., Wang, S., Herbst, A., Durben, D.J., Oliver, W.F., Kang, Z.C., and Halvorson, K. (1992) Pressure induced collapse of tetrahedral framework in crystalline and amorphous GeO_2. High-pressure research: Application to Earth and Planetary Sciences. edited by Shono, Y., Manghnani, M.H., pp.503-517. Terra Scientific Publishing Company (TERRAPUB) , Tokyo / American Geophysical Union, Washington, D.C., 1992

Yagi, T. and Akimoto, S. (1982) Rapid X-ray measurements to 100 GPa range and static compression of α-Fe_2O_3. In: High-Pressure Research in Geophysics., eds. Akimoto, S. and Manghnani, M.H., 89-91, TERRAPUB, Tokyo.

Yamanaka, T., Shibata, T., Kawasaki, S., and Kume, S. (1992) Pressure-induced amorphization of hexagonal GeO_2. High-pressure research: Application to Earth and Planetary Sciences. edited by Shono, Y., Manghnani, M.H., pp. 493-501. Terra Scientific Publishing Company (TERRAPUB) , Tokyo / American Geophysical Union, Washington, D.C., 1992

Yamanaka, T., Sugiyama, K., and Ogata, K. (1992) Kinetic study of the GeO2 transition under high pressures using Synchrotron X-radiation. Journal of Applied Crystallography, 22, 11-15.

Yamanaka, T., Nagai, T., and Tsuchiya, T. (1992) Mechanism of pressure-induced amorphization. Zeitschrift fur Kristallographie, 212, 401-410.

Yamaoka S., Fukunaga O., Shimomura O., and Nakazawa, H. (1979) Versatile type miniature diamond anvil high-pressure cell, Review of Scientific Instruments, 50, 1163-1164.

Zeto, R.J. and Roy, R. (1969) In Reactivity of Solids, Proceedings of the 6th international Symposium on the Reactivity of Solids, Schenectady, NY, 1968. Eds. J.W. Mitchell, R.C. DeVries, R.W. Roberts, P. Cannon (New York: John Wiley) pp. 803-813.

Zhang, Li., Ahsbahs, H., Hafner, S.S., and Kutoglu, A. (1997) Single-crystal compression and

crystal structure of clinopyroxene up to 10 GPa. American Mineralogist, 82, 245-258.